FIBER-SHAPED PEROVSKITE SOLAR CELLS FOR HIGH PERFORMANCE SOLAR FABRICS

BALILONDA ANDREW

PhD

The Hong Kong Polytechnic University

2025

The Hong Kong Polytechnic University

School of Fashion and Textiles

Fiber-Shaped Perovskite Solar Cells for High Performance Solar Fabrics

Balilonda Andrew

A thesis submitted in partial fulfillment of the requirements for the degree of Doctor of Philosophy

Aug 2024

Certificate of Originality

I hereby declare that this thesis is my own work and that, to the best of my knowledge and belief, it reproduces no material previously published or written, nor material that has been accepted for the award of any other degree or diploma, except where due acknowledgement has been made in the text.

_____(Signature)

Balilonda Andrew (Name of student)

Abstract

The advancement of fabrication technologies and the miniaturization of electronic devices triggered the rise of wearable electronics. However, these devices require substantial amount of power, which puts strain on the main power grids. To address this issue, fiber-shaped solar cells have emerged as a solution, providing self-powered devices and flexible/bendable photovoltaic systems. Fiber-shaped solar cells offer a multitude of advantages due to their unique geometry. Their increased flexibility allows for versatile applications, making them ideal for integration with various devices and structures. The lightweight makes them easy to handle, while their ability to conform to the human body and other shapes opens up new possibilities for wearable technology and architectural design. These innovative solar cells provide a sustainable and aesthetically pleasing solution for capturing solar energy in a wide range of settings. As a result, there is increasing need for highly efficient and stable fiber-shaped solar cells and solar fabrics to power portable and wearable electronics.

A crucial component of any solar cell is the photovoltaic layer. Perovskite, a new photovoltaic material, offers extraordinary energy conversion efficiency, and can be processed using solution-based methods. This presents an opportunity to develop low-cost and high-performance fiber-shaped solar cells.

Despite the remarkable power conversion efficiency (PCE) beyond 25.5%, perovskite solar cells, especially the Sn-based variants lack stability compared to silicon solar cells. Hybrid 2D/3D perovskite materials offer a solution to the stability issue in solar cells without compromising efficiency, with record stability of > 1 year. However, the reaction between 2D and 3D perovskite molecules requires high temperatures (~300ºC) and increased reaction time (~24 hours) to achieve high-quality 2D3D hybrid perovskites. In the first part our study, we based on the ability of chlorine to displace iodine from its ionic compounds in solutions to utilize chloride ions as catalysts for speeding up the reaction between iodine-based 2D and 3D perovskite molecules. By using this method, high-quality 2D3D hybrid material formed in a short time and a low temperature ~ 100ºC. Integrating the synthesized and optimized hybrid perovskite material in a fiber-shaped solar cell architecture yielded the high PCE of 11.96% in Sn-based fiber-shaped perovskite solar cells. The unencapsulated and encapsulated fiber-shaped solar cells could

maintain 75% and 95.5% of their original PCE respectively, after 2000 hours under room light and relative humidity of 35-40%.

To further improve the performance and stability of fiber-type Sn-based perovskite solar cells, the second part of our study focused on minimizing the oxidation of Sn-based perovskite materials, which results into material degradation. Sn-based perovskite materials have gained attention as an alternative to Pb-based materials in order to address the issue of toxicity in perovskite solar cells. However, Sn-based perovskite solar cells are known for their poor stability and loss of efficiency due to the rapid oxidation of Sn^{2+} to Sn^{4+} when exposed to air. Various antioxidants have been proposed to slow down the oxidation process. Nevertheless, during the antioxidation process, the antioxidant itself undergoes oxidation and forms non-antioxidizing by-products. This occurs in a single-stage redox reaction, depleting the antioxidants quickly and diminishing their ability to prevent oxidation. In this study, we introduced vanillin, a natural antioxidant that undergoes two redox reactions in succession. This enables it to inhibit the oxidation of Sn^{2+} or reduce Sn^{4+} back to Sn^{2+}. As a result, it improves the efficiency of the solar cells and prolongs the open-air stability of Sn-based perovskite solar cells. By doping the perovskite material with 7.5% vanillin, we achieved an impressive efficiency of 13.18% using a flexible one-dimensional solar cell architecture, which currently represents the highest efficiency in Sn-based fiber-type perovskite solar cells. Additionally, exposer of the solar cells to 160W microwave irradiation for 3 minutes, caused the efficiency of the solar cell to recover from 88% to 96.5% (normalized efficiency) at 812 hours, and from 35.7% to 65.4% after approximately 2200 hours of aging under high relative humidity >75% and open-air conditions. This work demonstrates the potential of using natural antioxidants and short microwave irradiation as suitable approaches to increase the efficiency and prolong the lifetime of tin perovskite solar cells.

In the third phase of this study, we demonstrated a novel and sustainable energy solution in the form of photovoltaic fabrics that can serve as reliable energy sources for wearable and mobile devices. The solar fabrics were woven using four fiber-type perovskite solar cells as the weft, and cotton yarns as the warp to create three types of weaves: plain, twill, and satin. The solar yarns in the weave repeats were connected in parallel and series configurations, and the output current and voltage were investigated. This approach of assembling fiber-type solar cells into

solar fabrics achieves large surface area solar energy harvesting platforms with flexibility, three-dimensional deformability, and moisture and heat transfer characteristics of textiles. In this investigation, both the design and performance of the solar energy harvesting fabrics weaves were explored. The resultant fabric weaves were characterized under different solar connections and weave designs. The estimated area of the assembled weave repeats was 50 mm × 45 mm solar active area. With series connection of the inherent solar cells, the voltage increased gradually from 3.84V to 4.01V to 4.03V for plain, twill, and satin woven solar fabrics, respectively. Changing the solar cell connection to a parallel configuration caused a significant increase in current output from 3.877 mA/cm^2 to 3.902 mA/cm^2 to 3.916 mA/cm^2 for plain, twill, and satin solar fabrics. Maximum power density of 3.95 mW/cm^2 was registered with a satin solar fabric (area 22.5 cm^2), with its inherent solar cells connected in a parallel configuration.

List of Publications

Related journal publications

1. **Balilonda A**, Li Z, Fu Y, Zabihi F, Yang S, Huang X, Tao X, Chen W. Perovskite fiber-shaped optoelectronic devices for wearable applications. Journal of Materials Chemistry C. 2022;10(18):6957-91. https://doi.org/10.1039/D2TC00532H
2. **Balilonda A**, Li Z, Luo C, Tao X, Chen W. Chlorine-Rich Substitution Enabled 2D3D Hybrid Perovskites for High Efficiency and Stability in Sn-Based Fiber-Shaped Perovskite Solar Cells. Advanced Fiber Materials. 2023 Feb;5(1):296-311. DOI: 10.1007/s42765-022-00222-y
3. **Balilonda A**, Du M, Li Z, Li W, Mei W, Leung MY, Wu G, Tao X, Chen W. High Performance and Efficiency Recovery in Sn-Based Flexible Perovskite Solar Cells by Antioxidant Vanillin and Microwave Treatment. Advanced Functional Materials. 2024 Jan 11:2313833. https://doi.org/10.1002/adfm.202313833

Other journal publications

1. Li Z, **Balilonda A**, Mei W, Li W, Chen W. A conformal van der Waals graphene coating enabled high-performance piezo-ionic sensor for spatial, gesture, and object recognition. Journal of Materials Chemistry A. 2023;11(21):11288-97. DOI: 10.1039/D3TA00215B
2. Li Z, **Balilonda A**, Yang S, Tao X, Chen W. Graphene-based soft actuator with dynamic spectrum modulation for a smart thermal surface. ACS Applied Nano Materials. 2022 Jun 8;5(6):8298-305. https://doi.org/10.1021/acsanm.2c01378
3. Li Z, Chao X, **Balilonda A**, Chen W. Scalable van der Waals graphene films for electro-optical regulation and thermal camouflage. InfoMat. 2023 Mar 17: e12418. https://doi.org/10.1002/inf2.12418

Acknowledgements

One of the most worthwhile and fulfilling experiences of my life has been pursuing a PhD at The Hong Kong Polytechnic University. Taking this occasion, I would like to sincerely thank God and everyone who has supported and assisted me in this endeavor.

I would like to express my deepest gratitude to my Chief Research Supervisor, Prof. Xiaoming Tao, for his invaluable guidance, unwavering support, and patience throughout my doctoral studies. Her expertise, encouragement, and mentorship have been instrumental in shaping my research and academic journey. I am also grateful to my Co-supervisor, Prof. Chen Wei, for his insightful feedback, encouragement, and constructive criticism, which have greatly contributed to the quality of my research work. I am thankful for their dedication and commitment to helping me succeed.

I would like to extend my appreciation to the faculty and staff members of the School of Fashion and Textiles at Hong Kong Polytechnic University for creating a conducive research environment and providing me with the resources and support necessary for my studies.

I am immensely grateful to the Hong Kong PhD Fellowship Scheme and the Research Grant Council of Hong Kong for awarding me the scholarship that has enabled me to pursue my doctoral studies. This financial support has been crucial in allowing me to focus on my research and academic pursuits.

I would also like to thank my research groupmates for their camaraderie, collaboration, and encouragement throughout this journey. Their support and friendship have been invaluable in making this academic endeavor a rewarding and enriching experience.

Last but not least, I want to express my deepest appreciation to my parents for their unwavering support, love, and understanding. Their belief in me and their sacrifices have been my source of strength and motivation. I am forever grateful for their constant encouragement and support.

I am truly blessed to have had such wonderful individuals and organizations supporting me on this academic journey. Their contributions have been invaluable, and I am deeply thankful for their support.

Table of Contents

List of Figures

Figure 5.5. a) Variation of light intensity with current and voltage output of satin fabric sample. b) Variation of illumination angle with normalized power density of a satin solar fabric.

List of Tables

List of Abbreviations

Photovoltaics	PVs
Giga Watts	GW
Power Conversion Efficiency	PCE
Fiber-Shaped Perovskite Solar Cells	FSPSCs
Electron Transport Layer	ETL
Hole Transport Layer	HTL
Internet of Things	IoT
Levelized Cost of Energy	LCOE
Indium Tin Oxide	ITO
Fluorine doped Tin Oxide	FTO
Transparent Conductive Oxide	TCO
Carbon Nano Tubes	CNT
2,2',7,7'-Tetrakis(N,N-di-p-methoxyphenylamine)9,9'-spirobifluorene	Spiro-OMeTAD
(6,6)-phenyl-C_{61}-butyric acid methyl ester	PCBM
Poly(3-hexylthiophene)	P3HT
Poly(3,4-ethylenedioxythiophenepolystyrene sulfonate	PEDOT: PSS
Poly(methyl methacrylate)	PMMA
Dimethylformamide	DMF
Dimethyl sulfoxide	DMSO
Polyethylene Naphthalate	PEN
Titanium Dioxide	TiO_2
Methylammonium	MA
Scanning Electron Microscopy	SEM
Aminovaleic Acid Iodide	AVI

Chapter 1: Introduction

1.1 Background

The global demand and consumption of energy have been steadily increasing due to the growing global population. As the Earth becomes more populated, the need for energy to power homes, industries, transportation, and technology also rises. However, this trend presents a challenge as traditional energy sources like coal, oil, and natural gas may not be able to meet the rising demand in the near future.[1] This is where renewable energy sources come in. Renewable energy sources such as wind, hydroelectric, geothermal, and biomass offer sustainable alternatives to traditional energy. Among these sources, solar energy stands out as the future of renewable energy due to its abundance, efficiency, and environmental benefits. By harnessing the power of the sun, solar energy provides clean and renewable electricity without emitting harmful gases or depleting finite resources.[2] As technology improves and costs decrease, solar energy is becoming more accessible and cost-effective, making it a key player in the transition towards a more sustainable energy future. Table 1 summarizes the current and predicted future global energy consumption.

Table 1.1 Future forecasts and current global energy statistics (adapted from Reference[1])

Quantity	Definition	Units	2001*	2050†	2100‡
N	Population	B persons	6.145	9.4	10.4
GDP	GDP§	T $/yr	46	140¶	284‖
GDP/N	Per capita GDP	$/(person-yr)	7,470	14,850	27,320
Ė/GDP	Energy intensity	W/($yr)	0.294	0.20	0.15
Ė	Energy consumption rate	TW	13.5	27.6	43.0
C/E	Carbon intensity	KgC/(W·yr)	0.49	0.40	0.31
Ċ	Carbon emission rate	GtC/yr	6.57	11.0	13.3
Ċ	Equivalent CO_2 emission rate	$GtCO_2$/yr	24.07	40.3	48.8

Notes:

*$\dot{E}$ = (403.9 Quads/yr) · (33.4 GWyr/Quad) · (10^{-3} TW/GW) = 13.5 TW; and $\dot{C}$ (24.072 $GtCO_2$/yr) · (12/44 $GtC/GtCO_2$) = 6.565 GtC (*as adapted from Energy Information Administration (2005) Annual Energy Outlook (US Dept of Energy, Washington, DC)).*

† $\dot{E}$ = (869 EJ/yr) · (10^6 TJ/EJ)/(60·60·24·365 s/yr) = 27.5 TW.

‡ $\dot{E}$ = (1,357 EJ/yr) · (10^6 TJ/EJ)/(60·60·24·365 s/yr) = 43.0 TW (adapted from reference (Scenario B2), pp. 48–55].

§All in year 2000 U.S. dollars, using the inflation-adjusted conversions: $\$_{2000}$ = 1/0.81590 $\$_{1990}$ (*as adapted from Energy Information Administration (2005) Annual Energy Outlook (US Dept of Energy, Washington, DC)*), and 'purchasing power parity' exchange rates.

¶In year 2000 U.S. dollars: (113.9 $T\$_{1990}$) · (1/0.81590 $\$_{2000}/\$_{1990}$) = 139.6 $T\$_{2000}$.

‖In year 2000 U.S. dollars: (231.8 $T\$_{1990}$) · (1/0.81590 $\$_{2000}/\$_{1990}$) = 284.1 $T\$_{2000}$.

The sun is a powerful source of energy, continuously releasing a massive amount of radiation towards Earth. In fact, it emits more energy in a single day than what is needed to power all human activities on Earth for an entire year. It's astonishing to think that by covering just 10% of the Earth's surface with solar cells that are only 10% efficient, we could potentially meet the current global energy demands.[3] This highlights the incredible potential of solar energy as a clean and renewable power source for our planet's future. Solar energy is virtually limitless and sustainable, yet it is still not fully utilized. There is still much to explore and improve in solar energy harvesting techniques before we can offer a nearly complete solution to the global energy challenge. Furthermore, photovoltaic (PV) systems have demonstrated great promise in addressing the current issue of climate change.[4]

The PV industry has a fascinating history that dates back to 1883 when the first solar cell was invented. Over the years, researchers and scientists have made remarkable progress in this field, leading to groundbreaking inventions that have revolutionized the way we capture solar energy. In recent years, the growth rate of the PV sector has significantly increased, particularly since 2010. This rapid growth can be attributed to advancements in production methods, which have resulted in an approximate 80% reduction in the costs of solar panels.[1] Solar energy has become more accessible and affordable for a wider range of consumers and businesses. Additionally, the future of the PV industry looks promising due to the development of innovative materials like perovskites. These materials have shown great potential in increasing the efficiency and reducing the costs of solar cells. Some experts even suggest that perovskites could replace traditional silicon-based solar panels in the near future. Since its inception in 1883, the photovoltaic

industry has made significant progress. With continued advancements, we expect growth and progress in the coming years.[5]

In 2018, global solar energy production reached 510 GW, a substantial increase of 106 GW from the previous year. This growth has resulted in a total cumulative production of 404 GW. Looking ahead, predictions indicate that an additional 621.7 GW will be added to the grid between 2018 and 2022, bringing the total solar energy production to an impressive 1025.4 GW by 2022. These estimates are based on the use of silicon-based solar cells, which are known for their long lifespan of over 22 years and an impressive 92% efficiency retention. This upward trend in solar energy production highlights the shift towards renewable energy sources and the potential for a more sustainable future.[1]

Dye-sensitized, quantum-dot, bi/hetero junction organic, and perovskite solar cells are emerging as promising alternatives to traditional silicon photovoltaics. Although these newer technologies are still in the research phase, they offer the potential for lower-cost manufacturing due to their use of low-temperature processes. While their PCE currently lags behind that of silicon cells on the market, perovskite cells have displayed remarkable efficiency levels. Ongoing research and development in these innovative solar cell technologies are expected to result in further improvements in efficiency and affordability, potentially revolutionizing the solar energy industry in the future. [6]

1.2 What are perovskite materials?

Perovskites are photoactive materials with a chemical structure similar to $CaTiO_3$.[7] These materials have a crystal structure represented by an ABX_3 formula, where X can be oxygen or a halogen.[8]

In this crystal structure, the A-cation is stabilized in a Cubo-octahedral position surrounded by twelve X anions. The smaller B-cation, on the other hand, is located in an octahedral site surrounded by six X anions, as shown in Figure 1.1. Perovskites that contain halogen anions and pseudohalide groups, such as thiocyanates,[9] allow monovalent and divalent cations to maintain charge neutrality in the A and B sites, respectively. For example, in the case of $CH_3NH_3PbI_3$, the

A-site cation is $CH_3NH_3^+$, while the B-site cation is Pb^{2+}.[10] Perovskite solar cells commonly use methyl-ammonium lead mono or mixed halides ($CH_3NH_3PbX_3$), with X representing either Br or I. However, the use of chloride is rare due to its large bandgap. The wide bandgap of $CH_3NH_3PbCl_3$ perovskites inhibits electron transfer and negatively affects the performance of the solar cell.[11] Further research on these perovskites has shown that the bandgap can be adjusted by varying the ratio of halides in the methyl ammonium mixed halide ($CH_3NH_3PbI_{3-x}Cl_x$). This property has led to improved power conversion efficiency (PCE) in mixed halide perovskites compared to mono halides.[12] The enhanced performance of mixed halide perovskites is believed to be due to their longer recombination lifetime, resulting in a superior diffusion length.

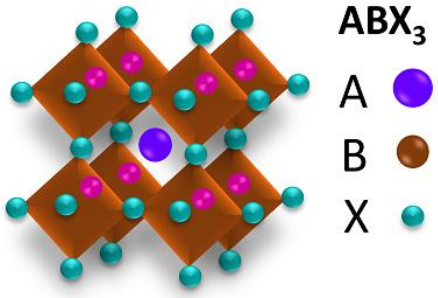

Figure 1.1 Schematic representation of the crystal structure of an organic–inorganic perovskite, where the central A-atom can either be ($CH_3NH_3^+$, Cs^+, and FA^+), while the B atom can be (Sn^{2+}, Pb^{2+}, Ge^{2+}, etc.) surrounded by six halogen atoms.

1.2.1 Mechanism of perovskite photoelectric conversion

Electron-hole pairs in the perovskite layer become excited and separated when the energy of the received photon exceeds the bandgap energy. This leads to a splitting of quasi-Fermi levels. The released charge carriers then move through the photoactive layer towards their respective charge selective layers and accumulate at the electrodes. The movement of these charge carriers is facilitated by the ambipolar nature of perovskites, which allows for balanced transport of both electrons and holes.[13] The intrinsic electric field created at the p-n junction plays a significant role in the separation and migration of electron-hole pairs in opposite directions, as depicted in Figure 1.2a. In perovskite photovoltaic devices, the inbuilt electric field serves as the primary force guiding the charge carriers towards the electrodes, thus preventing recombination.[14] Insufficient electric field force, caused by improper selection of adjacent layers (ETL & HTL), can lead to carrier trapping or accumulation at the interfaces due to insufficient driving force.

Introducing an external electric field to the photoactive layer in photovoltaic systems has been proven to be a strategy for enhancing charge separation and preventing carrier recombination at trap sites, thereby improving the efficiency of perovskite solar cells.[15]

In the photoactive layer of layered films of 3D perovskites, there is a mixture of 2D layered phases (represented by n = 1, 2, 3 in $(BA)_2(MA)_{n-1}Pb_nI_{3n+1}$) and 3D-like perovskite phases (with n = α). This combination allows for energy transfer from the layered phases to the 3D-like perovskites, as well as charge collection through the 3D-like perovskite network. The absorption of photons by the layered perovskite phases contributes to the photocurrent by transferring energy from the larger bandgap layered phases to the smaller 3D-like phases. Excitons are generated in the 3D-like perovskites and quickly dissociate into free charges due to the low exciton binding energy. Carrier transport within the perovskite layer primarily occurs through the 3D-like phase, which forms a percolating network vertically in the solar cell device, as shown in Figure 1.2(b).[10]

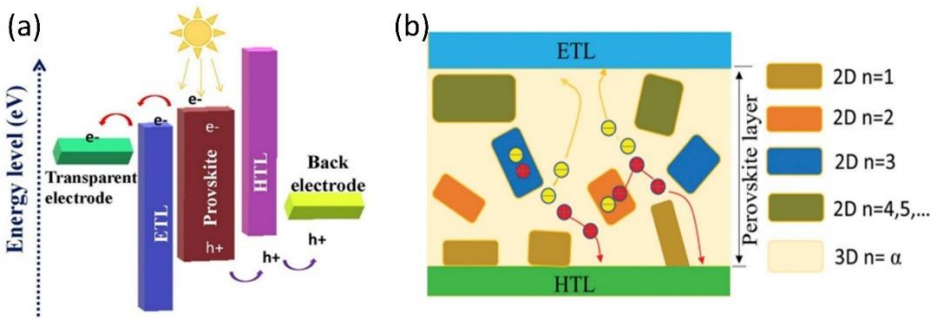

Figure 1.2 a) Generic energy diagram and charge transfer pathway (profile of electrical potential), in a thin-film perovskite solar cell under illumination b) Planar device structure demonstrating the generation and flow of charge carriers in solar cells based on 3D perovskite materials.

1.2.2 Why perovskite solar materials and solar cells?

Numerous photoactive materials, including dye (N719),[16] quantum dots,[17] organic polymers with high electron densities,[18] silicon, perovskites, and others, have been suggested for use in optoelectronic devices. However, only silicon and perovskite have demonstrated economically

feasible energy conversion efficiencies among all these materials. Silicon stands out due to its remarkable stability, lasting over 22 years with less than a 10% decrease in power conversion efficiency (PCE). Nevertheless, its production process is complex, requiring a purity level of over 99.9%, being energy-intensive, and lacking environmental friendliness.[19] Additionally, the highly crystalline nature of silicon solar material and the absence of technology enabling its solution processing into flexible fiber-shaped devices have redirected attention towards perovskite material, especially for photon-to-energy conversion in wearable/fiber-shaped devices.

Perovskites have shown great potential in solar devices, competing favorably with solar silicon materials in terms of power conversion efficiency, production costs, and production diversity. Over a span of approximately 12 years, the power conversion efficiency (PCE) in perovskite solar cells has rapidly improved from 3.8%[20] to a maximum reported value of around 25.7% and beyond on flat/planar substrates.[21] Additionally, fiber-shaped perovskite devices have recently reached a maximum PCE of 15.7%,[22] gradually catching up to their planar counterparts, as depicted in Figure 1.3(a). These fiber-shaped devices consist of at least one stimuli-responsive layer sandwiched between functional layers, as illustrated in Figure 1.3(b). In order to create optoelectronic fiber-shaped devices, it is necessary to incorporate a photoactive material capable of generating charge carriers upon receiving photons.

Organic-inorganic hybrid perovskites are considered the most promising materials for low-temperature solution processable, next-generation photovoltaics. This is due to their exceptional intrinsic properties, including a low hole-electron exciton binding energy ranging between 50~150 meV,[23] extended charge carrier lifetimes surpassing 446 ns,[24] superior charge carrier transfer properties (24~135 cm^{-2} $V^{-1}s^{-1}$), and diffusion lengths exceeding 175μm.[25] Perovskites also exhibit exceptional interfacial charge transfer ability,[26] shallow surface defects, and remarkable structural defect tolerance, thanks to the ionic bonds holding the perovskite molecules together. Moreover, perovskites have high absorption coefficients resulting from s-p antibonding and beneficial narrow band gaps that decrease as the dimensionality increases from 2D to 3D perovskite material configurations.[27] Compared to other photovoltaic technologies, perovskites have the lowest internal energy loss, second only to crystalline silicon solar cells. These enticing features have prompted extensive research into this emerging class of materials

for applications such as solar cells, light-emitting diodes, light-emitting transistors, photo-memories, and more.[28]

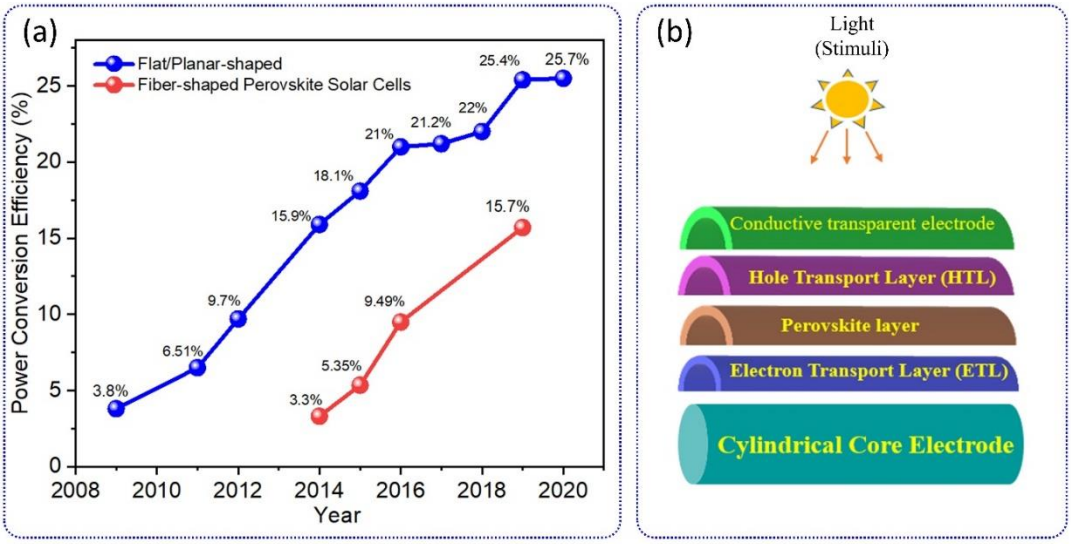

Figure 1.3 a) Variation of power conversion efficiency with time for Flat/planar and fiber-shaped perovskite solar cells. The Plotted data for planar/flat and fiber-shaped perovskite solar cells was extracted from references[21] and references, respectively.[22] b) Schematic illustration of a p-i-n layer-by-layer architecture in fiber-shaped perovskite solar cells.

1.3 Fiber-shaped devices for renewable energy harvesting

In the 21st century and beyond, the rise of smart living and the internet of things (IoT) has created a need for wearable, low-cost, and highly efficient energy supply sources. These self-powered wearables are crucial for sustaining advancements in technology, including robotics, wearable sensing, display, and artificial intelligence.[29] The demand for energy in wearable electronics has led to the development of fiber-shaped single-function and multifunctional self-powering devices. Thanks to advancements in material synthesis, high-performance device architectures, and nanotechnology, these devices have become smaller and more wearable.[30] The increasing demand for electronic devices is driven by their miniaturization, wearability, and multifunctionality. As a result, the market for wearable electronics is projected to grow at a compound annual growth rate of 18% between 2021 and 2026, reaching a market value of USD

265.4 billion.[31] Textiles are made up of fiber-shaped structures, making them ideal for integrating highly functional fiber devices. This integration allows for combining the functionality of new devices with the essential properties of textile structures, such as breathability, flexibility, stretchability (especially in knits), and ease of integration through weaving, knitting, twisting, and embroidery.

In recent years, there have been numerous reports on the development of fiber-shaped devices for various applications such as wearable communication, display, sensing, medical applications, energy storage, and harvesting.[32] Additionally, successful attempts have been made to create fabric forms and integrated multifunctional versions of these wearable devices. For instance, Shi et al.[33] presented a textile that serves as a large surface area display integrated with multiple electronic systems. They achieved this by weaving highly transparent and conductive melt-spun ionic-liquid-doped polyurethane as the weft fibers, along with luminescent warp and cotton yarns to create electroluminescent units within the textile itself. The team also demonstrated the integration of a textile-based keyboard and a fiber-shaped power supply, making the system a comprehensive communication tool.[33]

1.3.1 Technical benefits of the fiber geometry in solar cells

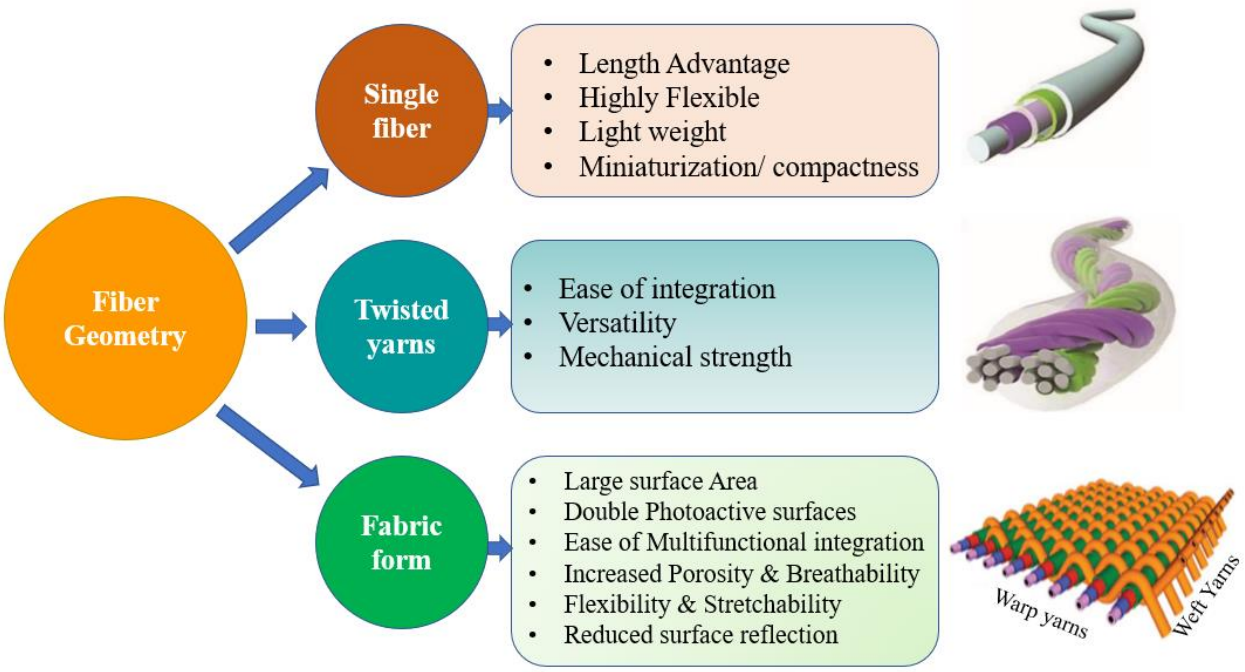

Figure 1.4. A schematic showing the breakdown of different fiber assemblies and their associated benefits in optoelectronic devices.

Fiber geometry is now commonly used in three main types of electronic devices: energy storage, energy harvesting, and devices for functional purposes. The advantages of fiber-shaped optoelectronics are outlined in Figure 1.4.[34] These devices have a high length to diameter ratio, which gives them beneficial mechanical properties like increased bending and flexibility. As a result, they are well-suited for wearable and textile applications. The bending rigidity of a fiber-shaped device in a specific direction is directly related to the fourth power of its radius in that direction along its cross-section, as shown in equation 1.1.[35] Therefore, fiber-shaped perovskite solar cells, with their reduced length to diameter ratio, have minimal bending rigidity (increased flexibility) in all directions. This characteristic is highly desirable for wearable devices (Fig. 1.5a-top). In contrast, planar or flat optoelectronics have different radii measurements along their central axis, as demonstrated in Figure 1.5a-bottom. As a result, they are stiffer along the axis with diameter D2 than along the axis with diameter D1. Bending, as a mechanical property of a fiber-shaped device, influences physical properties like curl, crimp, and skew of the fabric

optoelectronic devices. It also determines properties like formability, crease recovery, drapability, and tailorability.[35]

$I \propto r^4$ …….. Eqn 1.1

Where; I - is the bending rigidity

r- radius in a given direction along the cross-section

For solar cells and other optoelectronic devices, the available surface area for light exposure is highly influential in determining and boosting the output power density and overall performance.[36]

The fiber-shaped perovskite solar cells (FSPSCs) have a circular cross-section, which provides a significant photoactive surface area. This area can be calculated using the mathematical expression, where D represents the diameter of the device, and L represents its photoactive length. However, when exposed to uni-directional light, only half of the FSPSC's surface area is illuminated, leaving the opposite half unexposed. As a result, the effective active area is reduced by almost half. Nevertheless, when the optoelectronic fiber devices are woven or knitted, the resulting fabric surfaces become convoluted due to the interlacing and intermeshing of the fiber devices. This leads to curved sections of the FSPSCs on the fabric optoelectronic device's surface. These curved sections, technically increase the available photoactive surface area of the fabric optoelectronic device when exposed to uni-directional light, compared to their flat counterparts.

It has been reported that fiber-shaped solar cells are can maintain a consistent photon to energy efficiency even when the angle of incidence of the incoming light changes. Qui et al.[37] and Balilonda et al.[38] conducted studies on the power conversion efficiency (PCE) of fiber-shaped perovskite solar cells under different angles of incidence. Their findings showed that the PCE of the fiber devices remains nearly constant when the incident angle of light is varied from 0 to 180^o. This suggests that there is little correlation between the angle of incidence and the photovoltaic performance, which is a promising indication of the performance of self-powered

textiles. The only exception observed was at 90º, where there is a sudden increase in PCE due to the light source illuminating almost all surfaces of the fibers at this angle.

1.3.2 Advantages of solar fabrics from a technical standpoint

Figure 1.5(b), illustrates the advantages of using optoelectronic devices made from woven or knitted fabrics for integration, due to their loose structures. These fabric structures have the unique feature of having both the technical face and the technical back being photoactive.[39] This means that these textile structures can harvest light energy from multiple directions, as shown in Figure 1.5(c). The rough texture of the fabric surface, caused by its loopy and convoluted nature, reduces the immediate surface reflections of the incident light. This occurs because the rough texture permits successive inter-yarn light reflections, increasing the chances for the photoactive materials incorporated in the optoelectronic yarns to absorb photon energy (refer to Figure 1.5c). The improved optical interaction and absorption advantage resulting from the uneven fabric surface topography (fabric texture) is similar to the technique of surface texturization used for silicon solar cells. This technique involves etching the surface to reduce surface reflection, enhance incident light-harvesting capability, and improve the overall efficiency of the devices.[40]

Converting fiber-shaped devices into knitted structures enhances their stretchability when knitted, either in the warp or weft directions, depending on the knitting technique used.[41] The stretchability of a knitted fabric comes from the relaxed loops in its structure, which easily adjust their length to accommodate changes in the fabric's dimensions when subjected to tension. Stretchability is an important property in the field of textiles and wearable devices, as it allows for a better fit, improved durability, and increased comfort for the wearer. The ability of fiber-shaped optoelectronics to be knitted, woven, or twisted with other fiber-shaped devices expands the possibilities for integrating them into multifunctional structures. For example, Zhang et al.[42] demonstrated this by weaving fiber-shaped solar cells with fiber-shaped batteries to create a photo-rechargeable fabric, showcasing the seamless integration made possible by the fiber geometry. Chen et al. also developed a hybrid textile that combined fiber solar cells and triboelectric nanogenerators yarns, resulting in a lightweight energy textile capable of harnessing energy from multiple sources.[43] However, it should be noted that the previously reported fiber-

shaped devices and fabrics lack sufficient bending stability, and demonstrate very low power conversion efficiency. These limitations can be overcome by developing stable and highly efficient fiber-shaped perovskite solar cells.

The global annual garment production is estimated to be between 80-150 billion pieces per year, which averages to about 20 pieces per person. To address the energy supply problem for wearable devices, the proposed solution is to combine textile manufacturing and energy harvesting to create autonomous energy-generating textiles. This approach can alleviate the energy demand of mobile and wearable electronics (3416.4~10,249.2 GW per annum),[36] easing the strain on main power grids primarily used for production in different economies. The emergence of energy harvesting textiles, along with the growing need for interconnected devices in the Internet of Things (IoT),[44] is expected to have a significant impact on the convergence of textiles and electronics. This convergence will lead to the development of e-textiles and smart textiles, which not only serve traditional textile functions but also find applications in advanced technological fields.

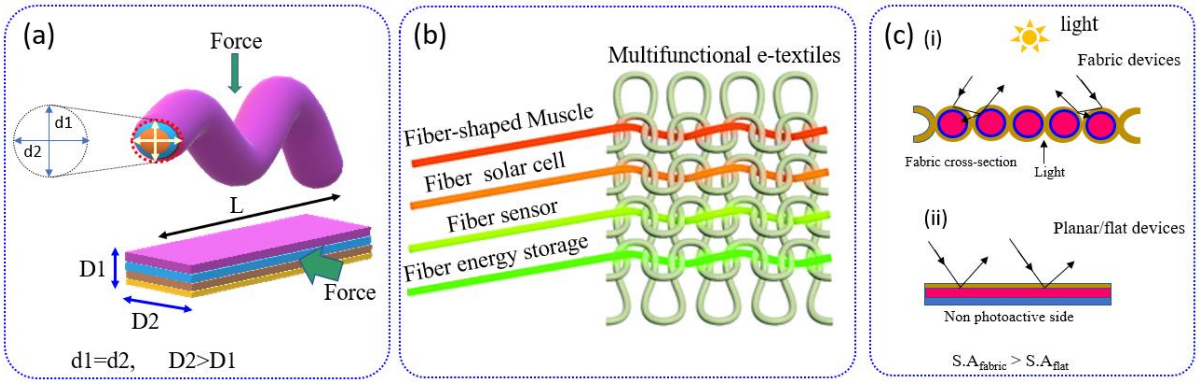

Figure 1.5. a) Schematic illustration of fiber-shaped and planar devices, demonstrating the effect of diameter to the minimum force required to cause bending. b) Multifunctional integration achievable with fabric and textile structures.[45] c) Schematic diagrams illustrating i) the interaction of light rays with fabric devices i) with flat/planar all solid devices.

1.4 Problem statement

As the demand for renewable energy sources for wearable applications continues to grow, the development of high-performance fiber-shaped perovskite solar cells and solar fabrics presents a

promising solution. Perovskite solar materials offer advantages such as solution processability, high power conversion efficiency (PCE), and superior material photovoltaic properties. Meanwhile, fiber-shaped solar devices offer flexibility, length advantage, ease of multifunctional integration and lightweight characteristics. However, fiber-shaped perovskite solar cells still face challenges such as perovskite material toxicity, low power conversion efficiency compared to their planar counterparts, and layer deposition challenges on circular substrates. Other challenges include loss of efficiency due to device bending or twisting, oxidation of tin-based perovskite material and material degradation (initiated by moisture, heat and air). These challenges need to be addressed in order to fully leverage the potential of fiber-shaped perovskite solar cells for practical applications.

When considering the fiber geometry in perovskite fiber-shaped solar cells, there are several disadvantages to take into account, and these include[42];

I. Limited Surface Area: The small surface area of the fiber geometry may limit the amount of perovskite material that can be deposited onto the solar cell, potentially reducing its efficiency in converting sunlight into electricity.
II. Mechanical Stability: The fiber shape may result in mechanical instability compared to traditional flat solar cells, making them more vulnerable to damage or breakage, which can affect their overall performance and lifespan.
III. Light Absorption: The orientation of the fibers may not always be optimal for capturing sunlight, leading to lower light absorption and conversion efficiency compared to flat solar cells that can be positioned to receive maximum sunlight exposure.
IV. Manufacturing Complexity: The fabrication process for fiber-shaped solar cells can be more complex and challenging compared to traditional solar cells, which can result in higher production costs and potential quality control issues.
V. Interconnection Challenges: Connecting multiple fiber-shaped solar cells to form a larger solar panel can be more difficult due to the unique geometry of the fibers, potentially leading to increased resistance and power losses in the overall system.

Despite these disadvantages, ongoing research and development efforts are focused on addressing these challenges to improve the efficiency and practicality of perovskite fiber-shaped solar cells.

1.5 Aims and Objectives

1.5.1 Overall aims

Fiber-shaped perovskite solar cells are seen as a top-pillar in solar energy harvesting for wearable applications. In planar-shaped devices, perovskite solar cells have demonstrated efficiencies (>26.1%) higher than the market dominant silicon solar cells, and the efficiency in fiber-shaped perovskite solar cells is gradually following the same footsteps of their planar counterparts. Still, fiber-shaped solar cells come with numerous advantages such as increased flexibility, light weight, ease of multi-functional integration and weave-ability into large area solar fabrics.

This research aims to realize and demonstrate toxic-free (Sn-based), highly efficient, flexible, and stable fiber-shaped perovskite solar cells suitable for wearable and textile applications. The research focuses on modifying the molecular structure of perovskite material to realize chemically stable, photovoltaically efficient, and non-toxic material configurations. Due to the low stability of Sn-based perovskite materials originating from the oxidation of Sn^{2+} to Sn^{4+}, we extensively investigated the impact of antioxidants on the stability and photovoltaic performance of Sn-based perovskite solar materials. The resulting stable and efficient fiber-shaped perovskite solar cells will be studied for their performance under continuous bending, when subjected to different temperature conditions, etc. The perovskite solar yarns will be woven or knitted to realize stable and efficient solar fabrics.

1.5.2 Specific objectives

1. To address the toxicity challenge in perovskite solar materials.
2. To overcome the high temperature processing requirement of 2D3D hybrid perovskite materials and the material deposition challenge on fiber-type substrates.
3. To enhance the power conversion efficiency of fiber-type perovskite solar cells.
4. To design fiber-type perovskite solar cells with bending stability and extended service lifetime.

5. To achieve large area and high-performance solar fabrics assembled from fiber-shaped perovskite solar cells.

By realizing these objectives, we aim to overcome the stability, efficiency, toxicity and flexibility challenges in fiber-shaped perovskite solar cells, and pave a way for high performance flexible solar cells for wearable applications.

1.6 Organization of this thesis

The chapters of this thesis are organized as follows:

Chapter 1: Starts with an overview of the increasing global energy demand, the challenges associated with conventional energy sources, and the genesis of the renewable energy sources. The chapter introduces perovskite material molecular structure, mechanism of perovskite photoelectric conversion, and the advantages of perovskite material over other photovoltaic materials. The chapter further introduces fiber-shaped perovskite solar cells, and the technical benefits of the fiber geometry in solar cell, and the challenges facing fiber-type perovskite solar cells (in a problem statement). In the end, the objectives, organization of the thesis and conclusion are presented.

Chapter 2: Reviews the literature about perovskite solar cell materials and device design, the genesis of perovskite solar cells, and the research progress in fiber-shaped perovskite solar cells, with a comprehensive study of related works. This chapter further reviews the current challenges facing fiber-shaped perovskite solar cells and points out the possible research directions to overcome the challenges. Details of work in chapter 1 and chapter 2 were published in our review paper.

Chapter 3: Presents a study on the use of chloride ions to speed up the reaction between 3D and 2D perovskite molecules so as to achieve high quality 2D3D hybrid perovskite molecules, under low reaction temperatures and time. This chapter further presents the incorporation of the optimized 2D3D perovskite material into a double twisted fiber-shaped solar cell design. Characterizations of the fiber-shaped solar cell for photovoltaic performance, temperature &

bending stability, performance lifetime etc., are also presented. Details of the work in this chapter were also published in our research paper.

Chapter 4: Reports an investigation on the use of a double redox reaction antioxidant vanillin to enhance the performance and efficiency of Sn-based flexible (Fiber-type) perovskite solar cells. This chapter elaborates doping of the 2D3D Sn-based perovskite material synthesized in chapter 4 with antioxidant vanillin, accompanied with thorough material optimization and characterization. The optimized material is incorporated in a 1-dimensional rectangular cross-sectional fiber-type flexible solar cell, followed by thorough characterization. This chapter further presents the use of microwave irradiation as a novel approach to recover lost efficiency in ageing perovskite solar cells as a strategy to overcome frequent solar cell recycling. Details of the work in this chapter were also published in our research paper.

Chapter 5: Presents an investigation of the performance of fiber-type perovskite solar cells assembled into woven solar fabrics with acrylic yarns. Herein, simple assemblies of plain, twill and satin woven solar fabrics are demonstrated to prove the concept, followed by subsequent perovskite solar fabric characterization.

Chapter 6: Presents a comprehensive overview of flexible fiber-type Sn-based perovskite solar cells, and the use of 2D3D hybrid perovskite materials. The chapter further elaborates the impact of doping perovskite with antioxidants and other strategies to improve the stability and photovoltaic performance of flexible perovskite solar cells. Additionally, this chapter also includes a brief summary of the challenges encountered in our study, and the possible future research directions in this area.

1.7 Conclusion

In conclusion, the global energy demand continues to increase significantly in tandem with the rise in global population, posing challenges for conventional energy sources in terms of sustainability and environmental impact. The shift towards renewable energy sources, such as next-generation solar cells like perovskite and dye-sensitized cells, offers a promising solution to

meet this growing demand. Perovskite solar cells, in particular, have emerged as a game-changer in the field of solar energy due to their material advantages and impressive efficiency progress. The introduction of fiber-shaped perovskite solar cells further enhances their utility, offering unique advantages in terms of flexibility and ease of integration into various applications. As we delve deeper into the development and implementation of these innovative solar technologies, it becomes evident that they hold immense potential for revolutionizing the energy landscape and driving us towards a more sustainable future. By harnessing the power of next-generation solar cells, we can strive towards achieving a cleaner, more efficient, and environmentally friendly energy ecosystem for generations to come.

1.8 References

1. Balilonda, A., Q. Li, M. Tebyetekerwa, R. Tusiime, et al., Perovskite solar fibers: current status, issues and challenges. Adv. Fiber Mater, 2019. **1**: 101-125.

2. Balilonda, A., Z. Li, Y. Fu, F. Zabihi, et al., Perovskite fiber-shaped optoelectronic devices for wearable applications. J. Mater. Chem. C, 2022. **10**(18): 6957-6991.

3. Tao, M., Inorganic photovoltaic solar cells: silicon and beyond. The Electrochemical Society Interface, 2008. **17**(4): 30.

4. Hayat, M.B., D. Ali, K.C. Monyake, L. Alagha, et al., Solar energy—A look into power generation, challenges, and a solar-powered future. International Journal of Energy Research, 2019. **43**(3): 1049-1067.

5. Kabir, E., P. Kumar, S. Kumar, A.A. Adelodun, et al., Solar energy: Potential and future prospects. Renewable Sustainable Energy Reviews, 2018. **82**: 894-900.

6. Djurišić, A., F. Liu, A.M. Ng, Q. Dong, et al., Stability issues of the next generation solar cells. Physica status solidi –Rapid Research Letters, 2016. **10**(4): 281-299.

7. Atou, T., H. Chiba, K. Ohoyama, Y. Yamaguchi, et al., Structure determination of ferromagnetic perovskite BiMnO3. Journal of Solid State Chemistry, 1999. **145**(2): 639-642.

8. Ekanayake, P., J.C.M. Lim, T. Meyer, and M.K. Nazeeruddin, Perovskite solar cells. Scientia Bruneiana, 2017. **16**(1).

9. Tai, Q., P. You, H. Sang, Z. Liu, et al., Efficient and stable perovskite solar cells prepared in ambient air irrespective of the humidity. 2016. **7**(1): 1-8.

10. Lin, Y., Y. Fang, J. Zhao, Y. Shao, et al., Unveiling the operation mechanism of layered perovskite solar cells. Nat. Commun, 2019. **10**(1): 1-11.

11. Xu, F., T. Zhang, G. Li, and Y. Zhao, Synergetic Effect of Chloride Doping and CH3NH3PbCl3 on CH3NH3PbI3− xClx Perovskite-Based Solar Cells. ChemSusChem, 2017. **10**(11): 2365-2369.

12. Wang, X., Y. Ling, X. Lian, Y. Xin, et al., Suppressed phase separation of mixed-halide perovskites confined in endotaxial matrices. Nature communications, 2019. **10**(1): 695.

13. Canicoba, N.D., N. Zagni, F. Liu, G. McCuistian, et al., Halide Perovskite High-k Field Effect Transistors with Dynamically Reconfigurable Ambipolarity. ACS Materials Letters, 2019. **1**(6): 633-640.

14. Christe, K.a.S., Stefan (2021, June 14). Iodine. Encyclopedia Britannica. https://www.britannica.com/science/iodine.

15. Zhang, C.C., Z.K. Wang, S. Yuan, R. Wang, et al., Polarized ferroelectric polymers for high-performance perovskite solar cells. Adv. Mater, 2019. **31**(30): 1902222.

16. Liu, Q., N. Gao, D. Liu, J. Liu, et al., Structure and photoelectrical properties of natural photoactive dyes for solar cells. Applied Sciences, 2018. **8**(9): 1697.

17. Gao, X., X. You, X. Zhao, W. Li, et al., Flexible fiber-shaped liquid/quasi-solid-state quantum dot-sensitized solar cells based on different metal sulfide counter electrodes. Applied Physics Letters, 2018. **113**(4): 043901.

18. Zou, D., D. Wang, Z. Chu, Z. Lv, et al., Fiber-shaped flexible solar cells. Coord. Chem. Rev, 2010. **254**(9-10): 1169-1178.

19. Dunlop, E.D. and D. Halton, The performance of crystalline silicon photovoltaic solar modules after 22 years of continuous outdoor exposure. Progress in photovoltaics: Research Applications, 2006. **14**(1): 53-64.

20. Kojima, A., K. Teshima, Y. Shirai, and T. Miyasaka, Organometal halide perovskites as visible-light sensitizers for photovoltaic cells. J. Am. Chem. Soc, 2009. **131**(17): 6050-6051.

21. Hou, Y., E. Aydin, M. De Bastiani, C. Xiao, et al., Efficient tandem solar cells with solution-processed perovskite on textured crystalline silicon. Science, 2020. **367**(6482): 1135-1140.

22. Li, Q., A. Balilonda, A. Ali, R. Jose, et al., Flexible Solar Yarns with 15.7% Power Conversion Efficiency, Based on Electrospun Perovskite Composite Nanofibers. Solar RRL, 2020. **4**(9): 2000269.

23. Koutselas, I., L. Ducasse, and G.C. Papavassiliou, Electronic properties of three-and low-dimensional semiconducting materials with Pb halide and Sn halide units. J. Condens. Matter Phys, 1996. **8**(9): 1217.

24. Zhang, M., H. Yu, M. Lyu, Q. Wang, et al., Composition-dependent photoluminescence intensity and prolonged recombination lifetime of perovskite CH 3 NH 3 PbBr 3− x Cl x films. Chem commun, 2014. **50**(79): 11727-11730.

25. Dong, Q., Y. Fang, Y. Shao, P. Mulligan, et al., Electron-hole diffusion lengths> 175 μm in solution-grown CH3NH3PbI3 single crystals. Science, 2015. **347**(6225): 967-970.

26. Marchioro, A., J. Teuscher, D. Friedrich, M. Kunst, et al., Unravelling the mechanism of photoinduced charge transfer processes in lead iodide perovskite solar cells. Nat. Photonics, 2014. **8**(3): 250-255.

27. Yin, W.-J., J.-H. Yang, J. Kang, Y. Yan, et al., Halide perovskite materials for solar cells: a theoretical review. J. Mater. Chem. A, 2015. **3**(17): 8926-8942.

28. Chen, J.Y., Y.C. Chiu, Y.T. Li, C.C. Chueh, et al., Nonvolatile perovskite-based photomemory with a multilevel memory behavior. Adv. Mater, 2017. **29**(33): 1702217.

29. Ling, Y., T. An, L.W. Yap, B. Zhu, et al., Disruptive, soft, wearable sensors. Adv. Mater, 2020. **32**(18): 1904664.

30. Hasan, M.N., S. Sahlan, K. Osman, and M.S. Mohamed Ali, Energy Harvesters for Wearable Electronics and Biomedical Devices. Adv. Mater. Technol, 2021. **6**(3): 2000771.

31. Masoodi, F. and B.A. Pandow, Internet of things: financial perspective and its associated security concerns. International Journal of Electronic Finance, 2021. **10**(3): 145-158.

32. Ando, H., M. Sugimoto, and T. Maeda, Wearable moment display device for nonverbal communications. IEICE transactions on information systems, 2004. **87**(6): 1354-1360.

33. Shi, X., Y. Zuo, P. Zhai, J. Shen, et al., Large-area display textiles integrated with functional systems. Nature, 2021. **591**(7849): 240-245.

34. Shao, G., R. Yu, X. Zhang, X. Chen, et al., Making Stretchable Hybrid Supercapacitors by Knitting Non-Stretchable Metal Fibers. Adv. Funct. Mater, 2020. **30**(35): 2003153.

35. Park, J.-W. and A.-G. Oh, Bending rigidity of yarns. Textile Research Journal, 2006. **76**(6): 478-485.

36. Balilonda, A., Q. Li, M. Tebyetekerwa, R. Tusiime, et al., Perovskite solar fibers: current status, issues and challenges. Adv. Fiber Mater, 2019. **1**(2): 101-125.

37. Deng, J., L. Qiu, X. Lu, Z. Yang, et al., Elastic perovskite solar cells. J. Mater. Chem. A, 2015. **3**(42): 21070-21076.

38. Balilonda, A., Q. Li, X. Bian, R. Jose, et al., Lead-free and electron transport layer-free perovskite yarns: Designed for knitted solar fabrics. J. Chem. Eng, 2021. **410**: 128384.

39. Qiu, L., J. Deng, X. Lu, Z. Yang, et al., Integrating perovskite solar cells into a flexible fiber. Angew. Chem. Int. Ed, 2014. **53**(39): 10425-10428.

40. Tang, H., S. Ma, Y. Lv, Z. Li, et al., Optimization of rear surface roughness and metal grid design in industrial bifacial PERC solar cells. Solar Energy Materials & Solar Cells, 2020. **216**: 110712.

41. Zhang, M., C. Wang, X. Liang, Z. Yin, et al., Weft-knitted fabric for a highly stretchable and low-voltage wearable heater. Adv. Electron. Mater, 2017. **3**(9): 1700193.

42. Zhang, N., F. Huang, S. Zhao, X. Lv, et al., Photo-rechargeable fabrics as sustainable and robust power sources for wearable bioelectronics. Matter, 2020. **2**(5): 1260-1269.

43. Chen, J., Y. Huang, N. Zhang, H. Zou, et al., Micro-cable structured textile for simultaneously harvesting solar and mechanical energy. Nat. Energy, 2016. **1**(10): 1-8.

44. Wei, J., How Wearables Intersect with the Cloud and the Internet of Things: Considerations for the developers of wearables. IEEE Consumer Electronics Magazine, 2014. **3**(3): 53-56.

45. Seyedin, S., T. Carey, A. Arbab, L. Eskandarian, et al., Fibre electronics: towards scaled-up manufacturing of integrated e-textile systems. Nanoscale, 2021. **13**(30): 12818-12847.

Chapter 2: Literature Review

2.1 Introduction

Perovskite solar cells, like other solar cells generate charge carriers when the perovskite layer, the photoactive component of the cell receives enough photon energy. This energy helps the charge carriers overcome the nuclear electrostatic attractions. Any surplus energy allows the electrons to move through the materials' bandgap and reach the conduction band. Perovskite solar cells, regardless of their shape, consist of various functional layers that surround the photoactive layer.[1] Ensuring the quality of these layers and their interfaces is crucial to achieving high power conversion efficiency and fill factor in the solar device. Understanding the individual components and the device mechanism is important for efficient electron and hole generation, as well as their transfer to the electrodes with minimal recombination. Therefore, the perovskite layer, which serves as the light absorber and is responsible for charge carrier generation, separation, and transfer, is a critical area of research. Additionally, the selection of electron and hole transport materials, as well as the quality of the interfaces they form with the perovskite layer, play a crucial role in creating an internal electric field force that minimizes recombination and drives the charge carriers. Researchers in the field of wearable and fiber-type perovskite solar cells, are particularly interested in non-toxic perovskite materials, highly flexible electrodes, and polymeric functional layers.[2]

In this chapter, we discuss the available material options for different functional layers of perovskite solar cells, the genesis of perovskite solar cells in general, and the recent developments in fiber-type solar cells. Additionally, we present a comprehensive discussion about the challenges facing fiber-shaped perovskite solar cells. This comprehensive discussion aims to enlighten the key aspects of fiber-shaped perovskite solar cells and serve as a beneficial roadmap for future research endeavors in this field.

2.2 Perovskite solar cell materials and design

A typical perovskite solar cell is made-up of several layers, including a photoactive layer (perovskite) sandwiched between an electron transport layer (ETL) and a hole transport layer (HTL). Regardless of its geometry, the cell has a transparent electrode on one end and a counter electrode on the other end. The most commonly used conducting metal oxide for the transparent electrode are Indium Tin Oxide (ITO) and fluorine-doped tin oxide (FTO), which are known as transparent conductive oxide - TCO materials.[3] In the case of fiber-shaped perovskite solar devices, transparent conductive materials are usually thin, translucent layers of gold[4] or transparent CNT yarns.[5] Sometimes, the primary yarn is twisted with a non-transparent silver or carbon yarn to serve as the top electrode.[6]

For planar rigid solar cells, the traditional electron and hole transport layers have been TiO_2 and Spiro-OMeTAD (2,2′,7,7-tetrakis(N,N-di(4-methoxyphenyl)amino)-9,9′Spiro-bifluorene).[7] However, researchers have explored different alternatives, such as organic composites, co-polymers, carbon allotropes, and alternative metal oxides (listed in Table 2.1), in order to improve the stability, cost-effectiveness, and efficiency of perovskite devices.

Table 2.1 Perovskite solar cell materials, possible applications in the solar cells, and the estimated energy bands.

Layer Function	Material Nature	Examples	LUMO (eV)	HOMO (eV)	Ref
Back electrodes		FTO	-4.7		[8]
		ITO	-4.4		[9]
Electron Transport Layer	Metal Oxides	ZnO	-4.4	-7.8	[10]
		TiO_2	-4.1	-7.3	[11]
		SnO_2	-4.5	-7.8	[12]
	Conjugated polymer	PCBM	-4.33	-6.16	[13]
Perovskites	Methylammonium-based	$MAPbI_3$	-3.93	-5.43	[14]
	Formamidium -based	$FAPbI_3$	-4.0	-5.4	[15]
	Bromine based	$MAPbBr_3$	-3.36	-5.58	[16]
	Cesium-based	$CsPbIBr_2$	-3.93	-6.0	[10]
		$CsPbI_3$	-3.6	-5.69	[17]

Hole Transport Layer (HTL)	Small molecules	Spiro-OMeTAD	-2.3	-5.2	[18]
		Pm- Spiro-OMeTAD	-2.3	-5.3	[19]
		Po- Spiro-OMeTAD	-2.2	-5.2	[19]
	Polymer materials	TTF-1	-1.98	-5.05	[20]
		P3HT	-3.0	-5.0	[20]
		PTTA	-1.8	-5.1	[21]
		PEDOT: PSS	-2.0	-5.2	[22]
	Inorganic Materials	NiOx	-1.80	-5.2	[23]
		$CuSbS_2$	-3.85	-5.25	[14]
		CuSCN	-1.5	-5.3	[24]
		CuI	-2.2	-5.3	[25]
		Cu_2O	-3.2	-5.37	[26]
Top Electrode	Metallic electrodes	Carbon	-5.1		[27]
		Gold	-5.1		
		Cupper	-5.1		
		Silver	-4.5		

2.3 Genesis of perovskite solar cells

The use of perovskite materials in light-harvesting was initially studied in dye-sensitized solar cells. In a 2009 study,[28] it was discovered that when methylammonium lead halide perovskite was absorbed on a nanocrystalline TiO_2 surface, it generated a photocurrent with a power conversion efficiency (PCE) of approximately 3.8%. Expanding on this research, Park et al.[29] optimized the thickness of the TiO_2 electron transport layer and treated it with $(PbNO_2)_2$, resulting in a solar cell with a PCE of around 6.51%. However, research on first-generation liquid-based perovskite solar cells declined due to the rapid degradation of perovskite materials in liquid electrolytes.

In 2012, Kim et al.[30] developed a solid-state perovskite solar cell that was relatively stable, and had an efficiency of approximately 9.7%. This groundbreaking design involved the use of a solid-state hole transporter called Spiro-OMeTAD, along with solid-state halide and mixed halide perovskites ($CH_3NH_3PbI_{3-x}Cl_x$) as the photoactive layer. These were coated on a thin film

of TiO_2, which served as the electron transport layer. In 2015, Zhang et al.[31] successfully created pinhole-free perovskite films using a one-step coating method followed by annealing. This advanced technique achieved a power conversion efficiency (PCE) of 15.2% using non-halide ($PbAc_2$). Zhou et al,[32] further improved perovskite devices in 2015 by altering the band alignment of the hole transport layer (HTL) and electron transport layer (ETL), resulting in a remarkable PCE of 19.3%. In 2016, Bi et al. introduced a method for producing high-quality perovskite films using poly(methyl methacrylate) (PMMA) as a template to control nucleation and crystal development.[33] This approach yielded a certified PCE of 21%. Shin et al. (2017) explored the use of a superoxide colloidal solution route to prepare an LBSO electrode under gentle conditions (below 300°C). The steady-state PCE of the perovskite solar cells produced with LBSO and methylammonium lead iodide ($MAPbI_3$) reached 21.2%. Since 2017, the efficiency of planar devices has been gradually increasing, with the current highest recorded efficiency being 25.5% and above.[34]

2.4 Progress in fiber-shaped perovskite solar cells

Unlike fossil fuels, solar energy is abundant, nearly inexhaustible, and environmentally friendly. Therefore, developing highly efficient solar cells that can be used in a wide range of applications is a viable solution to the global energy challenge and the issue of global warming. This section provides a summary of key developments in fiber perovskite solar cells.[35]

Fiber-shaped solar cells have the potential to pave the way for next-generation solar fabrics and self-powered wearable electronic devices. The improved performance of flat/planar multi-junction perovskite solar cells in terms of power conversion efficiency (PCE), combined with affordable low temperature and solution processing techniques, has led to exploration of different geometries such as fiber-shaped yarns for various applications.[36] However, due to the high PCE achieved by flat geometry perovskite solar cells, advancing research in fiber-shaped devices is seen as the best alternative to replace or surpass the limited maximum PCE of dye-sensitized solar yarns, which is currently 10%.[37] Additionally, fiber-shaped devices face challenges related to packaging and liquid electrolyte leakages. Therefore, the development of efficient fiber-shaped perovskite solar cells is currently a major focus.[38]

2.4.1 Coaxial and double-twisted fiber-shaped perovskite solar cells

Fiber-shaped perovskite solar cells are mainly classified into two categories; coaxial and double twisted. Coaxial solar cells are compact, and highly efficient, but complex to assemble. On the other hand, double twisted cells are more flexible and easier to assemble, but have low PCE. Qiu et al.[39] developed a revolutionary fiber-shaped perovskite cell using a thin stainless-steel fiber as the base and positive electrode. The steel fiber was first dipped in a TiO_2 solution and then baked at 400°C to create a compact n-type coating of TiO_2. A second dip-coating in a TiO_2 nanoparticle solution resulted in the formation of a mesoporous TiO_2 layer. The $CH_3NH_3PbI_3$ perovskite layer was then applied using a dip-coating technique, allowing it to penetrate the nanocrystal TiO_2 mesopores. Finally, the hole-transport layer was applied on top of the perovskite layer.

Figure 2.1 a(i) showcases a groundbreaking perovskite solar cell with an average diameter of 10 nm, which has been twisted with transparent multi-walled carbon nanotubes. The scanning electron microscope study in Figure 2.1 b(ii) confirms the arrangement of layers mentioned above. The fiber device could be woven into a fabric for perovskite solar cells, exhibiting the following characteristics: PCE of 3.3%, V_{OC} of 0.664 V, I_{SC} of 10.2 mA.cm^2, and FF of 0.487. The resulting yarn geometry allows for easy integration and application.[39] However, the stainless-steel core of the yarn increases costs and reduces flexibility. The authors also noted that depositing a thick layer of compact TiO_2 material would lead to difficulties, such as an increase in series resistance to the movement of charge carriers and a decrease in the fill factor of the solar yarn, which ultimately affects the low PCE. Furthermore, larger films are more prone to shattering into multiple pieces, especially when the fiber is twisted multiple times, making them susceptible to crack formation and spread. Conversely, ultrathin TiO_2 films with a high number of flaws result in shunts, shorter carrier lifetimes, and reduced photovoltaic efficiency. Additionally, it remains challenging to obtain compact perovskite layers with large crystal sizes on the curved surfaces of fiber electrodes.[39]

The main challenge highlighted in earlier reports was the difficulty of uniformly depositing mesoporous TiO_2 on a photoanode and creating a continuous compact layer of TiO_2. Figure 2.1b(i-ii) illustrates the innovative dimple compact TiO_2 layer and the suitability of Ag

nanowires as transparent electrodes in solar yarns. These solutions address various problems, as described by Lee et al. The dimple structure is crucial for bending robustness, preserving the fiber structure during annealing, and depositing additional mesoporous-TiO_2. Furthermore, solution process engineering can be easily used to create Ag nanowires. The solution-processed solar yarn demonstrated a power conversion efficiency of 3.85%.[40]

To increase flexibility and bending stability, Li et al.[6] developed a double-twisted solar yarn based on carbon fiber. This involved coating two layers of TiO_2 onto twisted carbon nanotubes - a compact layer for electron transport and a mesoporous layer for support. A composite combination of P3HT and single-walled carbon nanotubes served as the hole transport layer, and silver nanowires were placed on top for enhanced charge transmission. The Ag-coated yarn and CNT-yarn outer electrode were twisted together to form the double-twisted structure, which was then enclosed with PMMA for protection. The solar yarn achieved a champion PCE of 3.03%and maintained 89% of its PCE even after 96 hours in ambient conditions.[6]

In 2015, Deng et al.[41] described an elastic perovskite solar yarn constructed using aligned TiO_2 nanoparticles. A spring-like titanium wire was submerged in a titanium di-isopropoxide bis(acetylacetonate) solution, treated in a $TiCl_4$ solution, sintered at high temperature, and coated with TiO_2 nanoparticles. The titanium wire was then dipped in a perovskite solution, annealed to create a uniform perovskite layer, and dipped in a Spiro-OMeTAD solution to create a uniform HTL layer. An elastic silicone conductive yarn was added to provide the desired elasticity. The front electrode was formed by winding a second CNT sheet around the exterior surface. The device's efficiency significantly dropped from 5.22% to 0.6% when the outermost CNT sheets were removed. In order to improve the performance of perovskite solar yarn, Hu et al. developed a version with a titanium wire core electrode and mixed-halide perovskite (Figure 2.1(e)). The wire was heated and coated with a compact TiO_2 layer by dipping it in a TiO_2 solution and exposing it to air. A mesoporous layer was created by immersing the compact layer in a TiO2 colloidal solution. SEM analysis (Figure 2.1 e(i)) confirmed the device architecture, which involved coating a mixed halide perovskite layer ($CH_3NH_3PbI_{3-x}Cl_x$) and a Spiro-OMeTAD hole conductive layer using a solution processing technique. A flexible gold wire was wound around the fiber as the lead electrode, and an outermost gold back contact was added through magnetron sputtering (Figure 2.1 e(ii)). The optimized device achieved a short circuit current density of

12.32 mA/cm^2, a fill factor of 60.9%, a power conversion efficiency of 5.35%, and an open-circuit voltage of 0.714 V.[41]

The promising power conversion efficiency (PCE) of the material in planar devices led to further research on fiber-shaped perovskite solar cells. In 2016, Qui et al.[5] reported a solar yarn with a PCE of 7.1%. They grew TiO_2 nanorods (Figure 2.1f ii(a-b)) on a titanium wire, which served as the core and anode electrode, using anodization. This created a mesoporous structure. PbO porous scaffolds were then coated over the TiO2 nanotubes, and hydroiodic acid was added to generate PbI_2 crystalline plates (shown in Figure 2.1f ii(c-d)). The structure was dip-coated with CH_3NH_3I to form $CH_3NH_3PbI_3$ grains, which partially infiltrated the mesoporous TiO_2 through cathodic deposition. The entire structure was wrapped with transparent CNT, which had 80% transmittance in the 400–800 nm spectral range and an electrical conductivity of 500 S.cm^{-1}. This CNT layer served as the outer electrode for electron collection (Figure 2.1f). The fiber-shaped coaxially aligned PSC achieved a champion PCE of 6.8%, with an open-circuit voltage of 0.852 V and a short-circuit current density of 16.1 mA.cm^2. When a 5 nm silver coat was added to the outer layer (CNT), the contact electrode's conductivity improved from 1000 Scm^{-1} to 7.1%. It also had a fill factor of 56% and a short-circuit current density of 14.5 mA/cm^2.[5]

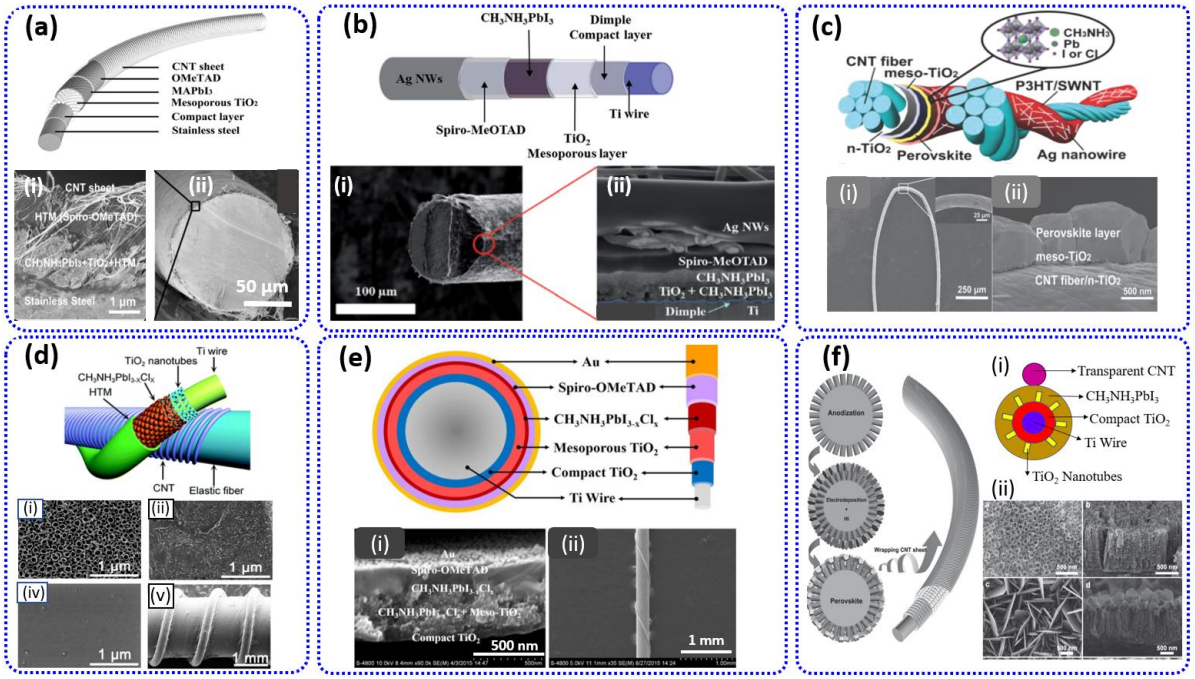

Figure 2.1 a) Steel core pioneer fiber solar cell. i-ii) SEM images show the arrangement of various layers and the yarn cross-section, respectively.[39] b) Schematic of an Ag nano wall-based perovskite yarn as the transparent top electrode with; i & ii) cross-section and surface SEM images show various layers' arrangement within the solar yarn.[40] c) A schematic of a highly flexible and double twisted perovskite yarn based on double twisted carbon nanofibers. i-ii) The SEM images show the bent solar yarn and the arrangement of various layers, respectively.[6] d) Schematic layer structure and surface SEM images of a highly elastic perovskite solar yarn suggested by Li et al. (i) Top view of aligned TiO_2 nanotubes, ii) Top view of $CH_3NH_3PbI_{3-x}Cl_x$, iii) Top view of the hole transport layer, iv) An elastic perovskite solar fiber solar cell with a pitch distance of 1.25 mm.[41] e) Schematic layer structure, cross-section, and surface SEM images of a fiber-shaped perovskite solar yarn suggested by Hu et al.[42] f) Schematic layer structure of the solar yarn introduced by Qui et al. i) yarn cross-section, and SEM images of TiO_2 nanotube array by top and side views, respectively. c, d) PbI_2 nanoplate array by top and side views, respectively.[5]

Hu et al.[4] introduced lead acetate as a new precursor material for perovskite solar fibers. The purpose was to improve the formation of the perovskite lattice on curved surfaces. The method involved using a titanium wire as the core electrode. First, a compact and mesoporous TiO_2 layer was grown on the wire through dip coating and electrical heating. Then, the wire was submerged in a perovskite solution prepared according to equations 2.1 and 2.2. To deposit the photoactive layer, the wire was heated at 100°C in a nitrogen environment. The resulting fiber was dipped in a Spiro-OMeTAD precursor solution to create the hole-transport layer. Finally, a gold front electrode was applied using magnetron sputtering, resulting in the final device shown in Figure 2.2(a). Under AM 1.5 illumination, the solar device achieved a power conversion efficiency (PCE) of 7.53% and an open-circuit voltage of 0.96 V.[4]

$$Pb(CH_3COO)_2 + CH_3NH_3I + DMF \rightarrow (CH_3NH_3I)_x\text{–}PbI_2\text{–}(DMF)_y + CH_3NH_2\uparrow + DMF\uparrow + CH_3COOH\uparrow \quad \text{…Eqn..2.1}$$

$$(CH_3NH_3I)_x\text{–}PbI_2\text{–}(DMF)_y \rightarrow CH_3NH_3PbI_3 + DMF\uparrow + CH_3NH_3I\uparrow \quad \text{…….Eqn…2.2}$$

Previous studies have shown that dip-coated perovskite film layers on fiber-shaped solar cells have subpar coverage, crystal quality, and carrier transport performance. In an effort to enhance the efficiency of these solar cells, Dong et al.[43] introduced a vapor-assisted deposition method to create a high-quality perovskite film on a cylindrical substrate. Figure 2.2 (c) illustrates the assembly of the device on a titanium metal wire. The following layers were sequentially deposited: a TiO_2 compact layer, a TiO_2 mesoporous layer, a perovskite layer, a Spiro-OMeTAD

layer, and a thin gold film, from the inside to the outside. The titanium wire was electrically heated to 500°C to generate a dense TiO_2 layer on the surface, serving as the electron transport layer during the preparation process. To obtain the mesoporous TiO_2 layer, the titanium wire was repeatedly dipped into a TiO_2 nanoparticle colloid with electric heating at 100°C, and then annealed at 500°C. The photoactive layer was deposited in two steps. Firstly, PbI_2 was horizontally coated at room temperature, followed by a solid-gas reaction with CH_3NH_3I that took 4 hours to complete and produce high-quality perovskite crystals. Thermal annealing was performed to efficiently remove the residual CH_3NH_3I. The resulting perovskite crystals were large with minimal grain boundaries, enhancing charge carrier mobility. A Spiro-OMeTAD hole transport layer was subsequently deposited, followed by a thin gold electrode layer. The optimized device demonstrated a power conversion efficiency of 10.79%, with an open-circuit voltage of 0.95 V, a short-circuit current of 15.14 mA cm^{-2}, and a fill factor of 0.75. Due to the highly crystalline nature of perovskite photoactive films used in early solar yarn projects, these devices were prone to cracking when bent, stretched, or twisted, which limited their flexibility and resulted in reduced efficiency, shorter lifetimes, and limited applications.[43] Li et al. proposed a solution to this problem by using $CH_3NH_3PbI_3$-PVP composite nanofibers as the photoactive layer in a perovskite fiber solar cell. The cell was assembled on a flexible silver yarn, which acted as both the core support and negative electrode. The yarn was dip-coated with a uniform layer of the hole-selective material Poly(3-hexylthiophene-2,5-diyl) (P3HT), and then a homogeneous layer of perovskite-PVP photoactive nanofibers was electrospun around it at an ideal electrospinning voltage of 18 kV and relative humidity of 75%. The perovskite yarn was twisted together with a carbon fiber yarn coated with a PCBM-SnO_2 composite to form a complete device. This device achieved a maximum power conversion efficiency (PCE) of 15.7% and maintained 99% of its original PCE after 750 cycles of bending. Furthermore, the service lifetime of the solar device was extended to over 216 hours by coating the solar yarn with PMMA polymer.[44]

Despite the progress made in fiber-shaped perovskite solar cells, the presence of toxic Lead (Pb) limits their use in wearable and textile industries. Balilonda et al.[45] have developed a Lead-free perovskite solar yarn as a promising solution. They achieved this by integrating composite nanofibers of methylammonium tin mixed halide-Polyvinylpyrrolidone (PVP) doped with (6,6)-

Phenyl C_{61} butyric acid methyl ester ($PC_{61}BM$) into the yarn architecture. These composite lead-free perovskite nanofibers acted as the photoactive layer in the solar yarn. The yarn was assembled on a pristine cathode, with the carbon yarn dip-coated in P3HT (HTM) to create a Carbon-P3HT yarn. Then, the $CH_3NH_3PbI_{3-x}Clx$-C_{61}-PVP composite nanofibers were directly electrospun onto it at an electrospinning voltage of 18 kV for 3 minutes under a relative humidity of 75%. Finally, the trio-stacked yarn was twisted with a pure silver yarn to complete the solar yarn device. The photoactive nanofiber layer of the solar yarn had an optical bandgap of 1.65 eV and demonstrated strong light absorption capabilities in the wavelength range of 300-550 nm. The best lead-free solar yarn achieved an open-circuit voltage (Voc) of 1.52 V, a short-circuit current (Jsc) of 4.75 $mA.cm^{-2}$, a fill-factor of 72.5%, and a maximum power conversion efficiency (PCE) of 7.49% with a PCBM doping level of 0.17%.

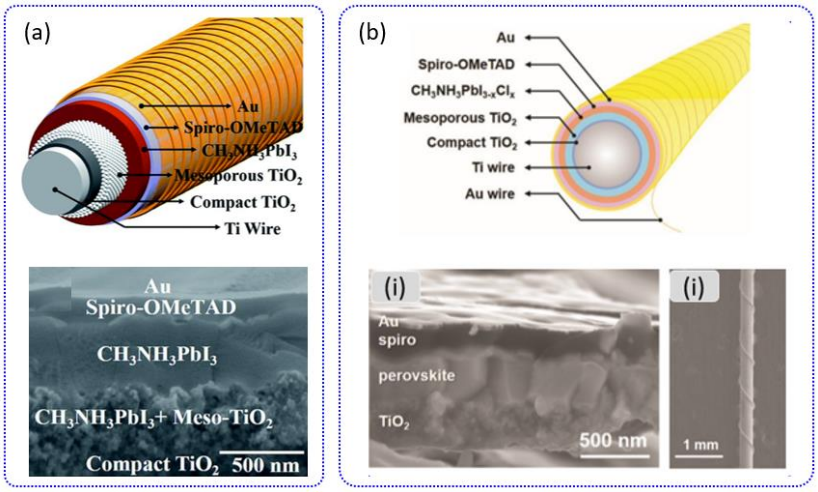

Figure 2.2 a) Schematic presentation and cross-sectional SEM image of the fiber-shaped perovskite solar cell based on the lead acetate precursor.[4] b) Schematic layer-by-layer structure of fiber-shaped perovskite solar cell assembled with vapor-assisted deposition; i) Cross-section SEM image showing the device layers; ii) Surface SEM image of a fiber-shaped perovskite solar cell.[43]

2.4.2 Rectangular cross-section fiber-type perovskite solar cells

Previous studies have highlighted two main challenges in the field of perovskite photoactive layers: achieving high quality and maximizing light exposure on curved or cylindrical surfaces.

Qiu et al.[46] addressed these challenges by developing a technique to enhance the quality of perovskite layers. They achieved this by growing high quality perovskite crystals on flexible strips made of polyethylene naphthalate coated with indium tin oxide. By adjusting the concentration of CH_3NH_3I, they were able to optimize the quality of the perovskite layer.

The flexible strip-shaped substrate acted as a transparent electrode, with light being emitted from this side. The flat surface of the strip enabled more uniform coverage of perovskite crystals and reduced defects in the photoactive layer. The SEM image in Figure 2.3(i) demonstrates the improved uniformity achieved with this technique. The perovskite crystals were grown in the micrometer size range on the flat surface of the substrate, which was consistently and evenly coated with the material. To further enhance device performance, a continuous carbon nanotube (CNT) sheet was added on top of the perovskite layer. This layer provided flexibility, mechanical strength, and electrical conductivity. A device measuring 1 x 5 mm² exhibited a power conversion efficiency (PCE) of 9.49%. Notably, even after being subjected to 500 cycles of bending and twisting with a curvature radius of 7.5 mm, the device maintained 90-93% of its original PCE, as depicted in Figure 2.3(ii).[46]

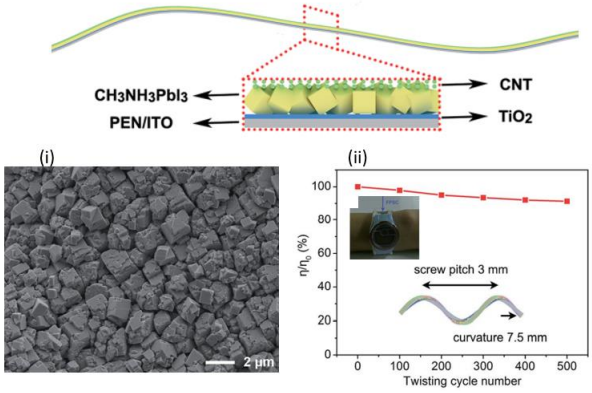

Figure 2.3 Schematic layer structure of the rectangular cross-section perovskite solar yarn with i) SEM image of the perovskite layer and ii) A graph presenting the variation of energy conversion efficiency with the number of twisting cycles. Inset is a photograph of an electric watch powered by the fiber-shaped perovskite solar cell. Images reprinted from reference.[46]

Table 2.2 A summary of the photovoltaic performance, photoactive material configuration, and the corresponding figures of the already reported fiber-shaped perovskite solar devices.

Perovskite Material configuration (photovoltaic layer)	Fill factor (%)	Short circuit current density (Jsc, mA cm^{-2})	Open circuit voltage (V)	PCE (%)	Reference
$CH_3NH_3PbI_3$	48.7	10.2	0.667	3.3	[39]
$CH_3NH_3PbI_3$	44.0	11.97	0.731	3.85	[40]
$CH_3NH_3PbI_x\ Cl_{3-x}$	56.4	8.75	0.615	3.03	[6]
$CH_3NH_3PbI_x\ Cl_{3-x}$		3.50	0.630	5.22	[41]
$CH_3NH_3PbI_x\ Cl_{3-x}$	60.9	12.32	0.714	5.35	[42]
$CH_3NH_3PbI_3$	56.0	14.20	0.85	7.1	[5]
$CH_3NH_3PbI_3$	66.0	14.18	0.96	7.53	[4]
$CH_3NH_3PbI_3$	0.656	15.9	0.91	9.49	[46]
$CH_3NH_3PbI_3$	0.75	15.14	0.95	10.79	[43]
$CH_3NH_3PbI_{3-x}Cl_x$-C_{61}-PVP	72.5	4.75	1.52	7.49	[45]
$CH_3NH_3PbI_3$–PVP	54.2	11.94	1.92	15.7	[44]

2.5 Challenges facing fiber-shaped perovskite solar cells

The fiber-shaped perovskite solar cells face several important challenges. These challenges include chemical and bending degradation, the need for high annealing temperatures, low fill factor, material toxicity, limited surface area for exposure to light from a single direction, lack of flexibility, and low power conversion efficiency (PCE). In the following paragraphs, each of these factors will be discussed in detail.

2.5.1 Perovskite material degradation

In order to industrialize and mass produce fiber perovskite solar cells, we need to address the issue of degradation observed in conventional thin film perovskite devices. The main triggers for degradation in these solar cells are environmental factors such as humidity, temperature, air, and UV radiation. Literature suggests that the commonly studied semiconductor perovskite, $CH_3NH_3PbI_3$, starts to decompose at a relative humidity of 55%. This degradation is visually noticeable as a distinct color change from dark brown to yellow[47]. In general, the degradation

and formation of methyl ammonium lead halide perovskites can be explained using the chemical equation 2.3 below.

$$PbI_2 + CH_3NH_3I_{(aq)} \leftrightarrow CH_3NH_3PbI_{3\,(s)} \quad \ldots..\text{Eqn } 2.3^{[48]}$$

The formation of $CH_3NH_3PbI_3$ occurs through a reaction between PbI_2 and CH_3NH_3I. This reaction can proceed from left to right or vice versa. Regardless of the geometry, there are two proposed degradation pathways for $CH_3NH_3PbI_3$.[48]

The first mechanism suggests that PbI_2 and CH_3NH_3I can combine with peripheral molecules, such as water, leading to the breakdown of $CH_3NH_3PbI_3$.

The second model explains that the degradation products of the perovskite depend on the prevailing conditions. In the presence of moisture, degradation occurs due to the solubility of methylammonium halide in water. When there are trace amounts of water, $CH_3NH_3PbX_3$ partially degrades to form an intermediate compound, which later decomposes into HI, CH_3NH_2 gases, and PbI_2 (as shown in the reactions). If there is excess water in the system, complete degradation occurs by dissolving HI and CH_3NH_2, leaving PbI_2 as a bright yellow substance (as shown in Equations 2.5 and 2.6).[49]

All of these reactions are reversible, allowing CH_3NH_3I, HI, CH_3NH_2, and insoluble PbI2 to coexist in the system. If the system is well encapsulated and there is minimal loss of these by-products, they can recombine to reform $CH_3NH_3PbI_3$, thus maintaining the performance of the perovskite cell for an extended period of time (as shown in Equations 2.4, 2.5, and 2.6).[50]

$$CH_3NH_3I_{(aq)} \leftrightarrow CH_3NH_{2\,(aq)} + HI_{(aq)} \quad \ldots\ldots\text{Eqn } 2.4$$

Decomposition of HI can proceed by either oxidation or under the influence of UV radiations as shown below.

$$2HI_{(aq)} \leftrightarrow H_{2\,(g)} + I_{2\,(s)} \quad \ldots\ldots\ldots\text{Eqn } 2.5^{[50]}$$

$$4HI_{(aq)} + O_{2\,(g)} \leftrightarrow 2I_{2\,(s)} + 2H_2O_{\,(l)} \quad \ldots\ldots..\text{Eqn } 2.6^{[50]}$$

In addition to the reversible reactions mentioned before, there are irreversible degradation reactions that can happen in perovskite materials due to moisture, UV, and temperature at the typical operating temperatures of solar cells, which range from 40 to 80°C. This is explained by reaction equation 2.7. Consequently, even if the perovskite solar cell is enclosed in a polymer, there may still be a small decrease in efficiency.[51]

$$CH_3NH_3PbI_{(aq)} \rightarrow NH_{3\,(aq)} + CH_3I_{(aq)} + PbI_{2\,(s)} \quad \ldots\ldots\ldots \text{Eqn } 2.7\ [51]$$

To stabilize perovskites, researchers have employed standard sealant approaches like encapsulation under inert conditions. These methods have been successful in preventing device degradation caused by moisture and oxygen.[52] Sealing or encapsulating the perovskite solar cell not only shields it from exposure to humid air, but also prevents the leakage and evaporation of volatile products that result from perovskite degradation. This allows the products to remain available to react and reform the perovskite within the system. According to Li et al.,[53] their fiber device experienced a 92% loss in power conversion efficiency (PCE) over a period of 96 hours in an open, humid environment when not encapsulated. However, when the device was coated with PMMA, its PCE was able to maintain 89% after 96 hours, as shown in Figure 2.4(a).

Other techniques for enhancing the stability of perovskite solar cells include the use of carbon protective (hydrophobic) layers, chemically inert scaffolds, and electrodes.[54] Additionally, mixed hybrid perovskites have been shown to improve both the stability and performance of solar cells. Seok and his colleagues reported that $CH_3NH_3Pb(I_{1-x}Br_x)$ (where $x > 0.2$) demonstrated good stability when exposed to 55% relative humidity for 20 days. The researchers attributed this stability to the compact and stable structure that resulted from the partial replacement of iodine with smaller bromine atoms in $CH_3NH_3Pb(I_{1-x}Br_x)$, which led to a reduction in lattice constant and a transition to the cubic phase.[55]

Another approach to enhancing stability is the use of an insulating mesoporous layer composed of Al_2O_3 nanoparticles. This layer prevents metal electrode migration, allows for precise control of the thickness of the hole transport material (HTM), and prevents degradation of the solar cell during 350 hours of operation.[56] It has also been reported that TiO_2 doped with Al_2O_3 is an effective perovskite scaffold for preventing rapid degradation. However, using Al_2O_3 alone as a

scaffold can accelerate degradation due to the formation of covalent bonds between alumina and the perovskite, resulting in a high binding energy. This leads to distortion at the Al_2O_3-perovskite interface and ultimately the dissociation of perovskite molecules.[57]

Two-dimensional hybrid perovskites, such as $(C_6H_5(CH_2)_2NH_3)_2MA(Pb_3I_{10})$ (where MA = CH_3NH_3), and other variants like 2D/3D $(HOOC(CH_2)_4NH_3)_2PbI_4/CH_3NH_3PbI_3$ perovskite junctions, have been shown to significantly extend the lifetime of perovskite solar cells. These 2D/3D hybrid perovskites have maintained their efficiency for up to a record time of 1 year under normal operating conditions.[58] This prolonged lifetime is attributed to their stable crystalline structure compared to mono-halide counterparts. Another strategy to overcome degradation caused by UV light is the use of an Sb_2S_3 interlayer between the mesoporous titanium layer and the photoactive $CH_3NH_3PbI_3$. Additionally, the use of UV filters, such as europium-doped yttrium vanadate, has been shown to prolong the active lifetime of the perovskite cell, although these rare earth materials are costly.[59] When it comes to fiber PV cells, the core material (metal or metal oxide, doped polymer, or any other conducting material) is coated with different layers in a specific order. However, flexing the core material and the fiber in general can cause stress that damages the compact TiO_2 layer and weakens various interfaces, leading to degradation and eventual cell failure.[60] To address this issue, it is recommended to use more bending-resistant layers to replace the traditional layers that are prone to cracking.

2.5.2 High annealing temperatures involved

A careful analysis of the annealing process reveals that highly efficient n-type compact TiO_2 layers can be produced at high annealing temperatures. According to Kais et al., TiO_2 doped with Fe^{3+} exhibits superior photocurrent generation properties compared to undoped material.[61] The presence of Fe^{3+} ions in TiO_2 facilitates the effective separation of hole-electron pairs, thereby enhancing the photocurrent generation capacity of the perovskite cell. However, annealing at elevated temperatures leads to increased production of iron oxide in the Fe^{3+}-TiO_2 system.[5] This significantly impacts electron transport and results in lower power conversion efficiency. The use of high annealing temperatures also escalates the production costs of PV fibers and renders the design process nearly impossible, making them less competitive in the market.

Furthermore, the integration of perovskites using simple conventional alternatives is limited by the high-temperature annealing of n-TiO_2 at 450–500°C.[62] Additionally, if conventional annealing methods are used, the annealed TiO_2 layer on highly curved surfaces, such as fiber PV, tends to peel off, leading to surface defects.[63] To overcome the issue of crack formation and propagation associated with annealing metal-oxides, especially in fiber-based devices, we propose replacing it in these PV devices with polymers that have high electron affinities, such as poly(p-phenylene vinylene) (PPV).[64] Another suitable option for electron transport materials in this application could be (6,6)-phenyl C_{61}-butyric acid methyl ester (PCBM). Moreover, it would be appropriate to replace other layers of these PV fibers with bending-resistant and low-temperature processable materials like poly(3,4-ethylenedioxythiophene):poly(styrene sulfonate) (PEDOT:PSS).[65] However, these alternative replacements face various challenges. Firstly, the semi-conductive polymers are electrically resistive and chemically vulnerable. To the best of our knowledge, they have not yet been incorporated into fiber devices. This issue may have arisen due to process difficulties and the subpar performance of semi-conductive polymers. Additionally, the majority of low-temperature (room-temperature) annealing techniques that have been uncovered are not technically suitable for fiber-shaped cells.[66]

2.5.3 Low fill factor and low power conversion efficiency

The fill factor values of previously reported fiber perovskite solar cells are generally low, with the highest reported value being 60.9%. This is due to structural defects, which can be either intrinsic (such as lattice imperfections in each layer) or extrinsic (such as lack of interfacial contacts). The former is a result of uneven co-axial growth of the layers, which is difficult to control. The latter is mainly caused by poor interlayer contacts, especially between twisted yarns, and can also result from layer breaking, peeling off, and segregation during measurement or device operation.[42]

The fill factor (FF) is defined by Equation 2.3, where J_m and V_m represent the current density and voltage at maximum output power, respectively. Jsc and Voc indicate the short circuit current (maximum current when the voltage is zero) and open circuit voltage (maximum voltage when the current density is zero), respectively.

$$FF = \frac{J_m V_m}{J_{sc} V_{oc}} \ldots\ldots\ldots\ldots\ldots\ldots\ldots\ldots\ldots\ldots\ldots\ldots\ldots\ldots \text{Eqn } 2.3^{[67]}$$

The expression suggests that the fill factor can be limited by a low overall current density and resulting voltage, which are greatly affected by the molecular and bulk structure of layers and interfaces. This becomes an even bigger problem for fiber solar cells, including fiber PSCs, because the active surface area decreases from the outermost to the core due to co-axial stacking. As shown in the inset of Figure 2.4b, this alignment leads to charge accumulation in the junctions. In other words, the fiber architecture potentially results in higher trap densities and recombination rates compared to the flat (thin film) architecture. This phenomenon creates even more complications for PSC fibers, which typically consist of at least five layers. For a high-quality solar cell, the fill factor is expected to be between 0.7 and 0.8, while a poorly performing cell may have a fill factor of 0.4 or even lower.[67] For perovskite fiber solar cells, the fill factor ranges from 0.48 to 0.66. It appears that this issue can be partially controlled by passivating trap sites at each individual junction through oxidation, assembly of an electrically active mono-layer, and doping with monovalent ions (Li^+, Cl^-).[68]

2.5.5 Limited surface area for unidirectional light exposure

The curved outward surface of fibers limits the access to photons when they are used as solar devices. Figure 2.4c compares the surface available for photons in flat and fiber solar cells. When the fibers are illuminated from one direction, a significant portion of the fiber system is always in the dark. As a result, the conversion efficiency of fiber PSCs is technically lower than expected. However, if fiber-shaped perovskite solar cells are illuminated from all angles, they can compete favorably with their planar counterparts in terms of efficiency. Theoretically, if the fiber solar cells are fully exposed to light, they should be able to produce a higher PCE compared to flat cells because of their larger surface area. However, in reality, this wide area is always partially illuminated. This may explain why there is a significant difference in reported efficiency between fiber-shaped and thin film solar cells, including PSCs. In addition to the functional problems caused by the reducing surface area, the accumulation of thermal energy in perovskite layers could be a key factor in cell degradation and low stability. To partially

overcome this issue, a modified highly absorptive perovskite compound must be developed specifically for fiber PSCs. Furthermore, a highly transparent front electrode and an anti-refractive layer (such as carbon allotropes) must be incorporated as the top layer.[69]

2.5.6 Loss of efficiency due bending and twisting

Wearable electronics often experience deformation, leading to cracks and fractures. These issues not only cause local malfunctions but also allow oxygen and water to permeate or trigger unwanted chemical reactions.[70] A key challenge in the field is to incorporate flexible and stress-sustaining materials in fiber solar cells. In particular, the functional layers of perovskite solar cells need to be ultrathin. However, these layers often develop numerous tiny defects during formation, which can enlarge and disrupt the device's efficiency when flexed. Figure 2.4(d) presents SEM images (layer and cross-section) and efficiency versus bending of a $NH_3CH_3PbI_{3-x}Cl_x$ fiber cell fabricated by Qiu's team.[39] This cell may owe its sturdiness to a stainless-steel support, a CNTs front contact, and a double (compact/mesoporous) TiO_2 ETL under perovskite. However, the manufacturing difficulty of forming mp-TiO_2 with a 400°C annealing process makes it incompatible for highly flexible supports such as conductive polymers. Li et al.[53] attempted to enhance bending stability by designing a perovskite fiber with a double twist. This fiber used CNT yarns for both the core support and the wrapping electrode. The ETL and HTL comprised a double (compact/mesoporous) TiO_2 and P3HT, covered by single-wall carbon nanotubes. This fiber configuration maintained its original performance even after 1000 cycles of bending. It was suggested that the SWCNTs filled in the initial cracks and controlled degradation due to bending. Deng et al.[41] grew $CH_3NH_3PbI_{3-x}Cl_x$ on a Ti-wire support between TiO_2 nanotubes or nanoparticles (ETL) and Spiro (HTL). The whole fiber was then twisted onto a super elastic fiber wrapped in CNT fibers. The efficiency of this fiber solar system was not significantly affected by bending, strain, or stretch, especially when TiO_2 nanoparticles were embedded as ETL. Figure 2.4(f) illustrates the mechanical endurance of this system.[41]

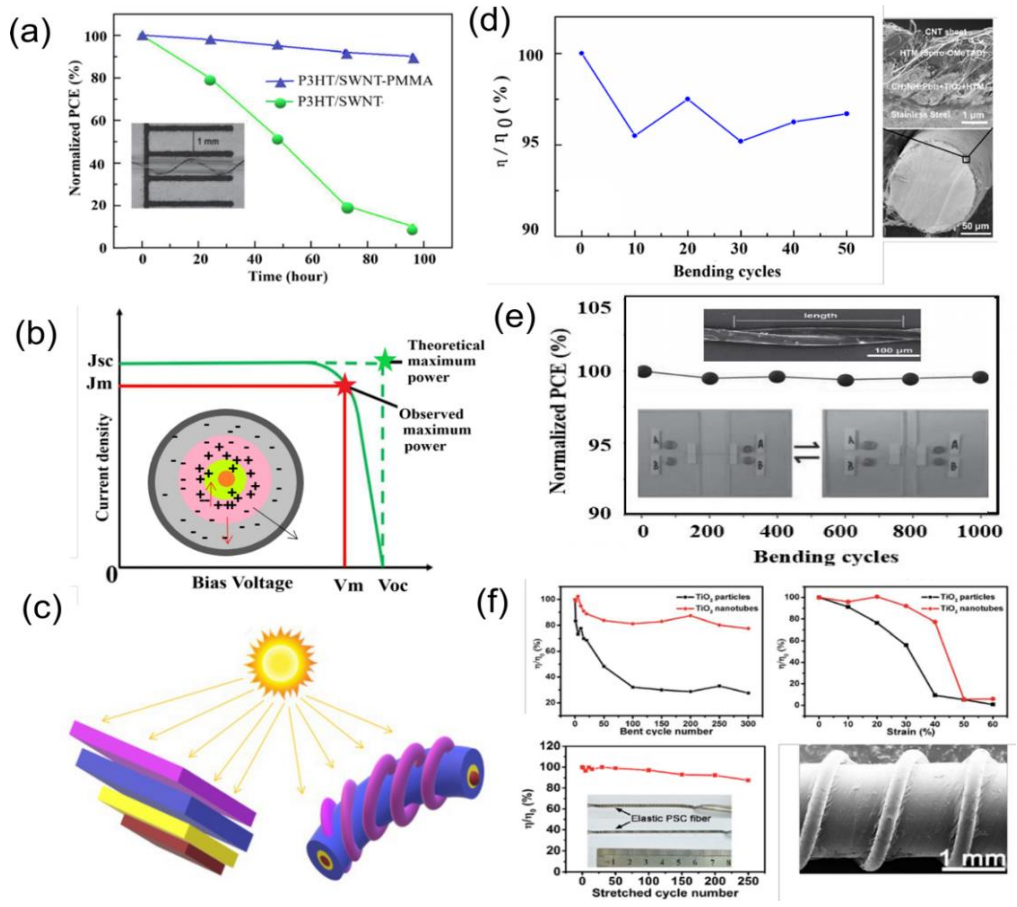

Figure. 2.4 (a) Stability test of double-twist fiber of $CH_3NH_3PbI_XCl_{3-X}$ encapsulated by PMMA for a period of 96 hrs (Inset photo of the device).[53] (b) Theoretical correlation between the voltage, current, and fill factor in a solar cell. Inset is an illustration of the imbalanced charge conduction due to the varying surface area from outermost to the core layer. (c) Different potential light exposure for the thin film and fiber SC. (d) SEM images (layer and cross-section) and efficiency versus bending of a $CH_3NH_3PbI_{3-x}Cl_x$ fiber SC with stainless steel support and CNTs front electrode.[39] (e) SEM image, efficiency versus bending, and the bending strategy of double-twist perovskite fiber SC, with CNTs yarn support and wrapping electrodes.[53] (f) Efficiency versus bending, strain and stretch, for $CH_3NH_3PbI_{3-x}Cl_x$ fiber SC, with Ti support, twisted onto a super elastic CNTs fiber.[41]

2.5.4 Toxicity

The photovoltaic community is well aware of the toxicity of key perovskite elements, such as Lead (Pb), as highlighted in Table 2.3 of the periodic table. This toxicity, along with the strain it puts on public perception and acceptance of perovskite devices, is a concern. The harmful effects of lead are attributed to its interactions with proteins, resulting in alterations in protein folding and decreased activity and function. Therefore, lead is toxic to all living organisms.[71] Tin (Sn) is being researched as a potential alternative for wearable and clothing-integrated solar cells. Although Sn is promoted as a more environmentally friendly alternative to Pb, it can still have negative impacts on the environment and human health.[72] Even though these metallic perovskite elements are used in small quantities in perovskite solar yarns, the potential for occupational and non-occupational exposure needs to be addressed due to the widespread use of this technology. The use of lead as the photoactive material in wearable perovskites is particularly risky because perovskites tend to disintegrate into harmful compounds when exposed to environmental conditions, leading to heavy metal contact with users of perovskite-based wearable devices.

When accidentally exposed to Pb-containing substances, lead can be absorbed through the digestive system, respiratory system, or skin.[73] Once absorbed, it can be transported by the blood to organs such as the liver, nervous system, and kidneys. The majority of lead (~90%) is deposited into the skeleton, where it remains for 20-30 years. Lead can cause significant damage as it can mimic essential elements like Ca, Fe, and Zn in the body, impairing the functionality of receptors and enzymes and interfering with the blood's hemoglobin activity.[74]

The use of Sn as a replacement for Pb in fiber-shaped perovskite solar cells is a newly emerging concept, and lead-free perovskite solar yarns have been reported.[45] However, due to the low redox potential of Sn(II), it quickly oxidizes to a more stable Sn(IV) under normal conditions. Therefore, Sn-based perovskites are typically synthesized in low-oxygen, dry environments in laboratories to slow down this conversion. Similar to Pb, Tin is absorbed and distributed through the body's transport systems, with a significant portion being deposited in the skeleton. Moreover, approximately 95% of ingested Sn is excreted in the feces quickly, with the remaining 5% being eliminated within 400 days.[75] The primary goal is to synthesize alternative materials

for perovskite that are both lead-free and environmentally friendly.[76] This involves replacing Pb^{2+} with less toxic cations that have similar outer shell electron configurations and ionic radii, such as Sn^{2+}, Ge^{2+}, Bi^{3+}, Sb^{3+}, and Sr^{+2}. Strontium is an option because its ionic radius is similar to lead and both metals have a valence state of +2. However, Sr is not preferred for photovoltaic purposes due to its high reactivity and narrow absorption range in the UV/Vis spectrum. Pb, Sn, and Ge have similar outer electron shell structures, but different ionic radii.[77] Among these choices, Sn has a high UV/Vis light absorption coefficient across a wide range of wavelengths.[78] Since the search for lead substitutes in perovskite began in 2014, Sn-based devices have consistently shown the highest PCE among all lead-free perovskite solar cells.

Table 2.3: A display of the periodic table, pointing out various elements used in photovoltaically useful perovskite materials configurations (ABX_3) and a glimpse of their level of toxicity.

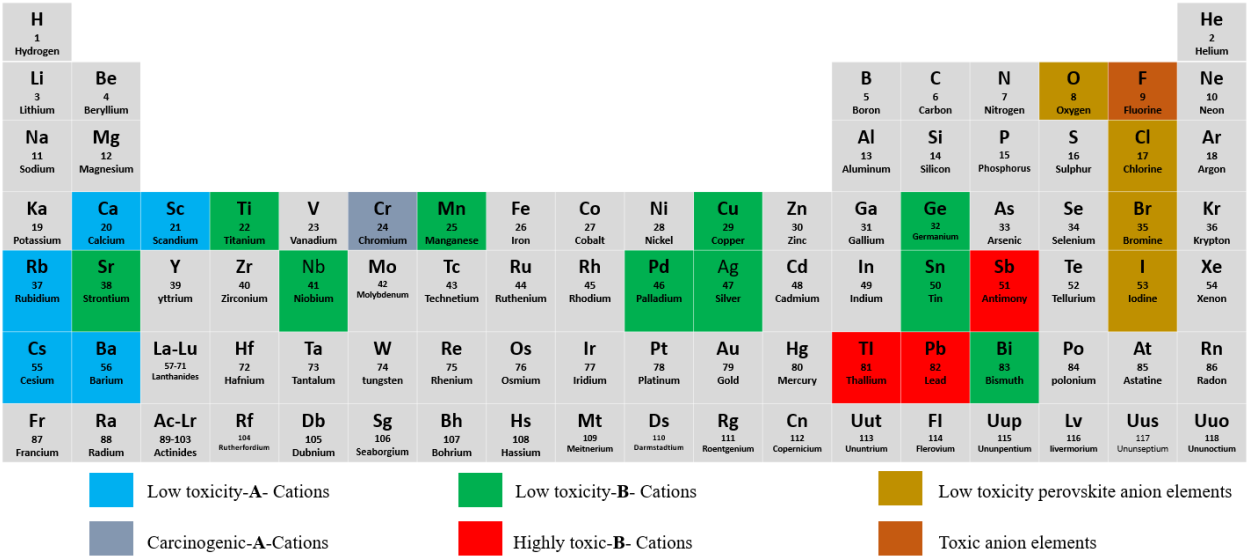

2.6 Conclusion

The realm of fiber-shaped perovskite solar cells is relatively new and remains a topic of great interest for numerous research teams. The efficiency of the PV capabilities in fiber-shaped perovskite solar cells is showing significant improvement, approaching levels seen in flat perovskite solar cells. Moreover, there is a growing focus on lead-free fiber-shaped perovskite solar cells, aiming to mitigate the potential toxicity hazards linked to perovskite PV systems that

predominantly consist of hazardous lead-based materials. Furthermore, in order for this technology to be scaled for industrial purposes, further investigation is essential to enhance the flexibility, durability, and lightweight nature of perovskite solar cells that can be woven. This is due to the numerous benefits and minimal preparatory steps required in creating woven structures. Consequently, there is a need for more cutting-edge engineering concepts to be implemented in various layers of these solar cells to ensure the achievement of the specified objectives.

2.7 Summary of potential areas for future research to address the current limitations

After reviewing the existing literature on perovskite materials and fiber-shaped perovskite solar cells, several potential research directions have emerged that could contribute significantly to the field. The following research avenues show promise for further exploration:

1. Overcoming perovskite material toxicity by replacing Pb with Sn in the material: Investigating the feasibility and potential advantages of replacing Pb with Sn in perovskite materials to reduce toxicity and improve overall material properties.
2. Synthesizing 2D3D hybrid perovskite to enhance material resistance to degradation: Exploring the synthesis of 2D3D hybrid perovskite structures to create materials with enhanced stability and resistance to degradation under various environmental conditions.
3. Devising better methods of perovskite layer deposition on curved substrates: Developing novel deposition techniques that can effectively deposit perovskite layers on curved substrates to enable the fabrication of flexible and curved solar devices.
4. Adopting nanofibers to enhance solar yarn flexibility: Investigating the use of nanofibers to improve the flexibility and mechanical properties of solar yarns, potentially enhancing their performance and applicability in various settings.
5. Using antioxidants to suppress tin oxidation: Exploring the use of antioxidants as a means to inhibit tin oxidation in perovskite materials, thereby improving the material's stability and longevity.

These potential research directions offer exciting opportunities for further investigation and innovation in the field of perovskite materials, with the potential to address critical challenges and drive advancements in solar energy technologies.

2.8 References

1. Balilonda, A., Z. Li, Y. Fu, F. Zabihi, et al., Perovskite fiber-shaped optoelectronic devices for wearable applications. J. Mater. Chem. C, 2022. **10**(18): 6957-6991.

2. Balilonda, A., Q. Li, M. Tebyetekerwa, R. Tusiime, et al., Perovskite solar fibers: current status, issues and challenges. Adv. Fiber Mater, 2019. **1**: 101-125.

3. Way, A., J. Luke, A.D. Evans, Z. Li, et al., Fluorine doped tin oxide as an alternative of indium tin oxide for bottom electrode of semi-transparent organic photovoltaic devices. AIP Adv, 2019. **9**(8): 085220.

4. Hu, H., B. Dong, B. Chen, X. Gao, et al., High performance fiber-shaped perovskite solar cells based on lead acetate precursor. Sustainable Energy & Fuels, 2018. **2**(1): 79-84.

5. Qiu, L., S. He, J. Yang, J. Deng, et al., Fiber-shaped perovskite solar cells with high power conversion efficiency. Small, 2016. **12**(18): 2419-2424.

6. Li, R., X. Xiang, X. Tong, J. Zou, et al., Wearable double-twisted fibrous perovskite solar cell. Adv. Mater, 2015. **27**(25): 3831-3835.

7. Wang, X., J. Wu, Y. Yang, X. Liu, et al., High performance and stable perovskite solar cells using vanadic oxide as a dopant for spiro-OMeTAD. J. Mater. Chem. A, 2019. **7**(21): 13256-13264.

8. Zhu, W., W. Chai, D. Chen, H. Xi, et al., Recycling of FTO/TiO2 substrates: route toward simultaneously high-performance and cost-efficient carbon-based, all-inorganic CsPbIBr2 solar cells. Acs Appl Mater Inter, 2020. **12**(4): 4549-4557.

9. Huang, Y., R. Jin, Z. Xiong, S. Wu, et al., Hexagonal-Tiled Indium Tin Oxide Electrodes To Enhance Light Trapping in Perovskite Solar Cells. ACS Applied Nano Materials, 2018. **1**(11): 6159-6167.

10. Wang, H., S. Cao, B. Yang, H. Li, et al., NH4Cl-modified ZnO for high-performance CsPbIBr2 perovskite solar cells via low-temperature process. Solar RRL, 2020. **4**(1): 1900363.

11. Ebrahimi, M., A. Kermanpur, M. Atapour, S. Adhami, et al., Performance enhancement of mesoscopic perovskite solar cells with GQDs-doped TiO2 electron transport layer. Sol. Energy Mater & Sol Cells, 2020. **208**: 110407.

12. Jiang, Q., X. Zhang, and J. You, SnO2: a wonderful electron transport layer for perovskite solar cells. Small, 2018. **14**(31): 1801154.

13. Yang, D., X. Zhang, K. Wang, C. Wu, et al., Stable efficiency exceeding 20.6% for inverted perovskite solar cells through polymer-optimized PCBM electron-transport layers. Nano letters, 2019. **19**(5): 3313-3320.

14. Raoui, Y., H. Ez-Zahraouy, N. Tahiri, O. El Bounagui, et al., Performance analysis of MAPbI3 based perovskite solar cells employing diverse charge selective contacts: Simulation study. Solar Energy, 2019. **193**: 948-955.

15. Wei, Q., W. Zi, Z. Yang, and D. Yang, Photoelectric performance and stability comparison of MAPbI3 and FAPbI3 perovskite solar cells. Solar Energy, 2018. **174**: 933-939.

16. Mehdi, H., A. Mhamdi, R. Hannachi, and A. Bouazizi, MAPbBr3 perovskite solar cells via a two-step deposition process. RSC Adv, 2019. **9**(23): 12906-12912.

17. Qiu, Z., N. Li, Z. Huang, Q. Chen, et al., Recent advances in improving phase stability of perovskite solar cells. Small Methods, 2020. **4**(5): 1900877.

18. Lee, J., M.M. Menamparambath, J.Y. Hwang, and S. Baik, Hierarchically structured hole transport layers of spiro-OMeTAD and multiwalled carbon nanotubes for perovskite solar cells. ChemSusChem, 2015. **8**(14): 2358-2362.

19. Jeon, N.J., H.G. Lee, Y.C. Kim, J. Seo, et al., o-Methoxy substituents in spiro-OMeTAD for efficient inorganic–organic hybrid perovskite solar cells. J. Am. Chem. Soc, 2014. **136**(22): 7837-7840.

20. Liu, J., Y. Wu, C. Qin, X. Yang, et al., A dopant-free hole-transporting material for efficient and stable perovskite solar cells. Energy & Environmental Science, 2014. **7**(9): 2963-2967.

21. Tsarev, S., S.Y. Luchkin, K.J. Stevenson, and P.A. Troshin, Perylenetetracarboxylic dianhydride as organic electron transport layer for nip perovskite solar cells. Synthetic Metals, 2020. **268**: 116497.

22. Reza, K.M., S. Mabrouk, and Q. Qiao, A review on tailoring PEDOT: PSS layer for improved performance of perovskite solar cells. Proc. Nat. Res. Soc, 2018. **2**(1): 02004.

23. Li, Z., B.H. Jo, S.J. Hwang, T.H. Kim, et al., Bifacial passivation of organic hole transport interlayer for NiOx-based p-i-n perovskite solar cells. Advanced Science, 2019. **6**(6): 1802163.

24. Jung, M., Y.C. Kim, N.J. Jeon, W.S. Yang, et al., Thermal stability of CuSCN hole conductor-based perovskite solar cells. ChemSusChem, 2016. **9**(18): 2592-2596.

25. Takahashi, K. and Y. Suzuki, Perovskite solar cells with CuI inorganic hole conductor. Japanese Journal of Applied Physics, 2017. **56**(8S2): 08MC04.

26. Liu, L., Q. Xi, G. Gao, W. Yang, et al., Cu2O particles mediated growth of perovskite for high efficient hole-transporting-layer free solar cells in ambient conditions. Sol. Energy Mater & Sol Cells, 2016. **157**: 937-942.

27. Wang, H., H. Liu, W. Li, L. Zhu, et al., Inorganic perovskite solar cells based on carbon electrodes. Nano Energy, 2020. **25**: 105160.

28. Kojima, A., K. Teshima, Y. Shirai, and T. Miyasaka, Organometal halide perovskites as visible-light sensitizers for photovoltaic cells. J. Am. Chem. Soc, 2009. **131**(17): 6050-6051.

29. Im, J.-H., C.-R. Lee, J.-W. Lee, S.-W. Park, et al., 6.5% efficient perovskite quantum-dot-sensitized solar cell. Nanoscale, 2011. **3**(10): 4088-4093.

30. Kim, H.-S., C.-R. Lee, J.-H. Im, K.-B. Lee, et al., Lead iodide perovskite sensitized all-solid-state submicron thin film mesoscopic solar cell with efficiency exceeding 9%. Sci. Rep, 2012. **2**(1): 1-7.

31. Zhang, W., M. Saliba, D.T. Moore, S.K. Pathak, et al., Ultrasmooth organic–inorganic perovskite thin-film formation and crystallization for efficient planar heterojunction solar cells. Nat. Commun, 2015. **6**(1): 1-10.

32. Zhou, H., Q. Chen, G. Li, S. Luo, et al., Interface engineering of highly efficient perovskite solar cells. Science, 2014. **345**(6196): 542-546.

33. Bi, D., C. Yi, J. Luo, J.-D. Décoppet, et al., Polymer-templated nucleation and crystal growth of perovskite films for solar cells with efficiency greater than 21%. Nat. Energy, 2016. **1**(10): 1-5.

34. Shin, S.S., E.J. Yeom, W.S. Yang, S. Hur, et al., Colloidally prepared La-doped BaSnO3 electrodes for efficient, photostable perovskite solar cells. Science, 2017. **356**(6334): 167-171.

35. Mostafaeipour, A., M. Alvandimanesh, F. Najafi, and A. Issakhov, Identifying challenges and barriers for development of solar energy by using fuzzy best-worst method: A case study. Energy, 2021. **226**: 120355.

36. You, J., Z. Hong, Y. Yang, Q. Chen, et al., Low-temperature solution-processed perovskite solar cells with high efficiency and flexibility. ACS Nano, 2014. **8**(2): 1674-1680.

37. Fu, X., H. Sun, S. Xie, J. Zhang, et al., A fiber-shaped solar cell showing a record power conversion efficiency of 10%. J. Mater. Chem. A, 2018. **6**(1): 45-51.

38. Wang, D., S. Hou, H. Wu, C. Zhang, et al., Fiber-shaped all-solid state dye sensitized solar cell with remarkably enhanced performance via substrate surface engineering and TiO2 film modification. Journal of Materials Chemistry, 2011. **21**(17): 6383-6388.

39. Qiu, L., J. Deng, X. Lu, Z. Yang, et al., Integrating perovskite solar cells into a flexible fiber. Angewandte Chemie International Edition, 2014. **53**(39): 10425-10428.

40. Lee, M., Y. Ko, and Y. Jun, Efficient fiber-shaped perovskite photovoltaics using silver nanowires as top electrode. J. Mater. Chem. A, 2015. **3**(38): 19310-19313.

41. Deng, J., L. Qiu, X. Lu, Z. Yang, et al., Elastic perovskite solar cells. Journal of Materials Chemistry A, 2015. **3**(42): 21070-21076.

42. Hu, H., K. Yan, M. Peng, X. Yu, et al., Fiber-shaped perovskite solar cells with 5.3% efficiency. Journal of Materials Chemistry A, 2016. **4**(10): 3901-3906.

43. Dong, B., J. Hu, X. Xiao, S. Tang, et al., High-Efficiency Fiber-Shaped Perovskite Solar Cell by Vapor-Assisted Deposition with a Record Efficiency of 10.79%. Adv. Mater. Technol, 2019. **4**(7): 1900131.

44. Li, Q., A. Balilonda, A. Ali, R. Jose, et al., Flexible Solar Yarns with 15.7% Power Conversion Efficiency, Based on Electrospun Perovskite Composite Nanofibers. Solar RRL, 2020. **4**(9): 2000269.

45. Balilonda, A., Q. Li, X. Bian, R. Jose, et al., Lead-free and electron transport layer-free perovskite yarns: Designed for knitted solar fabrics. J. Chem. Eng, 2021. **410**: 128384.

46. Qiu, L., S. He, J. Yang, F. Jin, et al., An all-solid-state fiber-type solar cell achieving 9.49% efficiency. J. Mater. Chem. A, 2016. **4**(26): 10105-10109.

47. Motti, S.G., D. Meggiolaro, A.J. Barker, E. Mosconi, et al., Controlling competing photochemical reactions stabilizes perovskite solar cells. Nat. Photonics., 2019. Available from: https://doi.org/10.1038/s41566-019-0435-1.

48. Niu, G., X. Guo, and L. Wang, Review of recent progress in chemical stability of perovskite solar cells. J. Mater. Chem. A, 2015. **3**(17): 8970-8980.

49. Shirayama, M., M. Kato, T. Miyadera, T. Sugita, et al., Degradation mechanism of CH3NH3PbI3 perovskite materials upon exposure to humid air. Int. J. Appl. Phys, 2016. **119**(11): 115501.

50. Matteocci, F., L. Cinà, E. Lamanna, S. Cacovich, et al., Encapsulation for long-term stability enhancement of perovskite solar cells. Nano Energy, 2016. **30**: 162-172.

51. Oo, T.T. and S. Debnath. Application of carbon nanotubes in perovskite solar cells: A review. in AIP Conference Proceedings. 2017. AIP Publishing.

52. Wang, D., M. Wright, N.K. Elumalai, and A. Uddin, Stability of perovskite solar cells. Solar Energy Materials and Solar Cells, 2016. **147**: 255-275.

53. Saidaminov, M.I., A.L. Abdelhady, B. Murali, E. Alarousu, et al., High-quality bulk hybrid perovskite single crystals within minutes by inverse temperature crystallization. Nat. Commun, 2015. **6**(1): 1-6.

54. Hambsch, M., Q. Lin, A. Armin, P.L. Burn, et al., Efficient, monolithic large area organohalide perovskite solar cells. Journal of Materials Chemistry A, 2016. **4**(36): 13830-13836.

55. Noh, J.H., S.H. Im, J.H. Heo, T.N. Mandal, et al., Chemical management for colorful, efficient, and stable inorganic–organic hybrid nanostructured solar cells. Nano letters, 2013. **13**(4): 1764-1769.

56. Guarnera, S., A. Abate, W. Zhang, J.M. Foster, et al., Improving the long-term stability of perovskite solar cells with a porous Al2O3 buffer layer. The journal of physical chemistry letters, 2015. **6**(3): 432-437.

57. Akbari, A., J. Hashemi, E. Mosconi, F. De Angelis, et al., First principles modelling of perovskite solar cells based on TiO 2 and Al 2 O 3: stability and interfacial electronic structure. Journal of Materials Chemistry A, 2017. **5**(5): 2339-2345.

58. Grancini, G., C. Roldán-Carmona, I. Zimmermann, E. Mosconi, et al., One-Year stable perovskite solar cells by 2D/3D interface engineering. Nature communications, 2017. **8**: 15684.

59. Wang, R., M. Mujahid, Y. Duan, Z.K. Wang, et al., A Review of Perovskites Solar Cell Stability. Advanced Functional Materials, 2019: 1808843.

60. Lee, M.M., J. Teuscher, T. Miyasaka, T.N. Murakami, et al., Efficient hybrid solar cells based on meso-superstructured organometal halide perovskites. Science, 2012. **338**(6107): 643-647.

61. Elghniji, K., A. Atyaoui, S. Livraghi, L. Bousselmi, et al., Synthesis and characterization of Fe3+ doped TiO2 nanoparticles and films and their performance for photocurrent response under UV illumination. Journal of Alloys and Compounds, 2012. **541**: 421-427.

62. Zabihi, F., M.-R. Ahmadian-Yazdi, and M. Eslamian, Fundamental study on the fabrication of inverted planar perovskite solar cells using two-step sequential substrate vibration-assisted spray coating (2S-SVASC). Nanoscale research letters, 2016. **11**(1): 71.

63. Yun, J.S., A. Ho-Baillie, S. Huang, S.H. Woo, et al., Benefit of grain boundaries in organic–inorganic halide planar perovskite solar cells. The journal of physical chemistry letters, 2015. **6**(5): 875-880.

64. Greenham, N., S. Moratti, D. Bradley, R. Friend, et al., Efficient light-emitting diodes based on polymers with high electron affinities. Nature, 1993. **365**(6447): 628.

65. Docampo, P., J.M. Ball, M. Darwich, G.E. Eperon, et al., Efficient organometal trihalide perovskite planar-heterojunction solar cells on flexible polymer substrates. Nature communications, 2013. **4**: 2761.

66. Eslamian, M. and F. Zabihi, Ultrasonic substrate vibration-assisted drop casting (SVADC) for the fabrication of photovoltaic solar cell arrays and thin-film devices. Nanoscale research letters, 2015. **10**(1): 462.

67. Chikate, B.V. and Y. Sadawarte, The factors affecting the performance of solar cell. International journal of computer applications, 2015. **1**(1): 0975-8887.

68. Giordano, F., A. Abate, J.P.C. Baena, M. Saliba, et al., Enhanced electronic properties in mesoporous TiO 2 via lithium doping for high-efficiency perovskite solar cells. Nature communications, 2016. **7**: 10379.

69. Farhadi, B., I. Marriam, S. Yang, H. Zhang, et al., Highly efficient photovoltaic energy storage hybrid system based on ultrathin carbon electrodes designed for a portable and flexible power source Journal of Power Sources, 2019. **422**: 196-207.

70. Sangid, M.D., H.J. Maier, and H. Sehitoglu, The role of grain boundaries on fatigue crack initiation–an energy approach. International Journal of Plasticity, 2011. **27**(5): 801-821.

71. Toscano, C.D. and T.R. Guilarte, Lead neurotoxicity: from exposure to molecular effects. Brain Research Reviews, 2005. **49**(3): 529-554.

72. Winship, K., Toxicity of tin and its compounds. Adverse drug reactions acute poisoning reviews, 1988. **7**(1): 19-38.

73. Florence, T., S. Lilley, and J. Stauber, Skin absorption of lead. The Lancet, 1988. **332**(8603): 157-158.

74. Virgolini, M.B. and M. Aschner, Molecular mechanisms of lead neurotoxicity. Advances in neurotoxicology, 2021. **5**: 159.

75. Ricciarelli, D., D. Meggiolaro, F. Ambrosio, and F. De Angelis, Instability of tin iodide perovskites: bulk p-doping versus surface tin oxidation. ACS Energy Letters, 2020. **5**(9): 2787-2795.

76. Babayigit, A., A. Ethirajan, M. Muller, and B. Conings, Toxicity of organometal halide perovskite solar cells. Nat. Mater, 2016. **15**(3): 247-251.

77. Zhang, H., W. Liu, R. Li, M. Zhang, et al., Lead-less mesoscopic perovskite solar cells with enhanced photovoltaic performance by strontium chloride substitution. Ceramics International, 2018. **44**(15): 18863-18870.

78. Zhu, H.L., Z. Liang, Z. Huo, W.K. Ng, et al., Low-Bandgap Methylammonium-Rubidium Cation Sn-Rich Perovskites for Efficient Ultraviolet–Visible–Near Infrared Photodetectors. Adv. Funct. Mater, 2018. **28**(16): 1706068.

Chapter 3: Chlorine-Rich Substitution Enabled 2D3D Hybrid Perovskites for High Efficiency and Stability in Sn-based Fiber-Shaped Perovskite Solar Cells.

3.1 Introduction

Organic-inorganic perovskite materials have emerged as leading contenders for next-generation solar cells. They are favored for their solution processability,[1] affordability,[2] recyclability, [3] superior absorption coefficient, and impressive photovoltaic properties. Over the past decade, research in this field has primarily focused on three-dimensional (3D) molecular structure perovskites. The molecular formula for these materials is abbreviated as ABX_3, where A represents a monovalent organic cation, B is a divalent inorganic (metal) cation, and X denotes a halogen anion. The most extensively studied 3D configurations include $CH_3NH_3PbI_3$, $CH_3NH_3PbI_{3-x}Cl_x$, and other variations.[4] Since its initial report in 2009, the power conversion efficiency (PCE) record of 3D perovskites has been steadily increasing, reaching 25.7% in 2021. The large and continuous quantum well of 3D structured perovskites contributes to their favorable photovoltaic properties, including a small optical bandgap, low electron-hole binding energies ranging between 10-50 meV, an increased charge carrier diffusion length (>1 μm), and a broad absorption range (300~850 nm).[5]

Despite the remarkable progress made in developing 3D materials, the lack of long-term stability and toxicity are still significant obstacles to overcome in order to commercialize perovskite solar cells. Addressing the issue of toxicity, researchers have explored replacing lead (Pb) in perovskite with various divalent cations like Sn, Ge,[6] or using trivalent materials such as Bi or Sb.[7] However, such substitutions often come at the cost of reduced energy conversion efficiency. Among the lead-free alternatives available, Sn-based compounds appear to be the most promising, as they are non-toxic. However, Sn is susceptible to oxidation in ambient conditions, leading to high background carrier concentrations in ASnI3 perovskites.[8] Full oxidation of the material causes it to disintegrate from a three-dimensional (ASnX3) structure to a zero-dimensional (0D) structure. Partial oxidation (p-doping) results in degenerately doped ASnI3 perovskite, which can cause short circuits in the devices (A2SnX6).[9] Recently, several methods have been developed to mitigate the rapid degradation of Sn-based perovskite solar

cells.[10] However, the current approaches only provide limited stability, typically lasting a few hours, with the best-case scenario achieving stability for 500 hours in the dark at a relative humidity of 20%.[11] Therefore, there is still a need to further enhance the stability of Sn-based solar cells.

3.1.1 Two-dimensional (2D) perovskite materials

Lower-dimensional layered perovskites, also known as 2D perovskites, are a recent and promising material for stabilizing perovskite solar cells.[12] The pioneer 2D perovskite materials used in solar devices belonged to the homologous series of $(CH_3(CH_2)_3NH_3)_2(CH_3NH_3)_{n-1}Pb_nI_{3n+1}$ and achieved stability in medium humidity for several months with reasonable power conversion efficiency (PCE).[12] For example, the current champion stability in 2D-based perovskite solar cells was reported to be over 2,250 hours, with a 60% retention of the original PCE of 12.5%.[13]

Generally, 2D perovskite molecules consist of large spacer cations and quantum wells.[14] The stability and optoelectronic properties of these molecules are determined by the two parts. For instance, 2D perovskites exhibit thermal robustness and resistance to moisture due to the large hydrophobic spacer cations ($CH_3(CH_2)_3NH_3^+$) that surround the quantum wells $(CH_3NH_3)_{n-1}Pb_nI_{3n+1})^{(n+1)-}$ and protect them from external ambient conditions.[15] Additionally, the organic part of the 2D perovskite molecule typically has a wider bandgap compared to its inorganic counterpart. This leads to the formation of multiple pseudo quantum wells, where the organic layers act as potential barriers and the inorganic layers act as potential wells.[16] Consequently, the molecular structure of 2D perovskite molecules justifies their large average optical bandgap of at least 2.5 eV.[17] This limits photon conversion to short-wavelength illumination and results in a higher exciton binding energy of 300 meV, which reduces the output photovoltage and lowers the PCE.

3.1.2 Hybrid perovskite materials (2D3D)

By combining 2D and 3D perovskites, it is possible to create a hybrid material that combines the excellent photovoltaic capabilities of 3D perovskites with the remarkable stability of 2D perovskite molecules. In a recent synthesis, aminovaleric lead iodide was used as the 2D component and methylammonium lead iodide was used as the 3D component to create a 2D3D perovskite material.[15] This synthesis resulted in a stable 2D3D lead-based perovskite solar cell with a power conversion efficiency (PCE) of 12.9% over the course of 1 year, demonstrating the robust nature of hybrid 2D3D perovskite molecules. It is reasonable to predict that this approach could also improve the stability of Sn-based perovskite solar cells.[18]

During the transformation from 2D to 2D3D, the 2D molecules absorb methylammonium ions (MA^+) into their quantum wells, causing the molecules to grow in a more 3-dimensional pattern and form 2D3D hybrid perovskite molecules.[19] Mixed dimensional perovskites have been used as photoactive layers in perovskite solar cells, with large phenylethylammonium and methylammonium cations combined to create a composition with a Ruddlesden-Popper structure.[20] Another synthesis procedure involved mixing methylammonium (MAI) and lead iodide (PbI_2) with DMF and DMSO solvents to form the 3D molecules, which were then decomposed and $CH_3NH_3^+$ ions were released. A layer of aminovaleric acid iodide (AVI) was deposited on top of the decomposed layer to introduce the 2D material component. The 2D and 3D double layered arrangement was heated to form the 2D3D material. The resulting 2D3D-based planar solar cell had an 18.0% PCE and retained 90% of its initial PCE after 32 days.[21] Other researchers also used a layer-by-layer approach via spin coating, but this method had drawbacks such as high-temperature heating and the use of multiple solvents for efficient charge transfer.[19] Additionally, this procedure was not suitable for depositing the 2D3D perovskite layer on complex substrates. Moreover, the proposed procedure made it difficult to control and ensure a complete reaction between 2D and 3D materials.

Chen et al.[22] proposed an alternative method to the layer-by-layer spin coating approach for the self-assembly of 2D3D crystals. They developed a single-solution approach using a mixture of MAI, PbI_2, and isobutyl ammine (iBA) dissolved in a combination of Dimethylformamide (DMF) and Dimethyl sulfoxide (DMSO) solvents. By heating the mixture, crystals were formed,

which were then redissolved to act as seeds for larger 2D3D crystal growth. It is believed that the dissolution of pre-synthesized perovskite in solvents leaves molecular perovskite seeds in solution, which facilitate homogeneous nucleation for film growth into the desired products.[23] However, this self-assembly and recrystallization method had its challenges. It was difficult to achieve a complete reaction between 2D and 3D reagents, and the reaction itself took more than 24 hours, making it time-consuming. Additionally, a mixture of multiple solvents (DMF and DMSO) was required to achieve a perpendicular crystal arrangement on the substrate.

This study presents a novel technique for synthesizing and controlling of the interaction between 2D and 3D molecules to produce high-quality 2D3D hybrid perovskite materials through chlorine doping. The method takes advantage of chlorine's ability to displace iodine from its ionic compounds in solution. This facilitates a reaction that accelerates the production of high-quality 2D3D perovskite materials. By increasing the chlorine doping ratio in the iodine-based mixture of 2D and 3D perovskites in solution, the effective reaction time was reduced to ~20 minutes at 100ºC. Additionally, this approach allows for the use of DMF as the sole solvent to achieve the desired perpendicular orientation of perovskite slabs with 50% chlorine doping and above. Furthermore, a chemical reaction mechanism is proposed in which chloride ions act as catalysts for creating 2D3D hybrid perovskites from iodine-based 2D and 3D perovskite molecules in solution. The resulting 2D3D perovskite material was integrated into a fiber-shaped perovskite solar cell, achieving an impressive PCE of 11.96% in Sn-based fiber-shaped perovskite solar cells. The solar yarn was hermetically sealed in a nylon casing and retained over 95.5% of its initial efficiency after a 6-month service life under ambient conditions.

3.2 Experimental section

3.2.1 Materials

Materials were obtained as follows: Methyl ammonium (CH_3NH_3I, Tokyo Chemical Industry $\geq$ 99.0 wt%), Tin Iodide (SnI_2, Shanghai Bojing Chemical Co, LTD > 99 wt%), Tin Chloride ($SnCl_2$, Shanghai Bojing Chemical Co, LTD > 99 wt%, N, N-Dimethylformamide (DMF; C_3H_7NO, Shanghai Lingfeng Chemical Co, LTD $\geq$ 99.9 wt%), Aminovaleric acid iodide ($HOOC(CH_2)_4NH_3I$, AVAI, Tokyo Chemical Industry Co, LTD $\geq$ 97 wt%),

3.2.2 Synthesis of 2D3D perovskite materials

Inspired by the concept of more reactive halogens (F^-> Cl^-> Br^-> I^-) displacing the less reactive ones from their ionic compounds in solution (chloride ions displace iodide ions), we first synthesized a solution containing a mixture of iodine-based 2D and 3D perovskite molecules. This was done by mixing methylammonium iodide (CH_3NH_3I, MAI), aminovaleric acid iodide ($HOOC(CH_2)_4NH_3I$, AVI), and tin iodide (SnI_2) in DMF solvent, following the procedure reported in reference.[18] The ratio of MAI to SnI_2 was kept at 1:1 for all samples, and AVI was added at a constant proportion of 3% of the total mixture. The reagents were mixed according to the proportions presented in Table S1 (Appendix), resulting in dark-brown solutions of iodine-based 2D and 3D mixture.

To further modify the mixture, $SnCl_2$ was added in various ratios with the previously added SnI_2. The mixtures of 2D and 3D in solution were then magnetically stirred and heated at 100°C for 5 minutes, as shown schematically in Figure 3.1(a). The ratio of SnI_2: $SnCl_2$ was varied as follows; 1:0, 3:1, 1:1, 2:1, and 1:3, corresponding to 0%, 25%, 33%, 50% and 75% halogen percentage of chlorine added. With addition of chlorine in the 2D and 3D mixture, the color of the solutions changed from dark brown to light brown and finally to light yellow (with the increasing proportion of $SnCl_2$ added), as shown in Figure 3.1(b). These color changes are attributed to the displacement of iodine from its typical brown perovskite compounds in solution to colorless iodide ions.

To analyze the effect of chlorine doping on Sn-based 2D3D perovskite crystal size and layer quality, the prepared solutions were spin-coated on glass substrates and heated at 50°C for 5 minutes, followed by an increase in heating temperature to 100°C for an additional 5 minutes. The initial heating step facilitated slow nucleation and grain clustering for a high-quality crystallization process. The final high-temperature heating phase aimed to achieve tertiary crystallization and drive off solvents.[24] As shown in Figure S1 (Appendix), the average crystal size and quality of the perovskite layer increased with the increasing chlorine doping percentage, with the best layer quality obtained at 50% halogen percentage of chlorine.

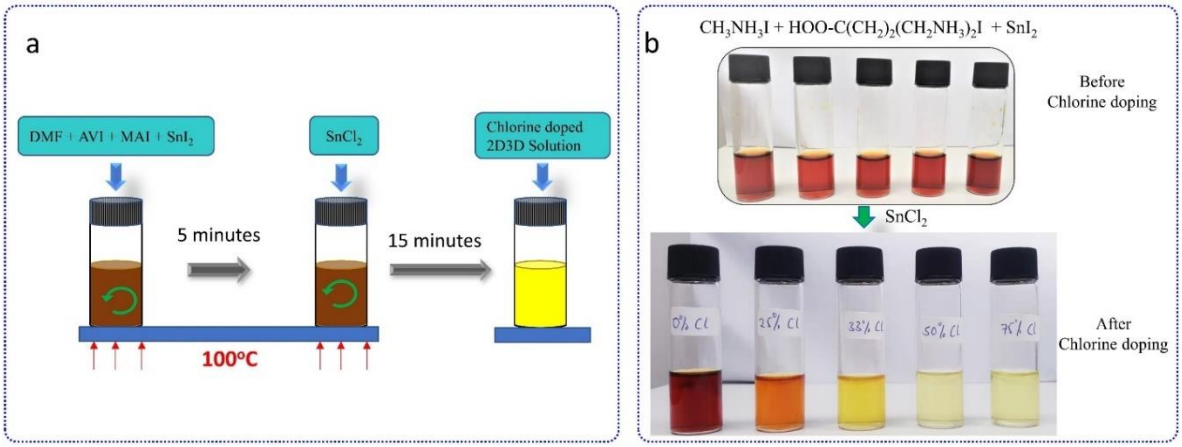

Figure 3.1. a) Schematic illustration of the chlorine-doped material synthesis route b) Camera images showing color changes with the increasing chlorine doping in iodine-based mixtures of 2D and 3D perovskites.

3.2.3 Characterization of 2D3D perovskite materials

As shown in Figure 3.2(a-b), the absorption spectra of chlorine-doped 2D3D synthesized samples exhibit two distinct regions with different characteristics. Figure 3.2(a) focuses on the 300∼500 nm wavelength range, also known as the 2D dominant region. This name comes from the observation that perovskite materials have higher absorbance in this range in the order of 2D > 2D3D > 3D. This indicates that perovskite materials with higher proportions of 2D exhibit the highest absorbance in this region (Figure S2, Appendix). However, increasing the chlorine doping percentage in the 2D3D perovskite material reduces the absorption capacity in the 300∼500 nm range and gradually increases the absorbance in the 550∼850 nm range, as shown in the magnified Figure 3.2(b).

The absorption capacity of perovskite materials in the 550∼850 nm range is in the order of 3D > 2D3D > 2D[18] (further supported by Fig. S2, Appendix). Therefore, the observed shift in the absorption behavior of the chlorine-doped samples from left to right of the absorption spectra indicates the rapid conversion of 2D to 2D3D hybrid molecules upon doping. In the 500∼850 nm region, the highest absorbance was recorded at a 50% halogen percentage of chlorine in the material (with a ratio of SnI_2:$SnCl_2$ = 1:1). These results can be attributed to an equal number of iodide and chloride ions in the solution, leading to effective displacement of iodide ions from

their ionic compounds and rapid transformation from 2D to 2D3D molecular structure, as explained in the mechanism in one of the subsections. With 75% chlorine doping, the excess and highly reactive chloride ions could have reacted with other molecules in the solution, resulting in traces of impurities that might have affected the absorbance of the 75% sample in the 550∼850 nm range. The above measurements were conducted using an ultraviolet–visible–infrared spectrophotometer (Perkin Elmer Instrument).

To further investigate the impact of chloride ions on the formation of 2D3D perovskite hybrid materials, we conducted steady-state and time-resolved photoluminescence (PL) measurements (see Figure 3.2(c-d)). Using a 478 nm pulse source, we excited charge carriers in chlorine-doped samples, as depicted in Figure 3.2(c). Notably, the undoped (0%) 2D3D sample exhibited the strongest emission, similar to that of a pure 2D sample ($HOOC(CH_2)_4NH_3)_2PbI_4$) illuminated with the same source.[18] These findings suggest a significant presence of the 2D phase in the undoped samples. In Figure 3.2(c), the intensity of excitons generated at 478 nm decreases with increasing chlorine doping, indicating a reduction in the amount of 2D material as it rapidly transforms into 2D3D due to chlorine doping. However, changing the excitation source wavelength to 665 nm reverses this trend, as shown in Figure 3.2(d). With a 665 nm laser beam, increasing the chlorine doping percentage leads to an increase in the intensity of excited charge carriers, with the highest intensity observed at 50%. These results offer additional evidence of the catalytic role of chloride ions in the reaction between 2D and 3D perovskites, resulting in the formation of 2D3D hybrid materials with altered bandgap, absorption peaks, and molecular dimensionality, among other properties. The photoluminescence measurements were performed using a lamp or a pulsed source with a spectrophotometer (Gilden Photonics).

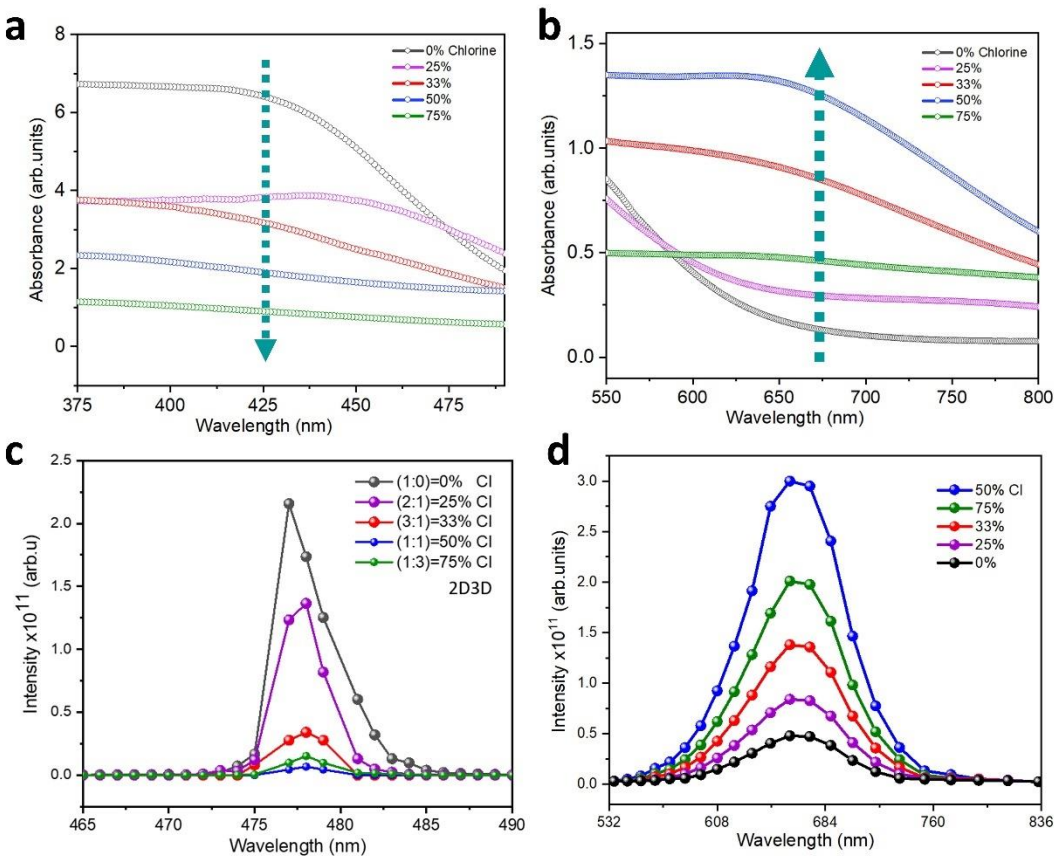

Figure 3.2 a) A magnified section of the absorption spectra in the wavelength range of 375-500 nm with increasing chlorine doping. c) A magnified section of the absorption spectra in the 500-800 nm range with increasing chlorine doping. c-d) Steady-state PL spectra with excitation wavelengths of 478 and 665 nm with increasing chlorine doping.

Figure 3.3(a) shows X-ray diffraction (XRD) patterns revealing a single Bragg peak at approximately 10° (2θ position), indicating a parallel orientation (060). The multiple reflections at low angles suggest the formation of a low-dimensional perovskite with a potentially complex crystal structure (2θ < 10°).[25] As chlorine doping increases in the 2D3D materials, the intensity of the 2D peak at (060) decreases and disappears completely at 50% chlorine doping and beyond. Despite the reduction in intensity, the position of the peak remains constant at 2θ ≈ 10°, indicating that the 2D molecules used in the chemical reaction were uniform and consisted of Sn_3I_{10} (n = 3). However, a slight addition of chlorine (from 0 to 25%) leads to changes in the lattice measurements of the crystals, as evidenced by the shift of the (120) peak from 19.5° to 20.0°. This increase in crystal dimensions is attributed to the larger molecular size resulting from

the transformation from 2D to 2D3D molecules with a large quantum well, hence the reduction in the intensity of the 2D peak.

We synthesized high-purity 2D3D hybrid Sn-based perovskite material with high-quality grains and a preferred perpendicular orientation of the perovskite slabs to the substrates. Thin film growth of 2D3D perovskite on a substrate can occur in three ways: parallel, perpendicular, and non-oriented.[26] In the parallel orientation, the planes of the $(Sn_nCl_{3n+1})^{(1+n)-}$ slabs are aligned parallel to the substrate, with the remaining layers stacked over them and separated by the spacer cations. Perpendicular orientation refers to the $(Sn_nCl_{3n+1})^{(1+n)-}$ perovskite slabs being oriented at a right angle to the substrate. Non-oriented growth indicates the absence of any preferentially aligned growth, as shown in Fig. S3 (Appendix).[26] A perpendicular orientation is preferred for efficient charge transfer across the perovskite layer. Previously, achieving a perpendicular orientation of the perovskite slabs in the synthesis of 2D3D perovskites required a mixture of two solvents: DMSO and DMF.[22] The use of a single solvent was found to facilitate the formation of intermediate complexes (SnI2·3DMSO) of divalent cations (Sn^{2+} or Pb^{2+}) and the solvent, which disrupted the desired perpendicular orientation.[27] Interestingly, in our approach, we discovered that the crystal slab orientation could be controlled by varying the chlorine doping percentage using a single solvent. With low chlorine doping (0-33%), the peak positions indicate trigonal crystals with crystal slabs arranged parallel to the substrate (i.e., 0k0, where k is an even integer). In the parallel orientation, all (0k0) planes are visible when k is an even number, while the (011), (202), and (213) planes are generally visible in the perpendicular orientation. At higher chlorine doping percentages (50-75%), XRD peak positions indicate tetragonal crystals with crystal slabs arranged perpendicular to the substrate, which is favorable for charge carrier movement. This means that chlorine doping can be utilized to control the orientation of 2D3D perovskite slabs, even when using a single solvent (DMF), eliminating the need for multiple solvents in 2D3D hybrid perovskite synthesis.

The change in crystal geometry and perovskite slab orientation to the substrate can be attributed to the reaction activity of chlorine, as explained in the mechanism shown in Figure 3.5. Chlorine's catalytic activity introduces new reaction kinetics, leading to different reaction rates between 2D and 3D perovskite molecules, different molecular orientations, and hence different crystal geometries.

At doping percentages above 50%, the most noticeable peak occurs at 14.1°, which is associated with the (110) direction of the tetragonal phase.[28] The peaks at positions (110), (202), and (213) indicate that the perovskite slabs are oriented perpendicularly to the substrate (i.e., 0k0, where k is a non-even integer). This perpendicular crystal orientation facilitates the efficient flow of electrons through the perovskite layer towards the electron transport layer. The clustered peaks that appear at 75% are believed to be due to impurities formed by the reactivity of excess chloride ions.

To investigate the molecular transformation from 2D to 2D3D hybrid perovskite molecules, FTIR characterization was performed on 2D3D samples with different levels of chlorine doping, as illustrated in Figure 3.3(b). When the chlorine doping is between 0-25%, a C-C stretch vibrational peak is observed at a wavenumber of 1000 cm^{-1}.[29] However, when the doping level is between 33-75%, the C-C stretch vibrational peak disappears due to changes in the molecular structure resulting from the transition from 2-dimensional (2D) perovskite molecules to more 3-dimensional-like structures (2D/3D). This transformation from linear (2D) to less linear (2D3D) molecules restrict the motion of certain atoms, hence causing the observed disappearance of the C-C vibrational peaks with increasing chlorine doping. The C-O stretch at 1,200 cm^{-1} and the broad H-O stretch (for carboxylic acids) that occurs between 2,500-3,300 cm^{-1},[30] indicate that the organic spacer part of the 2D molecule ($HOO\text{-}C(CH_2)_2(CH_2NH_3)_2SnI_4$) remains unchanged, and the reaction catalyzed by chlorine between 2D and 3D molecules only affects the quantum well. At 75% chlorine doping, the C-H bending peak shifts from 820 to 828 cm^{-1}. The shift in the C-H peak position is attributed to the molecular interactions between the 2D/3D molecules and the compounds formed by excess chlorine.

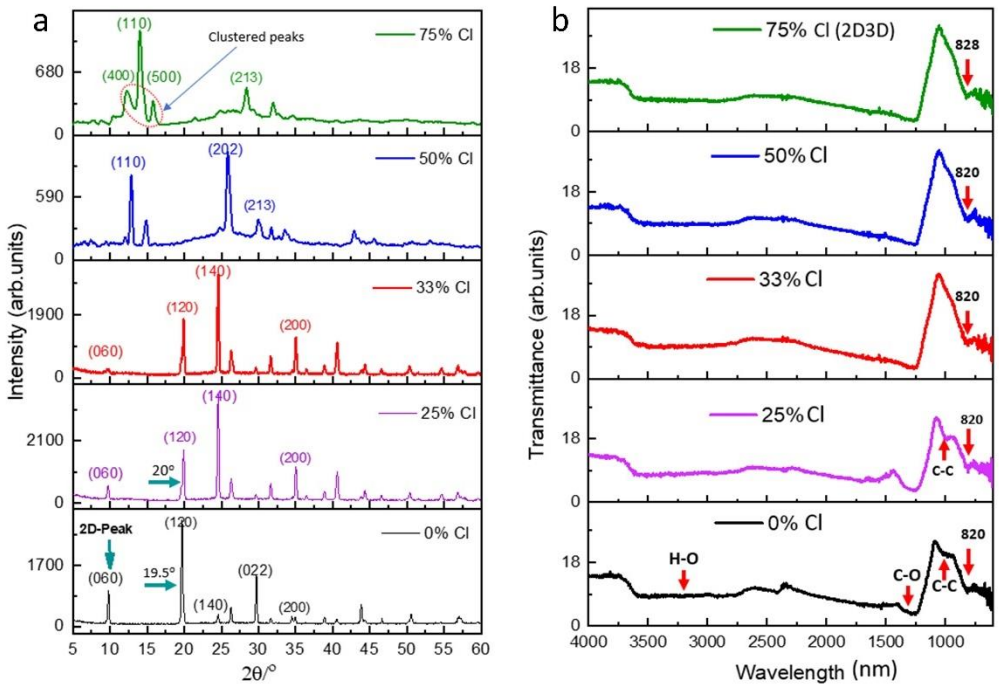

Figure 3.3 a) X-Ray diffraction patterns of 2D3D hybrid perovskite samples with different chlorine doping b) FTIR Spectra of 2D3D hybrid perovskite samples with different chlorine doping amounts.

3.2.4 Temperature and moisture stability of 2D3D perovskite materials

Heat is a major contributor to the degradation of perovskite. Figure 3.4(a) shows the differential scanning calorimetry (DSC) spectra of pure 2D and 3D perovskite samples. The DSC spectra are divided into five distinct regions: the chemical reaction region (A), glass transition region Tg (B), crystallization (C), crystal melting (D), and decomposition (E). Pure 2D perovskite (HOO-$C(CH_2)_2(CH_2NH_3)_2SnI_4$) demonstrates high thermal stability, as depicted in Figure 3.4(a). The sample releases some heat during the chemical reaction phase and does not experience any thermal changes in the Tg region, possibly due to H-bonding between adjacent 2D molecules. The high degree of orientation and hydrogen bonding lead to minimal heat release during crystallization. Due to the increased density of hydrogen bonds and the presence of large spacer cations that shield heat, the 2D sample does not melt but instead undergoes decomposition beyond the melting phase. In contrast, pure 3D ($CH_3NH_3SnI_3$) is very unstable due to the high volatility of $CH_3NH_3^+$[31], as well as the lack of significant chemical bonds and large spacer

cations. Figure 3.4(b) illustrates the thermal characteristics of 2D3D hybrid perovskite materials with different doping levels. The 0% chlorine-doped 2D3D hybrid sample shows distinct thermal changes as it absorbs and releases significant amounts of heat with increasing temperature. From 33-70% chlorine doping, the 2D3D samples exhibit increasing thermal stability with minimal heat absorption and release as the temperature rises. Unlike the 33% and 50% chlorine-doped 2D3D samples, the 75% chlorine-doped 2D3D sample releases some heat in the melting region. This melting at 75% is attributed to impurities resulting from the high reactivity of the excess chloride ions. Generally, the increase in thermal stability with increasing chlorine doping can be attributed to the corresponding decrease in the highly unstable 3D material. This breakdown releases ions responsible for transforming the 2D component into 2D3D hybrid molecules.

According to the water/perovskite contact angle analysis in Fig 3.4c, pure 2D molecules exhibit the highest water repellency (with a contact angle of 62.22^{o}) due to the effective sandwiching of moisture-sensitive quantum wells by its large spacer cations. Increasing the chlorine doping in the material catalyzes the reaction between 2D and 3D to form hybrid 2D3D molecules with large-sized quantum wells that are less shielded by the fixed-sized spacer cation part of the molecules. This, in turn, reduces the moisture stability. Pure 3D perovskite molecules ($CH_3NH_3SnI_3$) show the smallest contact angle (18.48^{o}) and the lowest moisture stability due to the absence of the sandwiching spacer cation part in their molecular structure. However, 3D molecules are structurally ionic compounds with the highly soluble methylammonium component (CH_3NH_3I).

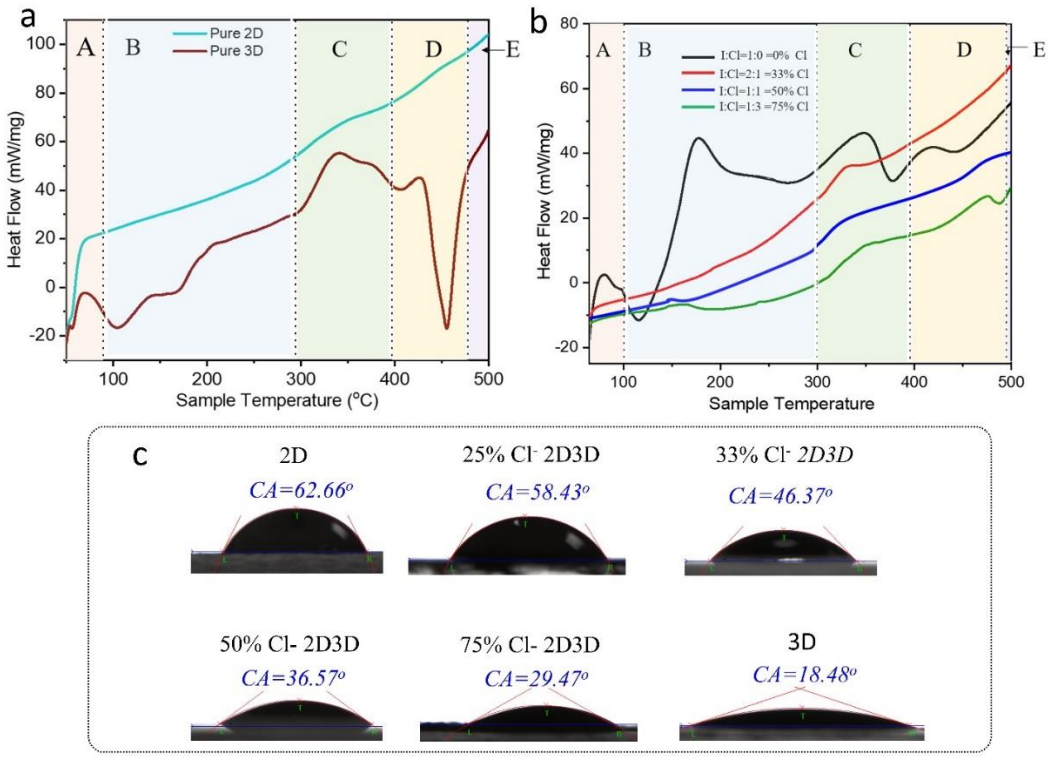

Figure 3.4 a) Differential scanning calorimetry (DSC) for Pure 2D and 3D perovskite samples b) 2D3D hybrid perovskites with different chlorine doping proportions. c) Contact angles for H_2O on pure 2D perovskite materials, 2D3D hybrid perovskite materials with varying chlorine doping percentages (25-75%), and pure 3D perovskite material.

3.3 Mechanism of chlorine catalysis leading to the formation of 2D3D perovskites

To form 2D3D hybrid perovskite molecules, the highly unstable 3D molecules decompose, releasing small and highly mobile $CH_3NH_2^+$ ions. This decomposition occurs due to factors such as heat and other influences that lead to the breakdown of perovskites.[19] The 2D molecules are ion scavengers due to their soft nature. As a result, the 2D structure can absorb and incorporate the methylammonium ions into their quantum well by modifying their pure layered structure into a quasi-2D or 2D3D structure.[32] Halogens are capable of displacement reactions, where a more reactive halogen ion (Cl^-) can displace a less reactive halogen ion (I^-) from its ionic compounds (F>Cl>Br>I). During this displacement reaction, the halogen-based compound breaks down and then reforms as a new compound with the more reactive halogen atoms.[33]

The first stage (1) in the formation of 2D3D hybrid perovskites involves the reaction between SnI_2 with CH_3NH_3I and $HOO\text{-}C(CH_2)_2(CH_2NH_3)_2I$ to create 3D and 2D perovskite molecules in solution, respectively. In stage (2), the solution containing 2D and 3D molecules is doped with chloride ions by adding $SnCl_2$. The chloride ions displace iodide ions from $CH_3NH_3SnI_3$. The ionic 3D compound is highly unstable, and the displacement of the central anion temporarily breaks down the compound, releasing $CH_3NH_3^+$, Sn^{2+}, and I- ions. The $CH_3NH_3^+$ ions are highly mobile and volatile. Due to the strong affinity of 2D molecules for the $CH_3NH_3^+$ ions, the 2D molecules absorb these ions into their quantum wells, causing a molecular transformation from 2D to 2D3D hybrid perovskite molecules. This mechanism is summarized in Figure 3.5i.

Energy-dispersive X-ray spectroscopy (EDS) characterization reveals that the displaced iodide ions make up a significant percentage on the surface of the material, and this percentage increases with higher chlorine doping, as shown in Figures 3.5ii. Since the iodine to chlorine mixing ratio was 1:1, it is expected that the 50% chlorine-doped sample would contain an approximately equal atomic proportion of iodine and chlorine on the material's surface. However, surface EDS analysis shows a higher percentage of iodine (12.08%) and a lower percentage of chlorine (8.09%). This could be because chlorine atoms were used to create the core molecules of the material, causing the displaced iodine to accumulate at the surface. Similarly, in the 75% chlorine-doped sample, the surface atomic percentage of iodine was significantly higher than that of chlorine for the same reason. It should also be noted that chloride ions also compete for the methylammonium ions, and there is a possibility of forming $CH_3NH_3SnCl_3$, especially at high percentages of chlorine doping. This explains the observed clustered peaks in XRD at 75% chlorine doping. The high electron density on the spacer part of the $HOO\text{-}C(CH_2)_2(CH_2NH_3)_2SnI_4$, caused by the carboxylic group and the large size of the molecule, helps maintain the stability of the molecule even when iodine is displaced to form the chlorine-based 2D molecule. The molecule transformation proposed in this mechanism is supported by the XRD and FTIR results in Fig. 3.3(a-b).

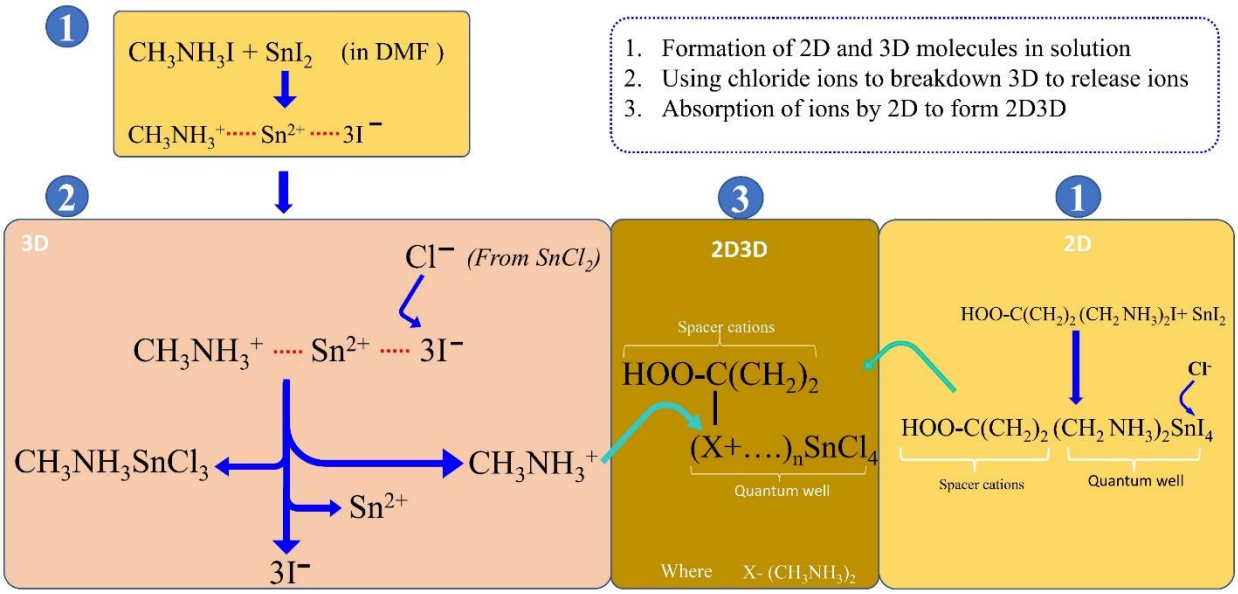

Figure 3.5i. Schematic representation of the mechanism through which chloride ions act as catalysts in the reaction leading to the formation of 2D3D hybrid perovskite molecules.

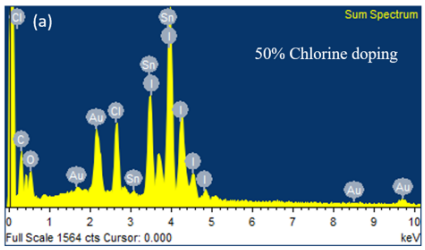

Element	Weight (%)	Atomic (%)
C K	15.39	47.66
N K	1.42	3.76
O K	8.87	20.64
Cl K	**7.71**	**8.09**
Sn L	18.20	5.70
I L	**42.21**	**12.08**
Au M	7.21	2.07
Total	100	100

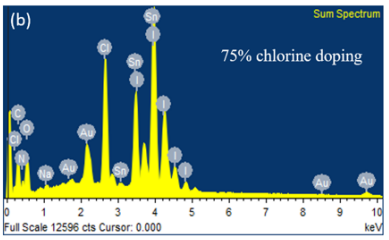

Element	Weight (%)	Atomic (%)
C K	16.00	53.74
N K	1.40	3.50
O K	4.77	12.80
Cl K	**6.49**	**7.56**
Sn L	19.31	6.99
I L	**42.45**	**13.02**
Au M	9.58	2.39
Total	100	100

Figure 3.5ii. Energy-dispersive X-ray spectroscopy (EDS) of 2D3D perovskite materials synthesized by doping with a) 50% chlorine b) 75% chlorine. The tables underneath present the percentage atomic and weight composition at the surface of each material.

3.4 Double twisted fiber-shaped solar cell assembling

Currently, there is a growing demand for portable and wearable electronic devices. As a result, flexible solar cells are becoming increasingly popular.[34] Fiber-shaped perovskite solar cells (FSPSC) are gaining attention as they exhibit similar characteristics to their planar counterparts.[35] The fiber geometry offers numerous advantages, such as enhanced flexibility, easy integration with other devices, lightweight design, and the ability to conform to the human body and other structural shapes. This has led to a significant interest in the development of highly efficient, stable, and non-toxic fiber-shaped solar cells for wearable energy harvesting applications.[36]

In this study, a coaxial structure was utilized to assemble a FSPSC with 2D3D perovskite photoactive layers doped with varying amounts of chlorine (Fig. 3.6a). The fiber-shaped device consisted of a steel yarn as the core electrode, Indium Tin Oxide paste (ITO), a 2D3D perovskite layer, an electrospun poly(3,4-ethylenedioxythiophene) polystyrene sulfonate (PEDOT: PSS) nanofiber layer as the hole transport layer (HTL), and finally twisted with a conductive silver yarn as the top electrode. The assembly process of the solar yarn begins with a pristine steel yarn with an average diameter of 900 μm (SEM in Fig. 3.6b), which is then coated with a uniform layer of Indium Tin Oxide paste, as shown in Figure 3.6(c). The ITO paste used in this process had a composition of In:Sn = 90/10, with an average particle size of 50 nm (see XRD and additional information on ITO paste in Figure S4 Appendix). Subsequently, the steel yarn is dip coated in chlorine-doped 2D3D perovskite solutions to deposit the photoactive layer.

3.4.1 Optimizing perovskite layer deposition on fiber-shaped substrates

We initially tried the conventional dip coating method, which involved dipping the steel/ITO yarn once in the 2D3D perovskite solution. Then, we placed the coated sample on a glass slide and heated it at 100°C for 7 minutes (heating by conduction). However, we found that this method resulted in a non-uniform perovskite layer on the cylindrical yarn, with multiple cracks (see Figure 3.6i(a)). To overcome this challenge, we proposed a new approach. This approach includes two dip-coating cycles, zero-contact heating (convection heating), and heating in two temperature phases. The purpose of the two dip-coating cycles is to fill the cracks in the

perovskite layer with perovskite grains, achieving uniformity. Zero-contact heating is used to prevent overheating of one side of the yarn, particularly the side in contact with the heating surface. Overheating one side creates stress in the perovskite layer due to the significant temperature difference, leading to crack formation. Heating in two temperature phases provides several advantages. The low-temperature phase (50°C) promotes slow but successful primary nucleation (germination) and secondary nucleation (crystal growth). The high-temperature phase (100°C) facilitates tertiary crystal growth (crystal clustering) and further solvent evaporation. Convection heating, which involves heating the air around the yarn, ensures uniform heating and crystallization. As a result of this approach, we were able to achieve a smooth perovskite layer on the fiber substrate (see Fig. 3.6i(b)).

3.4.2 Optimization of PEDOT: PSS nanofiber HTL layer

After successfully depositing the perovskite layer, the yarn was then wrapped with electrospun PEDOT: PSS nanofibers to serve as the hole transport layer. The cross-section and surface SEM images in Figure 3.6(e-g) illustrate this process. To enhance the electrospinnability of PEDOT: PSS, it was mixed with a carrier polymer called Polyvinylpyrrolidone (PVP) in a ratio of 3.25/0.015 g, respectively. This mixture was dissolved in 0.55 g of DMF solvent and then electrospun under the following conditions: 27 kV, 25^{o}C chamber temperature, 15 cm needle tip to yarn separation distance, and an extrusion rate of 0.4 ml/hr. The PEDOT: PSS nanofiber layer needs to possess two important qualities: transparency and conductivity. In order to optimize this layer and ensure it meets these requirements, we produced five nanofiber samples through electrospinning on Pure glass. Each sample had a different electrospinning duration, ranging from 7 to 35 minutes.

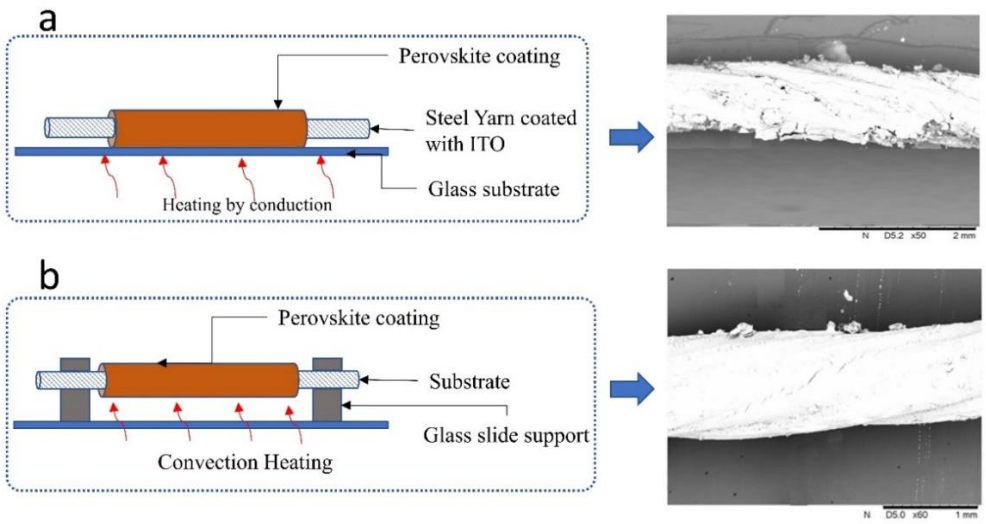

Figure 3.6i. a) Heating by conduction on a glass slide, single dip-coating, and rapid heating. Ensuing yarn from the ordinary dip-coating and heating approach. b) Heating by convection, with 2 dip-coating cycles and step by step heating, and the smooth perovskite coated yarn.

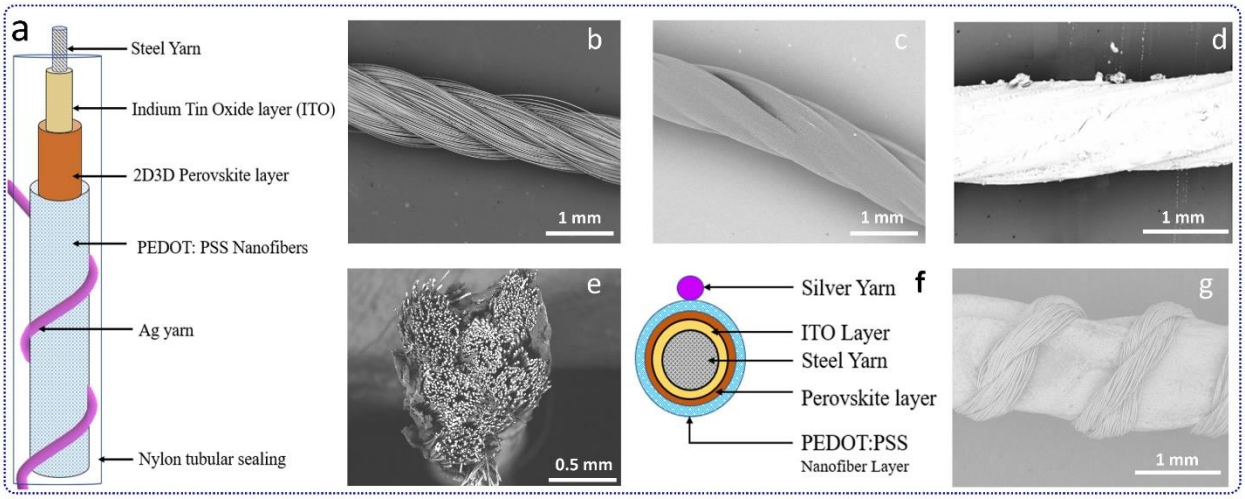

Figure 3.6ii. a) Schematic illustration of the fiber-shaped solar yarn architecture. b-d) Surface SEM images of; Pristine steel yarn, ITO coated steel yarn, and Steel/ITO/perovskite assembly, respectively. e-f) SEM images of the full cross-section of the Steel/ITO/Perovskite/PEDOT: PSS nanofibers. g) Surface SEM image of the silver yarn twisted complete solar yarn device. f) Schematic illustration of the solar yarn cross-section.

The transmittance of the electrospun samples was compared to that of 1 mm thick pure glass (quartz) and spin-coated and dip-coated PEDOT: PSS films, as shown in Figure 3.7(a). The electrical resistance of the electrospun, spin-coated, and dip-coated samples was determined and

presented in Table S2 (Appendix). To find a balance between transmittance and conductivity, we determined that a 15-minute electrospun nanofiber layer was optimal. This layer had a resistance of 7.56 kOhm and a transmittance greater than 70% in the 350∼850 nm wavelength range. PEDOT: PSS, as an HTL material, offers several cutting-edge advantages including high conductivity, excellent thermal stability, high transparency in the visible range, outstanding flexibility and stretchability, and a broad oxidation potential window of 1.2-1.5V.[37] Using nanofiber-based HTL (PEDOT:PSS) provided a large surface area of contact between the nanofibers and the Ag top electrode. A short and constant twist length of about 0.5cm was ensured to further enhance contact between the Ag yarn electrode and the PEDOT:PSS nanofiber layer. The large surface area associated with nanofibers and the short twist length ensured constant contact and increased charge transfer from the PEDOT:PSS nanofibers to the Ag top electrode.[37]

The Steel/ITO/Perovskite/PEDOT: PSS structural assembly was completed by twisting it with a pristine silver yarn with an average diameter of 350 μm, forming the solar yarn structure. To enhance the degradation resistance of the solar yarn under normal operating conditions, the device was vacuum-sealed using a commercial Nylon 66 material and a simple vacuum sealing machine (Model: Nesco VS-12 Deluxe vacuum sealer). Commercial Nylon 66 was chosen as the vacuum sealing material due to its high transmittance, which is comparable to that of pure glass in the range of 300∼850 nm. Additionally, it has low moisture (5.803–114.314 g mm^{-2} s^{-1} Pa^{-1} ($x10^{14}$)) and air (0.010–0.098 $mLmm^{-2}$ day^{-1} Pa^{-1} ($x10^{7}$)) permeability[38], as well as excellent thermal sealing properties. Figure 3.7(b) illustrates the transmittance comparison between pure glass, 76 μm thick commercial Nylon 66 for vacuum sealing, and the ITO paste coated layer.

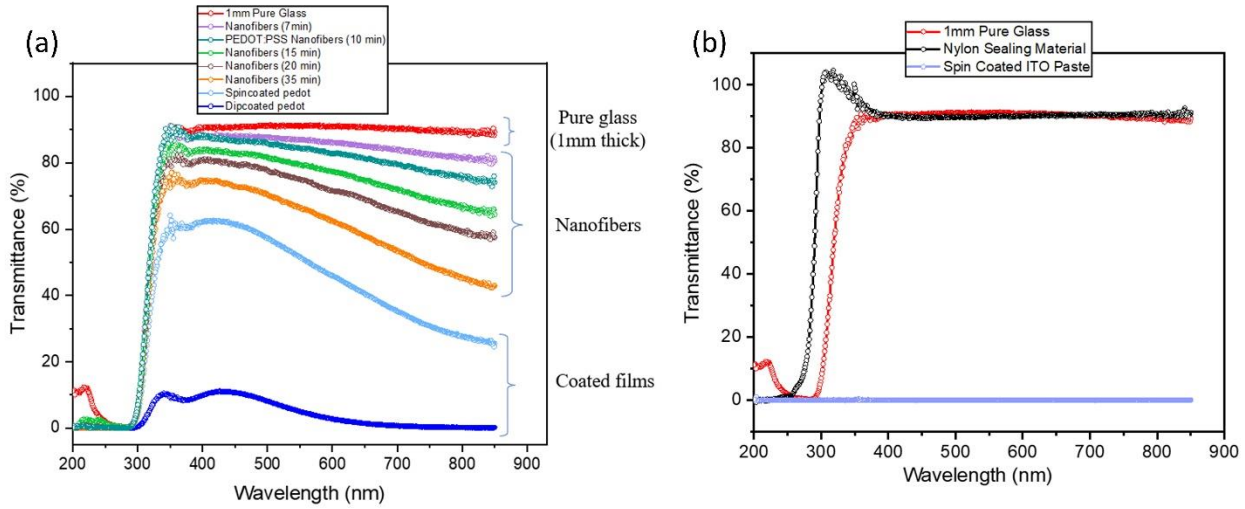

Figure 3.7 a) Variation of transmittance with wavelength for electrospun, spin-coated, and dip-coated PEDOT: PSS samples. b) Transmittance versus wavelength for vacuum sealing nylon, ITO paste material compared with pure glass.

3.5 Double twisted fiber-shaped solar cell characterization

Figure 3.8(a) displays the photovoltaic performance of 2D3D perovskite materials with different chlorine doping percentages in a solar yarn device structure. The tests were conducted under 1 sun (1000 Wm^{-2}) solar illumination, at an air mass of 1.5 G. The optimized Steel/ITO/2D3D perovskite/PEDOT: PSS yarn has a diameter of ≈ 1.2 mm (1200 μm), and considering an illuminated length of 5.5 cm, the projected active surface area was determined to be approximately 1.884 cm^2. The top area shadowed by the top silver yarn electrode is not taken into account. No adjustments were made to account for optical losses caused by reflections from the curvature of the primary fiber or the curved air/polymer coating interface.

To investigate the impact of chlorine doping in the 2D3D perovskite material on the photon-electric conversion of the fiber-shaped 2D3D perovskite-based solar yarns, different yarns with varying chlorine doping percentages in their photoactive layers were assembled and characterized. The champion solar cells' characterization results for different chlorine doping categories are presented in Table 3.1. As shown in Fig. 3.8(a) and Table 3.1, increasing the chlorine doping percentage in the 2D3D perovskite material significantly enhances the PCE, short circuit current (JSC), open circuit voltage, and fill factor up to a maximum doping percentage of 50%. Beyond this point, the photovoltaic performance of the yarn decreases. The

gradual improvement in the quality and performance of the solar yarns is attributed to the catalytic activity of chlorine ions, which contribute to the effective formation of hybrid 2D3D perovskite molecules that are responsible for larger perovskite crystals, smoother layer formation, and increased charge carrier lifetime.

The maximum PCE values increase from 5.84% at 0% chlorine doping to a maximum of 11.96% at 50% chlorine doping. The best device with 50% chlorine doping also exhibits the highest open circuit voltage (Voc) of 1.11 V, short circuit current (Jsc) of 29.91 $mAcm^{-2}$, and a fill factor of 76.5%. To the best of our knowledge, 11.96% represents the highest reported PCE in Sn-based fiber-shaped perovskite solar cells.

Table 3.1 Variation of photovoltaic outputs with increasing doping of chlorine in the 2D3D material, keeping the solar yarn architecture constant (steel yarn/ITO/2D3D Perovskite/PEDOT: PSS/Steel Yarn). 15 samples were prepared and characterized from each category.

% of Cl^- to I^-	PCE (%)	Fill factor (FF) (%)	J_{SC} (mA cm^{-2})	V_{oc} (V)
0	5.84	64.5	13.5	1.04
25	7.54	68.4	20.2	1.06
33	9.42	72.2	25.08	1.07
50	11.96	76.5	29.91	1.11
75	10.61	70.3	31.97	1.09

To guarantee stable performance in wearable electronic devices, it is crucial to examine their ability to withstand twisting and bending. In this study, we assessed the bending stability of the solar yarn by subjecting it to 500 bending cycles with a loop diameter of 0.5 cm. Figure 3.8(b) shows that the solar yarn maintained over 95% of its original power conversion efficiency (PCE) after the 500 bending cycles. The bending stability of the yarn is attributed to the synergy of the wrapping effect of the PEDOT: PSS nanofiber layer and vacuum sealing bag, which provide structural integrity and consolidation of the yarn structure. However, the bending process can cause film rupture, which affects the transmission of charge carriers. This results in a decrease in

the short-circuit current density and open circuit voltage, as shown in Fig. S5 (a-b) (Appendix). On the other hand, the bending process also tightens the contact between the layers, leading to a gradual increase in the fill factor (Fig. S5(C), Appendix) and a slight increase in the PCE after several bending cycles. This type of stability is beneficial for the wearability, weave-ability, and knittability of the solar yarns.

In practical applications, solar devices are exposed to hot and extremely cold weather conditions during summer and winter, respectively. To demonstrate tolerance to temperature variations, the 2D3D-based solar yarns were stored at different temperatures for 10 minutes before testing. Figure 3.8(c) shows that the solar yarns maintained over 98% of their original PCEs over a wide temperature range from 4 to 120°C. The thermal stability of the solar yarn with a 50% doping percentage is attributed to the thermal stability of the 2D3D hybrid perovskite material formed after chlorine doping, as explained in DSC Figure 3.4(a). The slight drop in PCE below 5°C and above 90°C is presumed to be caused by the contraction and expansion of the silver and steel metallic electrodes, which impact the different layers in the structure and their interfaces. However, high temperatures can negatively affect the PEDOT: PSS nanofibers, as they can undergo a glass transition, which in turn affects their hole transport properties.

Figure 3.8(d) displays the distribution of power conversion efficiency of 50 samples prepared with 50% Cl^- doped materials. The narrow efficiency distribution of the devices produced demonstrates the high repeatability of the method and is also beneficial for the industrialization and mass production of the devices.

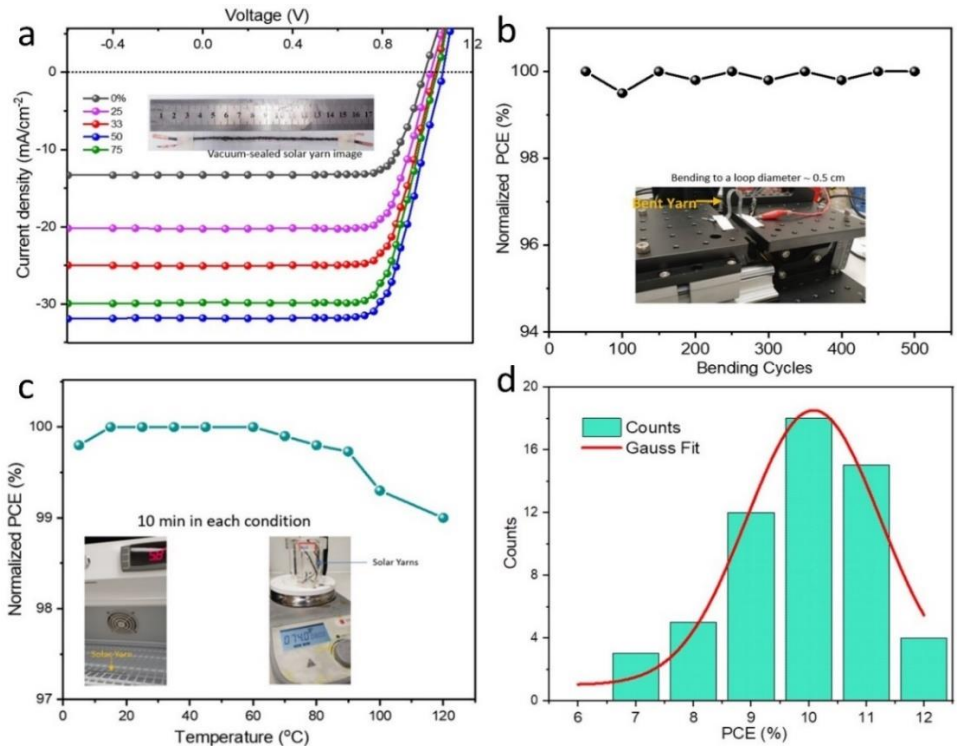

Figure 3.8 a) J-V curves of fiber-shaped solar cells with different chlorine doping levels in the 2D3D perovskite photoactive layer. b) Normalized PCE values as a function of bending. c) Normalized PCE values as a function of the working temperature. d) Device efficiency distributions.

The service lifetime of fiber-shaped perovskite solar cells remains a major challenge in their commercialization. This issue is particularly severe for tin-based perovskite solar cells due to rapid oxidation, resulting in material decomposition and performance loss. In our study, we focused on enhancing the stability and energy conversion efficiency of 2D3D hybrid perovskite material. Additionally, we introduced a vacuum sealing approach for the solar yarn, which was enclosed in a nylon 66 bag with protruding electrodes. Figure 3.9(a) shows that the normalized power conversion efficiency (PCE) of the bare device decreased to 75% after ~2,000 hours in open air. However, the vacuum-sealed yarn maintained over 98% of its original PCE under room light with 35-40% relative humidity. This represents the highest stability achieved for Sn-based fiber-shaped perovskite solar cells. The commercial vacuum sealing approach eliminates moisture from the sealed environment of the yarn, resulting in enhanced stability compared to conventional sealing methods. The good stability of 2D3D hybrid perovskite solar cells can be attributed to the large hydrophobic spacer cation part of the molecule, which protects the quantum well from exposure to moist air and other degrading conditions.

The cylindrical geometry, novel double-twisted architecture, and PEDOT:PSS nanofiber layer of the solar yarn minimize reflection of incident rays. As shown in Figure 3.9(b), the normalized PCE of the solar yarn remains nearly unchanged when the incident angle of the incoming light varies from 0° to 180°. This demonstrates that there is little correlation between the light incident angle and the photovoltaic performance of the yarn, which is a promising characteristic for self-powering textiles. In practical applications, wearable optoelectronics experience frequent and unprecedented movements that result in different incident angles of light. The constant energy output at all incident angles ensures a uniform power supply from the solar yarns. In summary, the solar yarn exhibits a sunflower-like behavior, where it does not need to follow the direction of the sun to maintain a constant energy output.

A slight increase in PCE was observed at an illumination angle of 90°, which can be attributed to the relatively small cross-sectional area of the solar yarn (approximately 1.13 mm^2). This cross-section is much smaller than the illuminating diameter of the Xenon lamp (50 x 50 mm^2). Therefore, at 90°, the solar yarn receives maximum illumination on its photoactive surface area, with less shadowing compared to other angles.

Figure 3.9(d) displays a parallel assembly of six vacuum-sealed yarns, which can function as a solar wristband to provide power for a smartwatch. The solar yarns, woven and knitted into perovskite solar fabrics, offer non-toxicity and relatively stable performance, owing to factors such as frictional resistance, bending stability, and sealing.

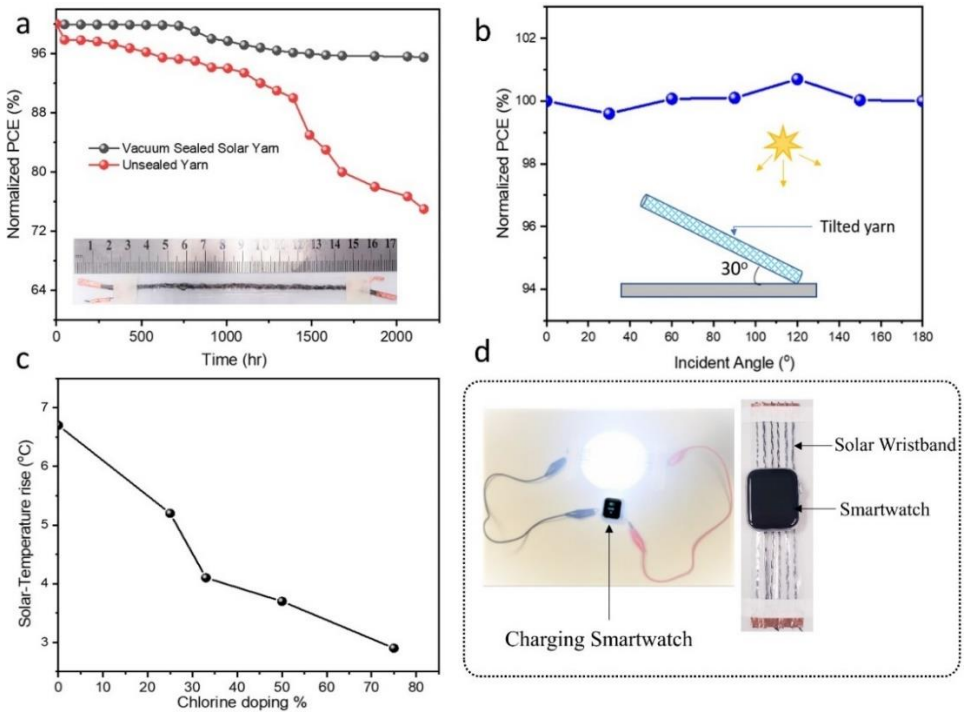

Figure 3.9 a) Stability test for the solar yarn devices under continuous room light at 35-40% relative humidity with and without encapsulation. b) Variation of PCE with changing light incident angles. c) Variation of solar yarn temperature rise upon light exposure for 10 minutes with increasing chlorine doping in the perovskite material. d) Camera images of an assembly of solar yarns under simulated light charging a smartwatch and a demonstration of solar-powered smartwatch assembly.

3.6 Solar-thermal dissipation analysis

During operation, solar devices generate heat through non-radiative recombination.[39] The amount of heat produced by a solar device depends on the photoactive material used and the composition of other layers. When photons are absorbed by the photoactive layer, some of the energy is used to generate free charge carriers, while another portion is used to move electrons from the valency band to the conduction band. Any remaining energy that is not used in the photoelectric process is released as heat.

Table 3.2 and Figure 3.9c demonstrate that the temperature of solar yarns increases after being exposed to simulated light for 10 minutes. Generally, the temperature rise decreases as the chlorine doping level increases, indicating that yarns with higher chlorine doping release less heat during photoelectric activity. This trend can be attributed to the fact that increasing chlorine

doping shifts the absorption peaks of the photoactive materials from shorter wavelengths (350-500 nm) to longer wavelengths (550-850 nm) in the UV/Vis spectrum, as shown in Fig. 3.2(a-c). Shorter wavelengths of light carry higher photon energy (350∼500 nm = 3.5∼2.48 eV), while longer wavelengths carry lower photon energy (550∼850 nm = 2.25∼1.45 eV). Therefore, all other factors being equal, photoactive materials that absorb shorter wavelengths release more unused energy as heat because they absorb photons with higher energy. The excess thermal energy released can lead to the decomposition of the photoactive layer and cause discomfort to the wearer of the wearable optoelectric device. The solar-thermal dissipation analysis was conducted using a thermal camera (FLIR C5 thermal imaging camera) positioned 10 cm away from the samples. Each sample was exposed to light for 10 minutes, and the final temperatures were immediately measured.

Table 3.2 Variation of solar-thermal heat dissipation from the solar yarn devices with the increasing chlorine doping before and after 10 minutes of illumination with simulated light.

Chlorine doping %	0% Cl	33% Cl	50% Cl	75% Cl
Initial sample Temperature	*23.9°C*	*24.0°C*	*23.6°C*	*23.4°C*
Solar Yarn Samples Before light exposure	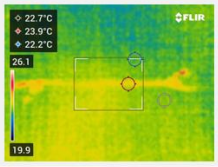	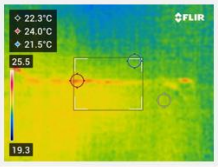	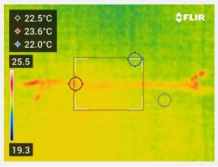	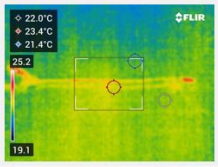
Light exposure for 10 minutes				
Solar Yarn Samples After light exposure	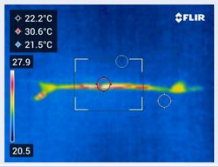	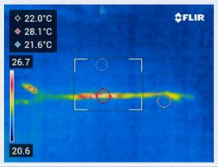	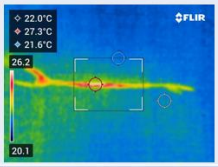	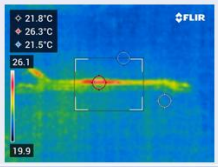
Final temperature	*30.6°C*	*28.1°C*	*27.3°C*	*26.3°C*
Temperature Rise (during photo-electric activity)	*6.7°C*	*4.1°C*	*3.7°C*	*2.9°C*

3.7 Key research findings and outputs in chapter three

In this work package, the following were the key outputs and achievements, in line with the set objectives of our study.

1. In this study, we completely replaced toxic Pb with non-toxic Sn cations in perovskite materials, and we realized lead-free fiber-shaped perovskite solar cells.
2. Developed a material synthesis approach that reduces the effective reaction time between 2D and 3D perovskite molecules to ~20 minutes, and the reaction temperature to ~100ºC with the formation of high-quality 2D3D hybrid perovskite, free from pure 2D traces.
3. By incorporating the hybrid material in a solar cell device, we achieved high PCE of 11.96% in Sn-based fiber-shaped perovskite solar cells.
4. The thermal stability of the synthesized hybrid material enabled the ensuing solar device to have good temperature stability from 5 ~ 100ºC, with minimal loss in its power conversion efficiency.
5. The incorporation of a nanofiber layer of PEDOT: PSS (HTL) that wraps the device assisted in maintaining structure integrity of the fiber-shaped solar cell, and brought about outstanding bending stability of more than 500 bending cycles, with minimum loss in efficiency.
6. The good moisture and air stability of the synthesized 2D3D perovskite material yielded the highest reported performance lifetime in Sn-based solar cells; 75% efficiency retention after 2000 hours.
7. Lastly, in this work package, we developed an optimized perovskite layer deposition technique on fiber-shaped/curved substrates, for high quality material depositions. This was achieved through multiple dip-coatings and a two-step heating process.

3.8 Conclusion

In summary, we have developed a method for synthesizing hybrid 2D3D perovskite material by using chloride ions as a catalyst to speed up and control the reaction between $CH_3NH_3SnI_3$ (3D) and $(HOOC(CH_2)_4NH_3)_2PbI_4$) 2D. We can achieve this at a relatively low temperature and shortened reaction time.

Our approach is based on the ability of chloride ions to displace iodide ions from their ionic compounds in solution. This causes a temporary breakdown of the 3D molecules, releasing $CH_3NH_3^+$, Sn^{2+}, and I^- ions. The stable 2D ion scavenger molecules and the chloride ions in

solution compete for these released ions. When the 2D molecules incorporate ions (especially $CH_3NH_3^+$) into their quantum wells, they grow in a more 3D-like pattern and form hybrid 2D3D molecules with properties that are intermediate between those of pure 2D and pure 3D. The concentration of chloride ions added to the iodine-based mixture of 2D and 3D molecules determines the rate of formation of stable and efficient 2D3D hybrid perovskite molecules. By using chloride ions to influence the reaction, we can synthesize perovskite slabs with a perpendicular orientation to the substrate without the need for multiple solvents, as previous attempts have required. Moreover, this approach allows us to control crystal geometry, ranging from trigonal (0% ~33% Cl- doping) to tetragonal (>50%).

Finally, our synthesis approach achieves a complete reaction of the 2D and 3D perovskite molecules, resulting in a hybrid 2D3D material with no traces of the 2D phase when the halogen percentage of chlorine in the material is at 50%. Based on our findings, this approach is a flexible, fast, cost-effective, and highly efficient method for synthesizing single-phase hybrid 2D3D perovskite material with enhanced efficiency and stability. We also believe that this approach can be used to synthesize not only Sn-based but also Pb-based 2D3D hybrid perovskites.

3.9 References

1. Zhang, L., X. Zhou, C. Liu, X. Wang, et al., A Review on Solution-Processable Dopant-Free Small Molecules as Hole-Transporting Materials for Efficient Perovskite Solar Cells. Small Methods, 2020. **4**(9): 2000254.

2. Asif, A.A., R. Singh, and G.F. Alapatt, Technical and economic assessment of perovskite solar cells for large scale manufacturing. JRSE, 2015. **7**(4): 043120.

3. Binek, A., M.L. Petrus, N. Huber, H. Bristow, et al., Recycling perovskite solar cells to avoid lead waste. Acs Appl Mater Inter, 2016. **8**(20): 12881-12886.

4. Zhao, M.-M., L. Zhou, P.-P. Shi, X. Zheng, et al., Halogen substitution effects on optical and electrical properties in 3D molecular perovskites. Chem commun, 2018. **54**(94): 13275-13278.

5. Zhang, F., D.H. Kim, and K. Zhu, 3D/2D multidimensional perovskites: balance of high performance and stability for perovskite solar cells. Curr. Opin. Electrochem, 2018. **11**: 105-113.

6. Lakhdar, N. and A. Hima, Electron transport material effect on performance of perovskite solar cells based on CH3NH3GeI3. Optical Materials, 2020. **99**: 109517.

7. Jain, S.M., T. Edvinsson, and J.R. Durrant, Green fabrication of stable lead-free bismuth based perovskite solar cells using a non-toxic solvent. Communications Chemistry, 2019. **2**(1): 1-7.

8. Wang, S., A. Wang, F. Hao, and L. Ding, Renaissance of tin halide perovskite solar cells. J. Semicond, 2021. **42**(3): 030201.

9. Lanzetta, L., T. Webb, N. Zibouche, X. Liang, et al., Degradation mechanism of hybrid tin-based perovskite solar cells and the critical role of tin (IV) iodide. Nat. Commun, 2021. **12**(1): 1-11.

10. Wang, T., Q. Tai, X. Guo, J. Cao, et al., Highly air-stable tin-based perovskite solar cells through grain-surface protection by gallic acid. ACS Energy Lett, 2020. **5**(6): 1741-1749.

11. Tai, Q., X. Guo, G. Tang, P. You, et al., Antioxidant grain passivation for air-stable tin-based perovskite solar cells. Angew. Chem. Int. Ed, 2019. **58**(3): 806-810.

12. Chen, Y., Y. Sun, J. Peng, J. Tang, et al., 2D Ruddlesden–Popper perovskites for optoelectronics. Adv. Mater, 2018. **30**(2): 1703487.

13. Tsai, H., W. Nie, J.-C. Blancon, C.C. Stoumpos, et al., High-efficiency two-dimensional Ruddlesden–Popper perovskite solar cells. Nature, 2016. **536**(7616): 312-316.

14. Zuo, C., A.D. Scully, D. Vak, W. Tan, et al., Self-assembled 2D perovskite layers for efficient printable solar cells. Adv. Energy Mater, 2019. **9**(4): 1803258.

15. Krishna, A., S. Gottis, M.K. Nazeeruddin, and F. Sauvage, Mixed dimensional 2D/3D hybrid perovskite absorbers: the future of perovskite solar cells? Adv. Funct. Mater, 2019. **29**(8): 1806482.

16. Jagielski, J., S. Kumar, W.-Y. Yu, and C.-J. Shih, Layer-controlled two-dimensional perovskites: synthesis and optoelectronics. J. Mater. Chem. C, 2017. **5**(23): 5610-5627.

17. Misra, R.K., B.E. Cohen, L. Iagher, and L. Etgar, Low-dimensional organic–inorganic halide perovskite: structure, properties, and applications. ChemSusChem, 2017. **10**(19): 3712-3721.

18. Grancini, G., C. Roldán-Carmona, I. Zimmermann, E. Mosconi, et al., One-Year stable perovskite solar cells by 2D/3D interface engineering. Nat. Commun, 2017. **8**(1): 1-8.

19. Sutanto, A.A., N. Drigo, V.I. Queloz, I. Garcia-Benito, et al., Dynamical evolution of the 2D/3D interface: a hidden driver behind perovskite solar cell instability. J. Mater. Chem. A, 2020. **8**(5): 2343-2348.

20. Smith, I.C., E.T. Hoke, D. Solis-Ibarra, M.D. McGehee, et al., A layered hybrid perovskite solar-cell absorber with enhanced moisture stability. Angew. Chem. Int. Ed, 2014. **53**(42): 11232-11235.

21. Ye, T., A. Bruno, G. Han, T.M. Koh, et al., Efficient and Ambient-Air-Stable Solar Cell with Highly Oriented 2D@ 3D Perovskites. Adv. Funct. Mater, 2018. **28**(30): 1801654.

22. Chen, X., M. Ding, T. Luo, T. Ye, et al., Self-assembly of 2D/3D perovskites by crystal engineering for efficient air-processed, air-stable inverted planar perovskite solar cells. ACS Appl. Energy Mater, 2020. **3**(3): 2975-2982.

23. Tidhar, Y., E. Edri, H. Weissman, D. Zohar, et al., Crystallization of methyl ammonium lead halide perovskites: implications for photovoltaic applications. J. Am. Chem. Soc, 2014. **136**(38): 13249-13256.

24. Huang, Y., L. Li, Z. Liu, H. Jiao, et al., The intrinsic properties of FA (1− x) MA x PbI 3 perovskite single crystals. J. Mater. Chem. A, 2017. **5**(18): 8537-8544.

25. Mercier, N., (HO2C (CH2)(3) NH3)(2)(CH3NH3) Pb2I7: a predicted noncentrosymmetrical structure built up from carboxylic acid supramolecular synthons and bilayer perovskite sheets. CrystEngComm, 2005. **7**: 429-432.

26. Cao, D.H., C.C. Stoumpos, T. Yokoyama, J.L. Logsdon, et al., Thin films and solar cells based on semiconducting two-dimensional ruddlesden–popper (CH3 (CH2) 3NH3) 2 (CH3NH3) n− 1Sn n I3 n+ 1 perovskites. ACS Energy Lett, 2017. **2**(5): 982-990.

27. Hao, F., C.C. Stoumpos, P. Guo, N. Zhou, et al., Solvent-mediated crystallization of CH3NH3SnI3 films for heterojunction depleted perovskite solar cells. J. Am. Chem. Soc, 2015. **137**(35): 11445-11452.

28. Wang, F., X. Li, H. Wang, Y. Gou, et al., Supramolecular bridging strategy enables high performance and stable organic-inorganic halide perovskite solar cells. J. Chem. Eng, 2022: 137431.

29. Guerrero-Pérez, M.O. and G.S. Patience, Experimental methods in chemical engineering: Fourier transform infrared spectroscopy—FTIR. Can. J. Chem. Eng, 2020. **98**(1): 25-33.

30. Mahdi, H., An FTIR study of characterization of neat and UV stabilized nylon 6, 6 polymer films. IHJPAS, 2017. **24**(1).

31. Qin, M., J. Cao, T. Zhang, J. Mai, et al., Fused-Ring Electron Acceptor ITIC-Th: A Novel Stabilizer for Halide Perovskite Precursor Solution. Adv. Energy Mater, 2018. **8**(18): 1703399.

32. Cao, D.H., C.C. Stoumpos, O.K. Farha, J.T. Hupp, et al., 2D homologous perovskites as light-absorbing materials for solar cell applications. J. Am. Chem. Soc, 2015. **137**(24): 7843-7850.

33. Trowbridge, P., Perhalides of Quinoline. J. Am. Chem. Soc, 1899. **21**(1): 66-72.

34. Balilonda, A., Q. Li, X. Bian, R. Jose, et al., Lead-free and electron transport layer-free perovskite yarns: Designed for knitted solar fabrics. J. Chem. Eng, 2021. **410**: 128384.

35. Balilonda, A., Z. Li, Y. Fu, F. Zabihi, et al., Perovskite fiber-shaped optoelectronic devices for wearable applications. J. Mater. Chem. C, 2022. **10**(18): 6957-6991.

36. Zhai, W., Z. Zhu, X. Sun, and H. Peng, Fiber Solar Cells from High Performances Towards Real Applications. Adv. Fiber Mater, 2022. **1-11**: https://doi.org/10.1007/s42765-022-00184-1.

37. Song, H. and K. Cai, Preparation and properties of PEDOT: PSS/Te nanorod composite films for flexible thermoelectric power generator. Energy, 2017. **125**: 519-525.

38. Bastarrachea, L., S. Dhawan, and S.S. Sablani, Engineering properties of polymeric-based antimicrobial films for food packaging: a review. Food Eng. Rev, 2011. **3**(2): 79-93.

39. Couderc, R., M. Amara, and M. Lemiti, In-depth analysis of heat generation in silicon solar cells. IEEE J. Photovolt, 2016. **6**(5): 1123-1131.

Chapter 4: High Performance and Efficiency Recovery in Sn-based Flexible Perovskite Solar Cells by Antioxidant Vanillin and Microwave Treatment

4.1 Introduction

Perovskite solar cells are known for their low cost (Levelized Cost of Electricity ~ 3.5–4.9 US cents/kWh)[1] and easy fabrication using solution processing methods such as dip-coating,[2] spin-coating,[3] electrospinning, spray coating, roller printing, etc.[4] The global market for PSCs is projected to expand at a rate of 32.0% annually by 2026, reaching USD 2.35 billion.[5] However, before perovskite solar cells can be commercialized, critical concerns need to be addressed, including the stability of volatile organic components like $CH_3NH_3^+$ and the toxicity of lead (Pb) contamination.[6] To overcome these concerns, researchers have focused on lead-free perovskites, particularly tin-based variants ($ASnX_3$), as the toxicity of Pb perovskites hinders their practical application.[7] The high reactivity and limited absorption range of strontium (Sr), despite its similar ionic radius and valence state to Pb, make it unsuitable.[2] Among the viable substitutes proposed, Sn (II) perovskites stand out due to their high UV-vis absorption capacity, minimal exciton binding energy, and high charge carrier mobility, making them the most suitable alternative for Pb in terms of photovoltaic performance.[8] Sn-based perovskites also have optical bandgaps that are close to the ideal bandgap for the Shockley-Queisser limit under the AM 1.5 solar spectrum.[9] However, Sn^{2+} readily oxidizes to Sn^{4+} when exposed to air or environments with small amounts of oxygen.[10] This results in undesired p-doping (high conductivity) of the perovskite film and the formation of Sn vacancies in the lattice, leading to the failure of Sn-based PSCs. Achieving long-term stability in tin PSCs is therefore challenging, and previously reported devices without sufficient enclosure deteriorated quickly in open air.[11]

4.1.1 Inorganic antioxidants of perovskite materials

To address the issue of rapid oxidation, various antioxidants have been proposed and used to suppress the formation of Sn^{4+} defects. Some antioxidants also act as supplements of Sn sources, such as SnX_2 (X = F-, Cl-) and the SnF_2–pyrazine complex.[12] In one study, Cao et al.[13] utilized ammonium hypophosphite to achieve antioxidation of the $FASnI_3$ perovskite precursor. This not

only suppressed the oxidation of Sn^{2+}, but also facilitated successful perovskite crystallization. As a result, the resulting solar cells maintained 50% normalized PCE after 500 hours of aging, while the control devices deteriorated rapidly within 100 hours. Li et al.[14] employed Hypophosphorous acid (HPA) as an antioxidant with a P-O bond that coordinated with Sn^{2+} in $CsSnIBr_2$. By doping with HPA, they achieved a PCE of 3.2% and the device demonstrated relative stability in PCE for a period of 77 days. In order to create a reducing atmosphere during the fabrication of perovskite films, organic reducing agents with high solubility are highly suitable. Furthermore, coordination with Sn^{2+} is necessary to delay crystallization and enhance the quality of perovskite crystals.

4.1.2 Organic antioxidants on perovskite materials

Mohammadian-Sarcheshmeh et al.[15] demonstrated the potential of uric acid as a natural organic antioxidant in enhancing the performance and stability of tin perovskite solar cells. This was achieved through a significant reduction in Sn^{2+} oxidation and charge carrier recombination. Wang et al.[16] utilized gallic acid (GA) as an antioxidant to improve the performance of tin PSCs. The study found that the $SnCl_2$-GA complex effectively conducted electrons and shielded the perovskite grains from fast oxidation, resulting in highly stable and efficient PSCs. Even when stored for 1000 hours in ambient air with 20% relative humidity, the unencapsulated devices retained nearly 80% of their initial efficiency.

Liu et al.[17] experimented with caffeic acid (CA), a natural antioxidant, to suppress the oxidation of Sn^{2+} in perovskite and control the crystallization process of the mixed Pb−Sn perovskite. The device with CA-doped perovskite demonstrated a PCE of 19.85%. In comparison, the control device lost more than 40% of its initial PCE after 500 hours, while the CA-doped devices maintained 90% of the initial efficiency during the same time. Ban et al.[18] used antioxidant tea polyphenol (TP) to control perovskite film crystallization through coordination interaction, inhibit the oxidation of Sn^{2+}, and increase the open-circuit voltage. The TP-doped device achieved a PCE of 8.1% and maintained 94% of its original PCE after 60 days in a nitrogen-filled glove box. Tai et al.[19] reported air-stable $FASnI_3$ solar cells by introducing hydroxybenzene sulfonic acid as an antioxidant in the perovskite precursor solution, along with excess $SnCl_2$. The interaction between the sulfonate group and the Sn^{2+} ion led to in-situ

encapsulation of the perovskite grains with a $SnCl_2$ additive complex layer, resulting in enhanced oxidation stability of the perovskite film. The ensuing PSCs were able to maintain 80% normalized PCE after 500 hours without encapsulation. Recent research has also revealed that using uric acid (UA) as an antioxidant is a simple, efficient, and cost-effective approach to prevent the rapid oxidation of Sn^{2+} to Sn^{4+} in perovskite solar materials.[15]

However, the main challenge with the aforementioned antioxidants is that they mostly perform via a redox reaction, in which they reduce the perovskite. As a result, the antioxidants themselves become oxidized and eventually deplete over time, as the majority of the byproducts of their oxidation are non-antioxidant molecules.

In this study, we revealed the potential of vanillin, as a robust antioxidant with 2 redox reactions in succession, in enhancing both the stability and efficiency of Sn-based perovskite solar cells. Vanillin is a highly effective antioxidant used in various industries, including food, medicine, and many others. Its primary function is to prevent the oxidation of easily oxidizable substances. **Firstly**, the hydroxyl benzene group on the vanillin molecule has a higher affinity for free oxygen radicals, which makes vanillin a highly effective reducing agent.[20] Additionally, as shown in Figure 4.1, the product of vanillin oxidation, vanillic acid, also acts as an antioxidant.[20] This extends the antioxidation capability of the vanillin-doped perovskite material, surpassing what could be achieved with single-stage antioxidants and preventing rapid antioxidant depletion. **Second**, the oxygen-rich side groups of vanillin (ether, aldehyde, and phenol groups) possess a lonely pair of electrons. These electrons have the ability to facilitate coordinate and electrostatic interactions between vanillin and perovskite. As a result, they promote improved crystallization and the mending of crystal defects.[18] Another advantage is that vanillin is non-volatile, which in turn slows down the crystallization process of perovskite. It is worth noting that slow crystallization has been found to enhance crystal growth and improve crystal quality.[21] **Thirdly**, the addition of vanillin to the Sn-based perovskite material enhances its UV-vis absorbance. This is because vanillin has antioxidant properties that allow it to convert Sn4+ ions back to Sn^{2+}, thereby restoring the perovskite molecular structure and improving the overall quality of the material. In our study, we incorporated 7.5% vanillin into the Sn-based perovskite material. This vanillin-doped perovskite material was then used as the photoactive layer in a one-dimensional flexible perovskite solar cell (PEN/ITO/TiO_2/Perovskite-

vanillin/PEDOT: PSS/Pt). Remarkably, this flexible solar cell achieved an efficiency of 13.18%. Furthermore, the efficiency of the solar cells increased from 30.1% to 65.4% normalized PCE after being exposed to 160 W microwave irradiation for 3 minutes over a duration of 2200 hours.

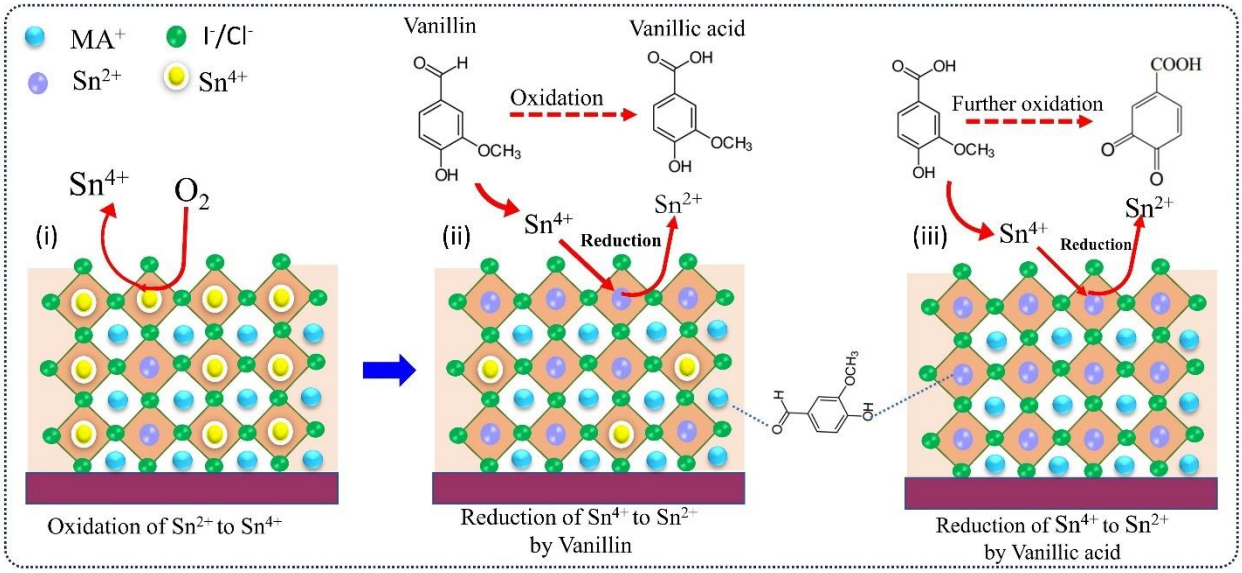

Figure 4.0. Schematic illustration of the 2-staged redox reaction between vanillin and Sn-based perovskite: i) Oxidation of Sn-based perovskite in absence of vanillin. ii) Reduction of Sn^{4+} back to Sn^{2+} and oxidation of vanillin to vanillic acid. iii) Reduction of Sn^{4+} back to Sn^{2+} and oxidation of vanillic acid.

4.2 Experimental section

4.2.1 Materials

Materials were obtained as follows: Polyethylene Naphthalate (PEN) (thickness ~ 0.125 mm, Sigma-Aldrich). Methyl ammonium (CH_3NH_3I, Tokyo Chemical Industry ≥ 99.0 wt%), Tin Iodide (SnI_2, Shanghai Bojing Chemical Co, LTD > 99 wt%), Tin Chloride ($SnCl_2$, Shanghai Bojing Chemical Co, LTD > 99 wt%), N, N-Dimethylformamide (DMF; C_3H_7NO, Shanghai Lingfeng Chemical Co, LTD ≥ 99.9 wt%), Aminovaleric acid iodide ($HOOC(CH_2)_4NH_3I$, AVAI, Tokyo Chemical Industry Co, LTD ≥ 97 wt%). Vanillin (Aladdin >99 wt%), Vanillic acid (Aladdin >99 wt%), Titanium dioxide (TiO_2 anatase 99.8 wt% metals basis, 60nm).

The SnI_2 solution was prepared by dissolving SnI_2 in DMF with a concentration of 1.5 mol L^{-1}. Commercial TiO_2 nanoparticle colloid was diluted with ethanol (1:6.5 w/w) and then placed in an ultrasonic bath for 8 h.

4.2.2 Measurements

The crystal structures of the perovskite films were investigated by using an X-ray diffractometer (Rigaku SmartLab 9kW). Film morphology and EDS mapping of the perovskite layer were observed using a Scanning Electron Microscope SEM (JOEL 6490, USA). The current– voltage tests of devices were conducted on a Keithley Model 2400 with an AM 1.5 solar simulator (Enli Technology Company). The light intensity measured by the device was 100 mW cm^{-2}, and the silicon solar cell used for calibration. The effective testing area of the cells is defined as the project area A, which is equal to the diameter of the photoanode multiplied by its length (5 cm). The transmittance of thin platinum layer determined via UV-visible meter, and at a wavelength of 650 nm. Surface resistance as measured using resistivity measuring devices using the four-probe array technique.

4.2.3 Synthesis of vanillin-doped 2D3D perovskite material

Figure 4.0 illustrates the molecular structures of vanillin and vanillic acid, highlighting the oxygen radical scavenging hydroxyl benzene group, the carbonyl group (-C-O-H), and the alkoxyl group (-O-CH_3). In order to assess the efficacy of vanillin as an antioxidant additive in perovskite, we chose to investigate its effects on Sn-based 2D3D hybrid perovskite material. The synthesis procedure for this perovskite material, involving the reaction of 2D and 3D perovskite molecules with chloride ions as catalysts to achieve tin-based 2D3D hybrid perovskite, has been previously reported in our work referenced as.[22] The procedure, summarized in equations 4.1, involved the mixing of methylammonium iodide (CH_3NH_3I, MAI), aminovaleric acid iodide ($HOOC(CH_2)_4NH_3I$, AVI), and tin iodide (SnI_2) in DMF solvent to create a solution containing a mixture of iodine-based 2D and 3D perovskite molecules. For each sample, the MAI to SnI_2 ratio was maintained at 1:1, with AVI added at a proportion of 3%. $SnCl_2$ was then added to the

mixture in a mass ratio of 1:1 to SnI_2. The resulting mixture was heated to 100oC for 5 minutes under magnetic agitation.[22]

$$AVI + MAI + SnI_2 \xrightarrow[(100^oC,\ 5min)]{SnCl_2} 2D3D\ Perovskite\ solution \ldots\ldots\ldots\ldots Eq(4.1)$$

$$2D3D\ Perovskite\ solution + Vanillin \rightarrow 2D3D\cdots\cdots Vanillin \ldots\ldots Eq(4.2)$$

The 2D3D hybrid solution was prepared and then doped with various mass percentages of vanillin (0%, 2.5%, 7.5%, 10%, 12.5%, and 15%) to create perovskite-vanillin composite solutions, as shown in equation 4.2. The mixture was then stirred magnetically at 60°C for 10 minutes.

4.2.4 Characterization of vanillin-doped 2D3D perovskite material

The color changes over time for the perovskite precursor solutions doped with 0%, 2.5%, and 7.5% vanillin provide visual evidence of the effect of vanillin on 2D3D hybrid perovskite. Initially, all the solutions had a pale-yellow color at 0 hours, as shown in Figure 4.1(a). After 500 hours of exposure to air, 65% relative humidity, and room light, the 0% solution (without vanillin) turned dark brown/black. The 2.5% vanillin-doped sample turned brown, while the 7.5% solution remained essentially unchanged, as shown in Figure 4.1(b). This color change phenomenon is tentatively attributed to the oxidation of Sn^{2+} to Sn^{4+}, indicating the susceptibility of Sn perovskites to oxygen. The comparison clearly shows that vanillin can inhibit the oxidation of Sn^{2+} in the precursor solution.

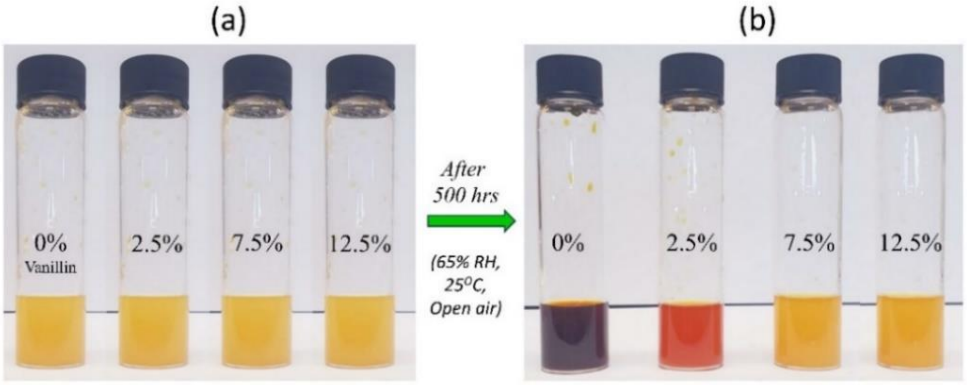

Figure 4.1 a-b) Photographs of vanillin-doped Sn-based perovskite solutions; a) Initially (0 hours). b) after 500 hours of aging.

According to Figure 4.2(a), the UV-vis absorption capacity of vanillin-doped Sn-based perovskite samples decreases as the vanillin doping increases, particularly in the wavelength range of 500 to 850 nm. Reflectance analysis in Figure 4.2(b) shows that the reflectance of the perovskite films increases with higher vanillin doping.

The observed trend in UV-vis absorption could be explained by the fact that the average density of vanillin is approximately 1.06 g/cm^3,[23] while the density of perovskite is around 4.29 g/cm^3.[24] As a result, excess vanillin molecules are likely to float on top of the perovskite film and form a continuous or discontinuous vanillin film. This is verified by SEM images in Figure 4.2(c-j) and illustrated in Figure S6 (Appendix). When light interacts with the vanillin thin film on top of the perovskite layer, three possible scenarios can occur: absorption, reflection, or transmission. However, the transmittance spectrum in Figure S7 (Appendix) of the pure vanillin film on a glass slide shows high transmittance in the wavelength range of 500 to 850 nm, indicating that vanillin has low absorbance in this range. Therefore, this confirms that the reflectance effect is caused by the thin vanillin layer formed on the perovskite surface at high vanillin doping percentages.

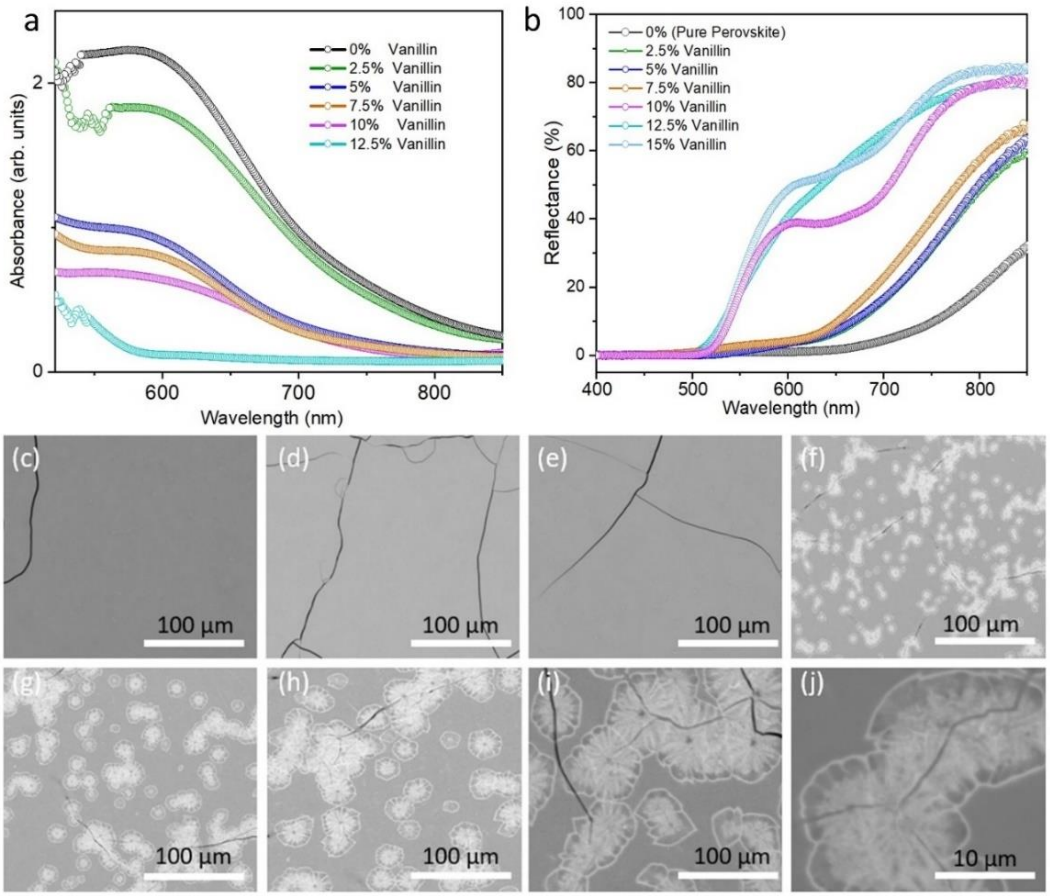

Figure 4.2 a-b) UV–vis absorption spectra and reflectance spectra respectively, all measured at 0 hours for vanillin-doped perovskite films. c-j) Surface SEM images of perovskite samples doped with 0%, 2.5, 5% 7.5%, 10%, 12.5% and 15% vanillin, respectively. h) Magnified portion with vanillin thin film on perovskite.

The changes in UV-vis absorbance of the vanillin-doped samples at a wavelength of 650 nm after 120 hours of exposure to air, 65% RH, and room light were analyzed and summarized in Figure 4.3 and Figure S8 (Appendix). Figure 4.3(a-b) shows that the absorbance of the undoped sample decreased by -58.7%, while the 7.5% vanillin-doped sample exhibited the highest percentage increase in absorbance (about +75%) after 120 hours. Figure 4c presents a bar graph summarizing the absorbance data for perovskite films with different levels of vanillin doping after 120 hours. The outstanding increase in absorbance at 7.5% vanillin doping in perovskite films after 120 hours of storage is attributed to the following reasons;

1. At this percentage, the amount of vanillin molecules could be just enough to effectively bring about the required saturation of vanillin within the bulk of perovskite material, for maximum redox reaction interactions with perovskite molecules.
2. Since at this percentage the molecules are just enough, less vanillin is available to float and form reflective films on the surface of perovskite, as witnessed in the SEM images in Figure 4.2, hence the observed increase in absorbance.

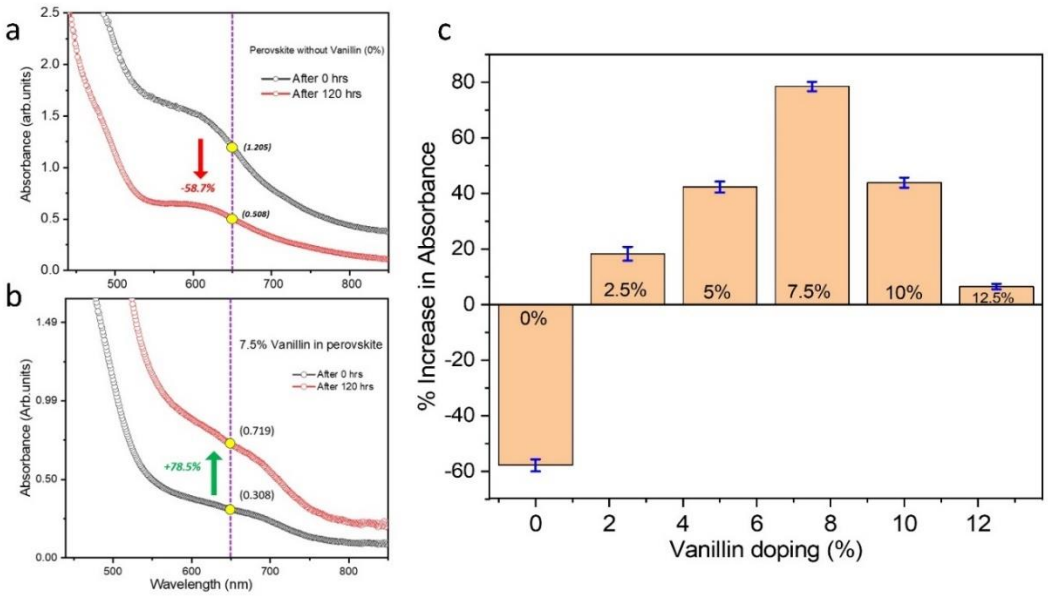

Figure 4.3. UV-vis absorption spectra after 120 hours; a) Showing a decrease in absorbance for the undoped perovskite film. b) Increase in absorbance for the 7.5% vanillin-doped perovskite film. c) A bar graph showing the percentage increase/decrease in absorbance after 120 hours of film exposure, for perovskite films with different vanillin doping percentages.

The energy-dispersive X-ray spectroscopy (EDS) characterization of the surfaces of vanillin-doped films showed that the composition of Sn atoms on the surface decreased, while the composition of oxygen atoms increased with increasing vanillin doping. This is shown in Figures S9 (Appendix). The increase in oxygen atoms on the perovskite surface with increasing vanillin doping is attributed to the oxygen atoms present in the ether, aldehyde, and hydroxyl groups of the vanillin molecules that form films on top of the perovskite. The percentage of Sn atoms

decreases with increasing vanillin doping because at high vanillin percentages, the antioxidant forms surface films and covers the perovskite surface.

The increase in UV-vis absorbance observed in the 7.5% vanillin-doped perovskite films was further investigated beyond 120 hours. The results are presented in Figure 4.4(a) (and its inset table). The findings show that after approximately 336 hours of exposure to ambient conditions, the absorbance of the 7.5% vanillin-doped sample increased by approximately 122.7% compared to its initial absorbance, reaching its peak absorbance. After a cumulative exposure of 500 hours, the sample's absorbance was found to be 19.75% higher than its initial absorbance. Further exposure to 668 hours resulted in a decrease in absorbance to -25.3% of the initial value, indicating the start of the material's degradation process. The increase in perovskite material absorbance over the course of 336 hours is attributed to the healing of crystal defects through coordinate and electrostatic interactions between vanillin and perovskite, as well as the continuous reduction of Sn^{4+} to Sn^{2+}. After 336 hours, the UV-vis absorption capacity gradually decreases due to the gradual depletion of the antioxidants as vanillin continues to oxidize to vanillic acid, and vanillic acid further oxidizes to dioxobenzoic acid, a final non-antioxidant product.

On the other hand, as shown in Figure 4.4(b), the undoped (0% vanillin-doped) sample exhibited a significant decrease in absorbance of -57.1% compared to its original value after the same duration of exposure. After an additional 500 hours of exposure, the absorbance of the control film decreased by -79.4%. The decrease in the absorption capacity of the control film is attributed to the continuous oxidation of Sn^{2+} to Sn^{4+}, resulting in the loss of the material's molecular structure. Previous studies by other researchers have shown that the oxidation of vanillin in a redox reaction leads to the formation of vanillic acid. Additionally, the moderate antioxidant activity of vanillic acid has been confirmed.[25] The average thickness of the spin-coated perovskite-vanillin thin films was estimated to be approximately 850 nm, coated on pure quartz glass with a thickness of 1mm. The prepared perovskite thin films were stored in open air, room light, at room temperature (25ºC), and an average relative humidity of 65%.

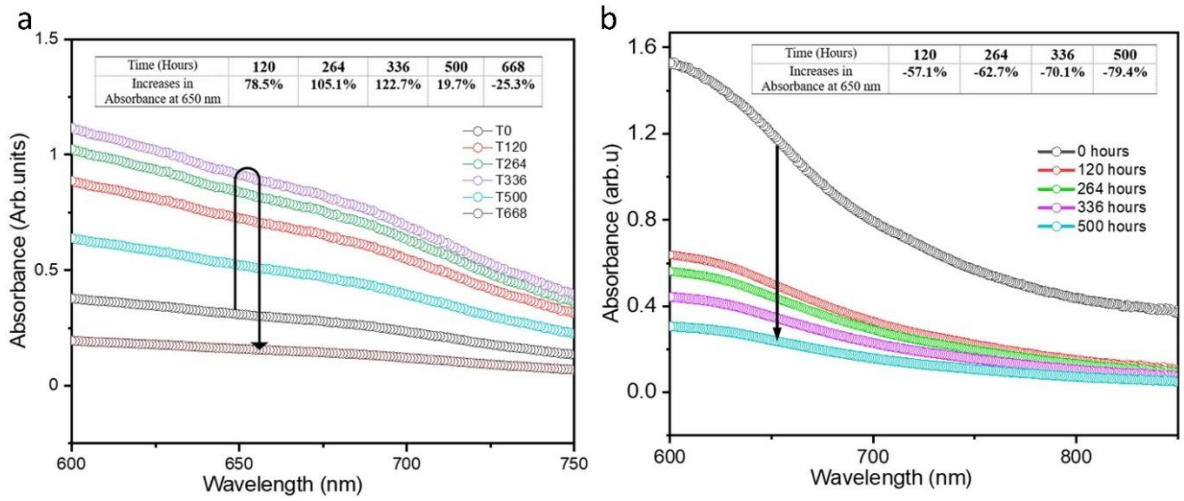

Figure 4.4. Variation of UV-vis absorption capacity with time (beyond 120 hours of perovskite material aging) a) 7.5% vanillin-doped perovskite b) Undoped perovskite, at 650 nm wavelength.

In this study, we investigated the effectiveness of vanillic acid, a byproduct of vanillin oxidation, in slowing down the oxidation of Sn-based perovskite. We also examined its ability to enhance the material's stability and performance. In Figure S10 (Appendix), we observe that the absorbance increases to a maximum of 86.7% of the initial value after 336 hours when the perovskite material is doped with 7.5% vanillic acid. However, after 500 hours of exposure to 35% humidity, room light, and air, the sample's absorbance decreases by -30.2% from its initial value. This decrease indicates that the material has partially degraded due to oxidation. We believe that the depletion of vanillic acid in perovskite had begun at the point of degradation, exposing Sn^{2+} to oxygen. Oxygen is highly detrimental to Sn-based perovskites because it readily oxidizes Sn^{2+} to Sn^{4+} upon contact with air. This oxidation causes perovskite to break down from a three-dimensional ($ASnX_3$) material to a zero-dimensional (0D) form, resulting in a significant loss of the material's UV-vis absorption capability.

Figure 4.5(a-b) shows the X-ray Photoelectron Spectroscopy (XPS) spectra of the Sn 3d bands of the perovskite films, both without and with vanillin. This technique helped us determine the surface compositions of the films and study their chemical states. When the control samples (0% vanillin-doped) were exposed to air during film preparation, handling, and characterization, oxidation was easily observed on the film surfaces. The area ratio of 3:2 ($d_{5/2}$: $d_{3/2}$) is indicated by the fitting of Sn 3d doublets, which is due to the degenerate spin states. The deconvolution of

the XPS data shows four main peaks: 487.2 and 495.8 eV for the Sn^{4+} charge states, and 486.5 and 495.0 eV for the Sn^{2+} charge states. To evaluate the effect of vanillin in suppressing Sn^{2+} oxidation, we estimated the area ratio of Sn^{4+}/Sn^{2+}, which decreased from approximately 58.6% (0% vanillin-doped perovskite) to about 4.85% (with 7.5% vanillin-doped perovskite) on the surface. This confirms that vanillin effectively retards Sn^{2+} oxidation due to its antioxidant activity. After being exposed to air, moisture, and a relative humidity of about 35% for 264 hours, the surface composition of both doped and non-doped perovskite samples indicates that vanillin significantly reduces Sn^{4+} back to Sn^{2+} and maintains the material's stability.

To investigate the impact of Vanillin doping in the Sn-perovskite on reducing nonradiative recombination and improving the lifetime of charge carriers in the device, both steady-state and time-resolved PL spectroscopy were conducted and presented in Figure 4.5(c-d). The results shown in Figure 4.5(c) indicate that the exciton intensity increases as the vanillin content increases, reaching a maximum at 7.5% vanillin doping, but decreases beyond that point. The highest intensity of excited charge carriers is observed at 7.5% vanillin doping, followed by 2.5% and 12.5%, with the lowest intensity at 0%. The PL intensity of the perovskite film doped with 7.5% vanillin increased by approximately 258% compared to that of the control sample. This increase is attributed to the improved suppression of trap-assisted nonradiative recombination of charge carriers. The addition of vanillin also resulted in a narrower full width at half maximum (FWHM), indicating a reduction in deep-level defect states within the bulk perovskite layer and an improvement in perovskite crystallinity.

Similarly, in Figure 4.6(d), it can be seen that the charge carrier lifetime of the samples increases from 19 ns for the control sample to 28 ns for the 2.5% vanillin-doped sample, and further increases to 46 ns for the 7.5% vanillin-doped sample, as indicated in Table S3 (Appendix). The reason for this increase in charge carrier lifetime with higher levels of vanillin doping is the result of the coordinated and electrostatic interactions between vanillin and perovskite molecules. These molecular interactions facilitate the slow yet successful crystallization of the perovskite, leading to improved crystal quality and a reduction in crystal defects. Consequently, with better crystallization and higher crystal quality, charge carriers are able to be generated and dispersed with minimal recombination. However, it should be noted that at higher percentages (12.5%), vanillin, being nonconductive, tends to hinder the continuous flow of charge carriers. Moreover,

excessive amounts of vanillin also tend to form a surface coating on the perovskite crystals, which increases their reflectivity to incident light and consequently leads to a decrease in exciton intensity. As an additive, vanillin serves as an antioxidant in perovskite, preventing the oxidation of Sn^{2+} and aiding in the reduction of Sn^{4+} back to Sn^{2+}.

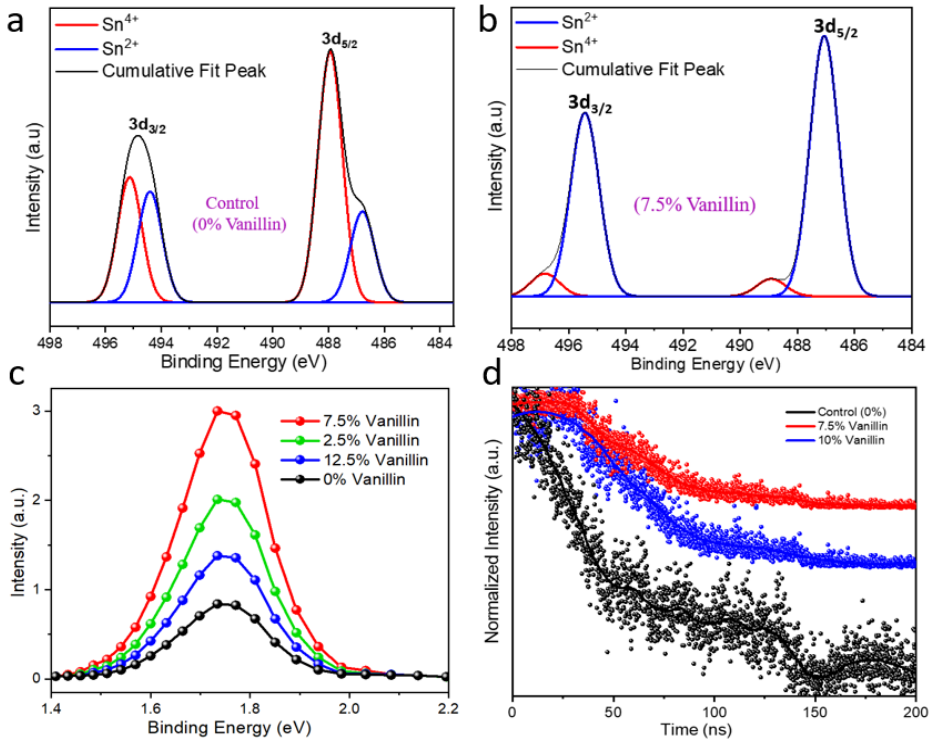

Figure 4.5. a-b, XPS spectra of films without and with 7.5% Vanillin addition. c-d) Steady-state PL and Time-resolved photoluminescence (TRPL) spectra of the perovskite films.

To gain a better understanding of the interaction between perovskite and vanillin, we conducted Raman characterizations of vanillin, Sn-based 2D3D perovskite, and vanillin-2D3D perovskite samples. Figure 4.6(a) shows that the peak shift from 113 to 121 cm^{-1}, and 153 to 148 cm^{-1} indicates molecular interaction between perovskite and vanillin. This interaction specifically occurs between Sn^{2+} and the electron-rich groups on vanillin. Additionally, the peak shift from 237 to 240 cm^{-1} reveals the interaction between $(CH_3NH_3)_n^+$ and the electron-rich groups on vanillin. Furthermore, the presence of the vanillin-related peak at 425 cm^{-1} in perovskite-vanillin suggests that vanillin is incorporated into the bulk perovskite films, rather than being surface absorbed. This is because the Raman signals from the surface would be too weak to be detected by normal Raman measurements.

We used XRD to examine the changes in crystallinity with increasing vanillin doping. Figure 4.6(b) displays the XRD patterns for 2D3D perovskite samples doped with 0%, 2.5%, 7.5%, and 10% vanillin as an additive. Close analysis of the XRD spectra reveals that the intensity of the most prominent perovskite peak at 14.7^{o} increases from 19.0 to 59.8 to 185.4 and finally to 48.5 arbitrary units, corresponding to 0%, 2.5%, 7.5%, and 10% vanillin doping percentages in the perovskite material. Similarly, the full width at half maximum (FWHM) of the peak at 14.7o continuously decreases with increasing vanillin doping, reaching its lowest value at 7.5% before increasing again. This consistent increase in peak intensity and decrease in FWHM with increasing vanillin doping can be attributed to improved crystal quality. This improvement arises from enhanced nucleation and crystallization, facilitated by electrostatic and coordinate interactions between vanillin and perovskite molecules. Additionally, the SEM images in Figure S11 (Appendix) further demonstrate the gradual enhancement in crystal size and quality up to a maximum doping percentage of 7.5%. At higher doping levels, the SEM crystal images become difficult to discern due to the formation of a vanillin film on top of the perovskite.

The perovskite identifier peak, which corresponds to the (110) direction of the tetragonal phase, is observed at ∼14.7°. In the parallel orientation, all the (0k0) planes are visible (where k is an even number), and in the perpendicular orientation, the (011), (202), and (213) planes are generally visible. However, we observed changes in the lattice measurements with increasing vanillin doping, as indicated by the slight shift in peak positions. For instance, the position of the (202) peak shifted from 22.2^{o} with 0% vanillin to 25.9^{o} with 2.5%, 26.3^{o} with 7.5%, and finally 26.7^{o} with 10% vanillin doping. These changes in the crystal lattice can be attributed to increased molecular distortion resulting from augmented coordinate and electrostatic interactions between perovskite and vanillin molecules.

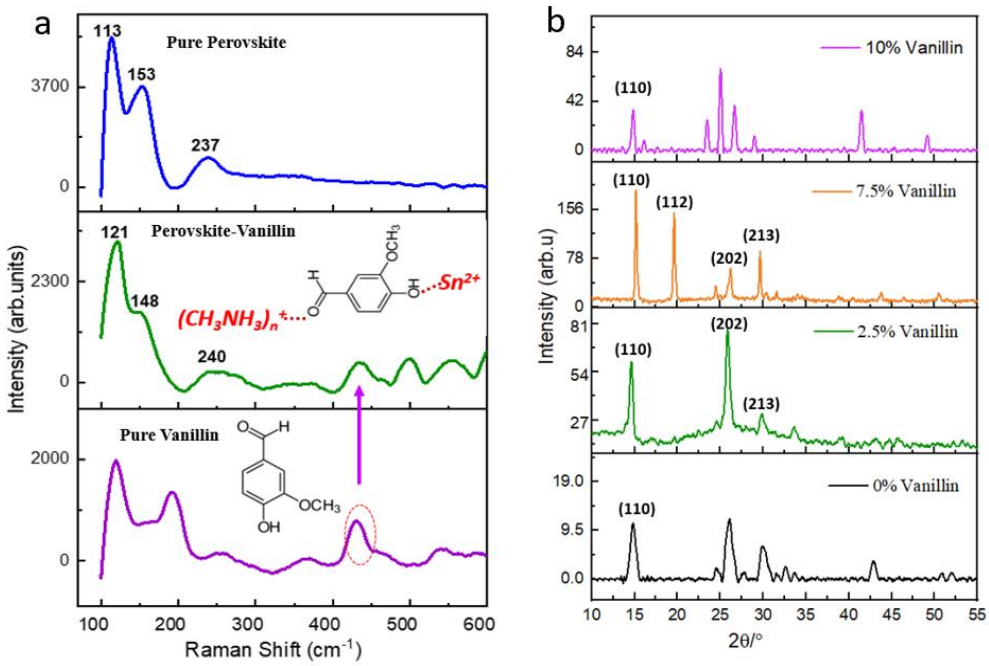

Figure 4.6 a) Raman spectra of pure Sn-based 2D3D perovskite film, perovskite-vanillin composite film, and pure vanillin film. b) XRD spectra with increasing levels of vanillin doping in perovskite.

4.3 Solar cell fabrication and characterization

To assess how the addition of vanillin affects the performance and stability of Sn-based perovskite materials in solar cells, we conducted a series of photovoltaic experiments using a flexible one-dimensional fiber-type assembly. The structure of the device is illustrated in Figure 4.8(a) and consists of PEN-film/ITO/TiO_2/Perovskite-vanillin/PEDOT:PSS/Thin platinum electrode. The flexible perovskite solar cell (FPSC) is built on a polyethylene naphthalate/indium tin oxide (PEN/ITO) strip. Before use, the strip is treated with 2 M HCl, followed by cleaning with water and ethanol. Polyethylene naphthalate possesses desirable properties, such as high tensile strength, minimal heat shrinkage, excellent dimensional stability, low moisture absorption, and good physical property retention within a wide temperature range. Its tensile strength, hydrolytic stability, and oxygen barrier performance surpass that of PET films.

The ITO layer acts as the internal electrode for electron collection from the Titanium oxide layer. The mesoporous TiO_2 layer, as shown in Figure S12 (Appendix), is deposited through dip-coating using a 400 mg ml-1 TiO_2 paste solution in ethanol. The coated layer is then annealed at

80oC for 40 minutes. To create the mesoporous TiO_2 layer, commercial TiO_2 nanoparticles (diameter: 60 nm) paste is diluted with ethanol (1:3 w/w) and deposited accordingly. This layer increases the surface area for electron extraction and serves as a barrier for holes, reducing electron-hole recombination in the device. It also aids in generating the necessary electric field force to direct electrons and holes towards their respective electrodes. The vanillin-doped perovskite solution, with a concentration of 100 mg mL^{-1}, is then spin-coated onto the mesoporous TiO_2 layer and dried at 80^oC.

Once the perovskite layer is deposited, a nanofiber layer of PEDOT:PSS is electrospun on top. This layer functions as the hole transport or electron-blocking layer in the device structure. To enhance its electrospinnability, PEDOT:PSS is mixed with a carrier polymer, Polyvinylpyrrolidone (PVP), in a ratio of 3.25/0.015 g, respectively. The blend is dissolved in 0.55 g of DMF solvent and electrospun at a rate of 0.4 ml/hr. The electrospinning process maintains a needle tip-to-substrate separation distance of 15 cm and an electrospinning voltage of 27 kV. The nanofiber layer of PEDOT:PSS should fulfill two crucial criteria: high transmittance and conductivity. Based on our previous research, we determined that a 15-minute electrospun nanofiber layer meets these requirements optimally. This layer exhibits a resistance of approximately 7.56 kOhm and a transmittance greater than 70% within the wavelength range of 350-850 nm. PEDOT:PSS, as the hole transport layer material, offers several cutting-edge advantages, such as high conductivity, excellent thermal stability, high transparency in the visible range, exceptional flexibility and stretchability, and a broad oxidation potential window of 1.2-1.5V.[26]

Magnetron sputtering was used to create a thin film of platinum nanoparticles as the top electrode. This method was chosen for its ease of industrialization and its safety for the underlying layers. Figure S13a (Appendix) shows the transmittance of platinum thin films created with different sputtering durations. Figure S13b (Appendix) presents the relationship between surface resistance and transmittance of the sputtered thin platinum layer. As the magnetron sputtering duration increased from 15 s to 55 s, the surface resistance of the platinum thin films decreased from 68.9 Ω/cm^2 to 10.8 Ω/cm^2, while the transmittance of the thin platinum layers decreased from 84.04% to 58.55% at a wavelength of 650 nm. The optimal sputtering time was determined to be 35s, with a transmittance of approximately 72.9% and a surface resistance

of 20.5 Ω/cm^2. This condition was considered the best balance between transmittance and conductivity for the top platinum thin electrodes.

Figure 4.7(a) illustrates the solar cell design used during device assembly. Several solar devices with varying percentages of vanillin doping in the photoactive layers were fabricated and examined to evaluate the effect of vanillin doping in the Sn perovskite material on the photovoltaic performance of the solar cell. Table 4.1 outlines the best photovoltaic characteristics, and Figure 4.7(b) displays the typical J-V curve of the best-performing PSCs, obtained by doping the photoactive layer with 7.5% vanillin. All tests were conducted at an air mass of 1.5 G under 1 sun (1000 Wm^{-2}) solar illumination. The surface area of PEN/ITO/Sn-Perovskite-Vanillin/PEDOT: PSS yarn was estimated to be approximately 200 mm^2 (4 x 50 mm), with a projected photoactive area of the solar cell of approximately 125 mm^2. All devices were fabricated with consistent film thicknesses ($TiO_2 \approx 400$ nm, Perovskite-Vanillin ≈ 850 nm).

As shown in Figure 4.7(b) and Table 4.1, increasing the vanillin doping percentage in the perovskite material significantly improves the PCE, short circuit current (JSC), open circuit voltage (Voc), and fill factor up to a maximum doping level of 7.5%. Beyond this level, the photovoltaic performance starts to decrease. The PCE values increased from 9.6% for the control device to a maximum of 13.18% at 7.5% vanillin doping. The champion device also exhibited the highest Voc of 1.01 V, Jsc of 22.08 mAcm^{-2}, and a fill factor of 75.3%. To the best of our knowledge, 13.18% is the highest reported PCE in one-dimensional flexible Sn-based perovskite solar cells. The gradual improvement in solar cell performance with increasing vanillin doping is attributed to the corresponding enhancement in crystal quality, reduction in crystal defects, and increased charge carrier lifetime. Vanillin, as an antioxidant, reduces Sn^{4+} to Sn^{2+} and restores and maintains the quality of the perovskite materials. However, at high vanillin doping levels, the solar cell performance decreases because vanillin is a non-conductor.

Table 4.1. Detailed photovoltaic parameters of the champion PSCs without and with Vanillin. (For 15 samples from each category)

Vanillin (%)		V_{oc} (V)	Fill factor (FF) (%)	J_{SC} (mA.cm^{-2})	PCE (%)
0	Highest	0.93	68.4	15.97	9.60
	Average	0.88 ± 0.15	67.4 ± 0.3	15.4 ± 0.4	9.1 ± 0.2
2.5	Highest	0.98	71.4	19.20	12.70
	Average	0.92 ± 0.21	70.6 ± 0.25	18.8 ± 0.23	12.2 ± 0.1
7.5	Highest	1.01	75.3	22.08	**13.18**
	Average	0.99 ± 0.01	74.6 ± 0.32	21.7 ± 0.22	12.95 ± 0.11
10	Highest	0.95	70.2	18.31	10.90
	Average	0.89 ± 0.05	68.3 ± 0.42	17.4 ± 0.12	9.36 ± 0.43
12.5	Highest	0.84	63.3	13.50	7.70
	Average	0.76 ± 0.07	61.2 ± 0.12	12.4 ± 0.23	6.81 ± 0.17

The average temperature at the South Pole of the Earth during the polar day is approximately -40°C, while the highest daytime temperature on the moon reaches around 127°C. A wearable solar cell needs to be able to withstand a wide range of temperatures, from fluctuations in winter to extreme heat in the summer. To test the stability of the photovoltaic devices against varying temperatures, they were stored at different temperatures for 15 minutes before testing, without any encapsulation. The normalized power conversion efficiencies (PCEs) were recorded at both temperature extremes (-47°C and 110°C), and they were found to be over 90%, as shown in Figure 7c. This indicates that the flexible perovskite solar cells (FPSCs) operated stably within this temperature range. The overall thermal stability of the solar cell is attributed to the use of a thermally stable 2D3D hybrid perovskite material. However, the normalized PCE declined below 10°C and above 90°C due to the contraction and expansion of the metallic electrodes and other layers, which affected the interfaces and charge flow properties. Additionally, high temperatures beyond the glass transition of PEDOT: PSS nanofibers negatively impacted their hole transport capabilities.

One challenge faced by FPSCs is the potential for film rupture when they are bent or twisted, which could hinder the transmission of charge carriers and lead to a decrease in the open circuit voltage (Voc) and short-circuit current density (Jsc). Figure 4.7(d) demonstrates that the FPSC maintained around 90% of its original PCE after 500 bending cycles. The slight reduction in PCE can be attributed to the rupture of layers during the bending process. However, the observed relative bending stability is due to the increased flexibility of certain layers, such as the PEDOT: PSS nanofiber layer and PEN polymer substrate. On the other hand, the bending process tightens the contacts between the layers, resulting in a slight increase in the fill factor after 500 cycles of bending, as shown in Figure 4.7(e). Nevertheless, other photovoltaic variables, including Voc and Jsc, slightly decreased (as shown in Figure S14(a-b)-Appendix) due to perovskite film rupture and damage to other layers caused by bending and flexing of the device.

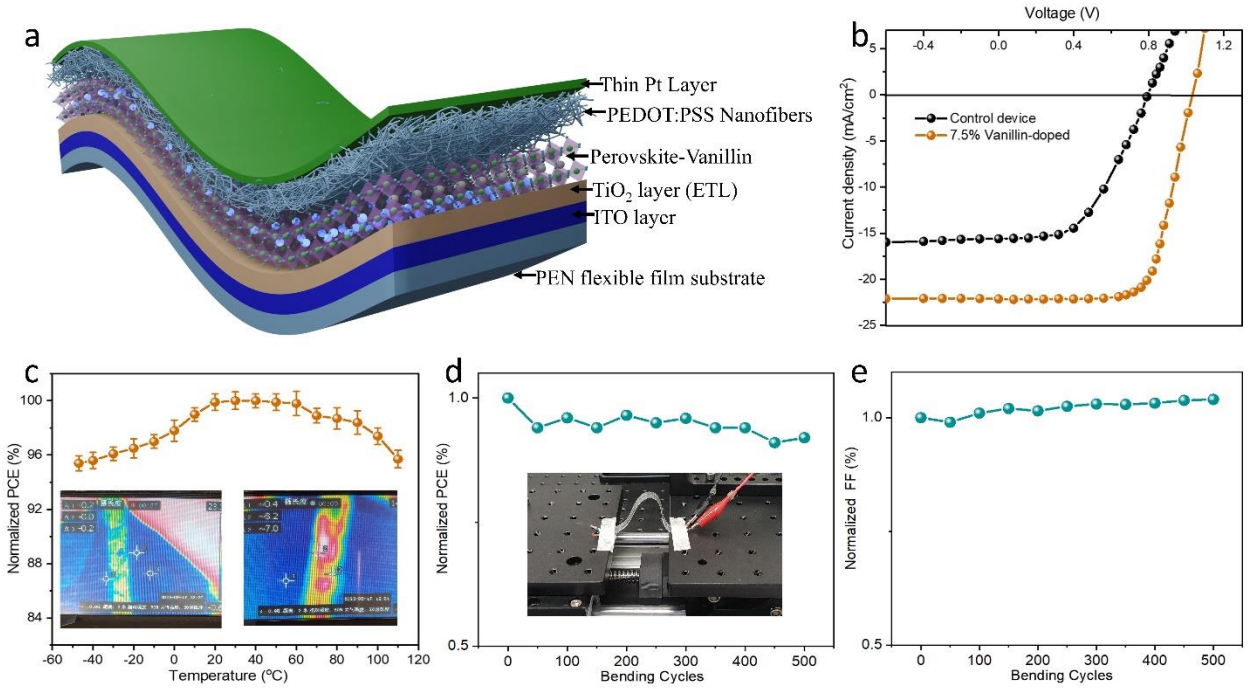

Figure 4.7 a) Schematic representation of the flexible perovskite solar cell; b) IV test results for the 7.5% vanillin-doped highest performance devices; c) Variation of normalized PCE with storage temperature. Inset; thermal camera images of the solar cells taken immediately after withdrawing from extreme cold chamber. d-e) Variation of PCE and fill factor over 500 consecutive bending cycles.

Figure 4.8(a) shows the external quantum efficiency (EQE) of the control device and the 7.5% vanillin-doped device. Both devices demonstrate a strong optical response across a wide range of wavelengths, from near-infrared to ultraviolet. Particularly, in the long wavelength range of >450 to ~700 nm, the EQE response of the vanillin-doped device is increased. This can be attributed to a lower charge recombination rate and decreased defect state density, resulting in a more efficient collection of photogenerated electrons. The integrated current densities determined from the EQE spectra are 22.07 and 15.97 $mA.cm^{-2}$ for the vanillin-doped device and the control device, respectively.

Figure 4.8(b) illustrates the variation of normalized power conversion efficiency (PCE) with storage time under specific conditions. The data shows that during the first 348 hours, the normalized PCE of the 7.5% vanillin-doped device gradually improves by approximately 4.1%. After this time, the normalized PCE returns to its initial value. After 812 and 2200 hours of aging, the normalized PCE of the vanillin-doped device decreases to about 88% and 35.7%, respectively. In comparison, the normalized PCE of the undoped device decreases drastically to around 40% and 19% after 812 and 2200 hours, respectively. The prolonged stability of the vanillin-doped device is attributed to the double staged redox reaction of vanillin. The initial increase in normalized PCE is due to the gradual improvement in the quality of the perovskite material and the reduction of Sn^{4+} to Sn^{2+}, as well as the healing of internal defects.

The carrier dynamics in PSCs were studied using electrochemical impedance spectroscopy (EIS) measurements. Nyquist plots of the vanillin-doped and control devices, as shown in Figure 4.8(b), represent a dielectric polarization in the bulk perovskite. From these plots, the high-frequency series resistance (Rs) and the low-frequency recombination resistance (Rrec) can be determined. Table S4 in the Appendix provides the equivalent values. Since the recombination rate is inversely proportional to Rrec, it can be concluded that the device with vanillin additive exhibits a lower recombination rate compared to the reference device.

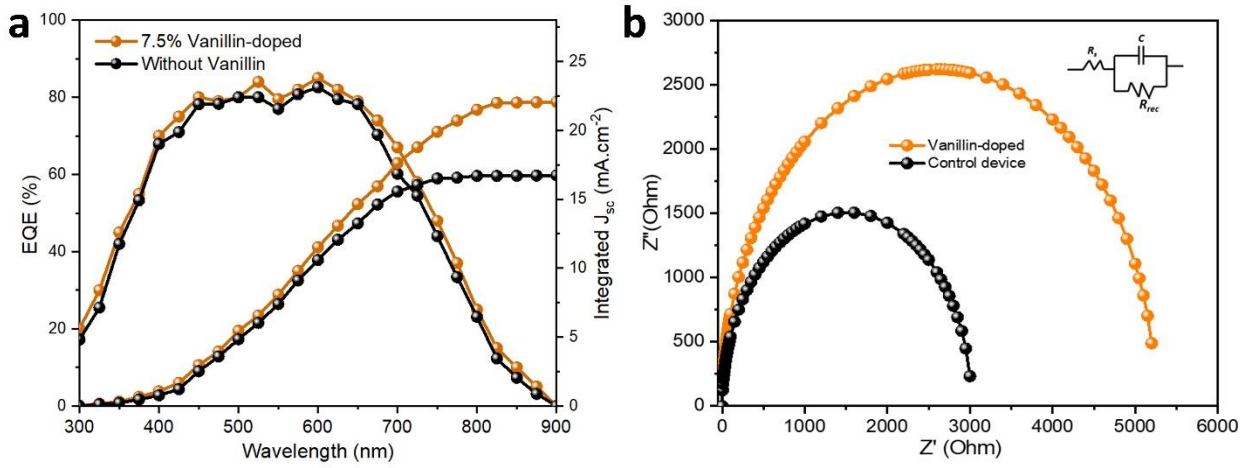

Figure 4.8. a) External quantum efficiency (EQE) spectra and the integrated current density curve. b) EIS of vanillin-doped and the perovskite solar cells (inset: equivalent circuit for fitting the plots)

4.4 Microwave irradiation of aging solar cells

The main challenge faced by perovskite solar cells today is the decrease in efficiency over time, which shortens their lifespan and requires frequent expensive recycling. In this study, we propose using microwave irradiation to rejuvenate aging perovskite solar cells, providing a low-cost and non-destructive method to recover some of their initial efficiency without the need for recycling. The solar cells were subjected to microwave radiation at a power of 160 watts for a duration of 3 minutes. Initial trials, as shown in Table S5 (Appendix), indicate that increasing the microwave irradiation time from 0 to 3 minutes improves the efficiency recovery percentage, with the maximum recovery achieved at 3 minutes. However, beyond 3 to 5 minutes, the efficiency recovery percentage gradually decreases, and after 6 minutes, the solar cells fail.

To determine the extent of efficiency recovery for solar cells after different aging periods, we used the optimal exposure time of 3 minutes with 160 W of microwave irradiation. Solar cells doped with 7.5% vanillin and exposed to microwave radiation showed a recovery of up to 96.5% and 65.4% in normalized power conversion efficiency (PCE) after 812 and 2200 hours of aging, respectively. In contrast, without microwave irradiation, the vanillin-doped solar cell exhibited 88% and 35.7% normalized PCE after the same aging periods. Microwave irradiation of undoped

solar cells resulted in a 30.1% recovery in normalized efficiency after 2200 hours of aging, as shown in Figure 4.9.

Microwave treatment has both thermal and non-thermal effects. Recent studies have shown that microwave heat promotes the crystallization and recrystallization of perovskites, as well as the evaporation of water molecules.[27] This recrystallization was further confirmed by X-ray diffraction analysis (Figure S15, Appendix). Microwave radiation also enhances the interaction between oxidized Sn^{4+} and antioxidant vanillin molecules, increasing the reduction activity of Sn^{4+} to Sn^{2+} and leading to the observed recovery in PCE. This process is summarized in the schematic illustration in Figure S16 (Appendix). The decomposition of perovskite is a reversible reaction under favorable conditions, and the byproducts are contained within the reaction environment. In our opinion, vanillin serves a dual role. Firstly, it acts as a medium to contain the degradation byproducts of various perovskites. Additionally, it facilitates the transfer of microwave heat, promoting perovskite re-crystallization.[28]

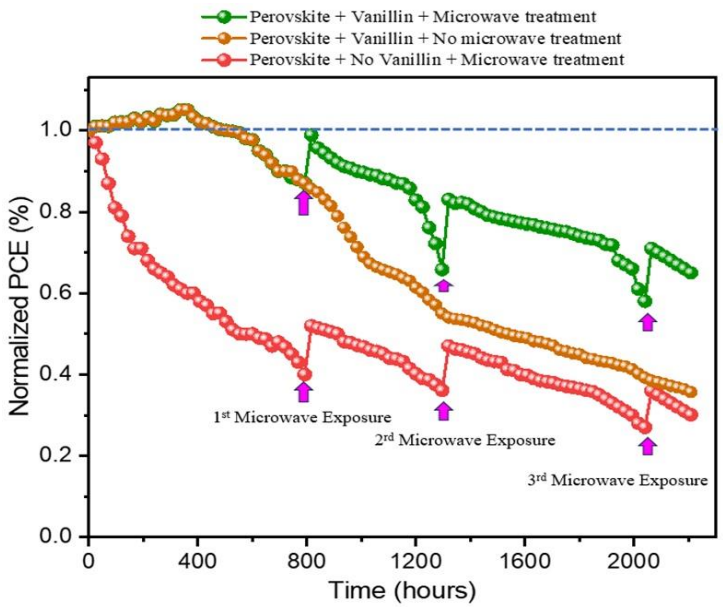

Figure 4.9. Variation of normalized PCE with time and microwave irradiation, under high relative humidity (>70%) and open-air conditions.

4.5 Key research findings and outputs in chapter four.

In this work package, the following were the key outputs and achievements, in line with the set objectives of our study.

1. The coordinate and electrostatic interactions between vanillin and perovskite to induced better crystallization of perovskite (according to the SEM images and XRD), and resulted in power conversion efficiency enhancement, to a champion PCE of 13.18% using a flexible one-dimensional solar cell architecture.
2. The flexible PEN polymer substrate, the incorporation of a nanofiber layer of PEDOT:PSS (HTL) and the 1D fiber-type perovskite solar cell structure enabled increased bending stability after > 500 bending cycles, and suitability of the solar cells for weaving applications.
3. Unlike in other reports about antioxidation of Sn-based perovskites using antioxidants such as caffeic acid and others, in this study, we revealed the prolonged antioxidation capability of vanillin (demonstrated by the XPS analysis) due to its ability to undergo two reduction reactions in succession. This therefore resulted in prolonged inhibition in the oxidation of Sn^{2+} to Sn^{4+}, hence preventing rapid material degradation under open air conditions.
4. As a pioneer study, we introduced the use of microwave irradiation on ageing perovskite solar cells as a strategy for recovering the lost efficiency due to material degradation. With this approach, we recovered the normalized efficiency of the solar cell from 88% to 96.5% after 812 hours, and from 35.7% to 65.4% after approximately 2200 hours of aging (in light, relative humidity >75% and open-air conditions).

4.6 Conclusion

In summary, we proposed a combined approach using antioxidant vanillin and microwave irradiation to improve the efficiency, performance, stability, and toxicity of Sn-based perovskite solar cells. Vanillin is not only a robust antioxidant with double redox reactions, but also capable of chemical interactions. In addition to suppressing the oxidation of Sn^{2+} to Sn^{4+}, vanillin also

helps to modulate perovskite film crystallization, resulting in better-quality films. When the perovskite was doped with 7.5% vanillin, the perovskite solar cell with the structure PEN/ITO/TiO_2/Perovskite-Vanillin/PEDOT: PSS/Pt achieved the highest power conversion efficiency (PCE) of 13.18%, which is the highest value among all FPSCs. The addition of vanillin reduced the trap state density and charge recombination rate by mitigating Sn2+ oxidation. Furthermore, the device reproducibility and long-term storage stability were significantly improved.

Microwave irradiation of the vanillin-doped solar cells led to the recrystallization of perovskite and a significant recovery of efficiency in aging FPSCs. This study unveils microwave treatment as a contactless and non-destructive approach to reuse perovskite solar cells, eliminating the need for frequent and expensive destructive recycling. The use of vanillin and microwave irradiation shows great potential in enhancing the efficiency and prolonging the stability of Sn-based perovskite solar cells. It also provides a foundation for further research on achieving indefinite perovskite stability using vanillin and other antioxidants.

4.6 References

1. Kajal, P., B. Verma, S.G.R. Vadaga, and S. Powar, Costing Analysis of Scalable Carbon-Based Perovskite Modules Using Bottom Up Technique. Global Challenges, 2022. **6**(2): 2100070.

2. Balilonda, A., Z. Li, Y. Fu, F. Zabihi, et al., Perovskite fiber-shaped optoelectronic devices for wearable applications. J. Mater. Chem. C, 2022. **10**(18): 6957-6991.

3. Zheng, J., M. Zhang, C.F.J. Lau, X. Deng, et al., Spin-coating free fabrication for highly efficient perovskite solar cells. %J Solar Energy Materials and Solar Cells, 2017. **168**: 165-171.

4. Li, Q., A. Balilonda, A. Ali, R. Jose, et al., Flexible solar yarns with 15.7% power conversion efficiency, based on electrospun perovskite composite nanofibers. Solar RRL, 2020. **4**(9): 2000269.

5. Cao, J. and F. Yan, Recent progress in tin-based perovskite solar cells. Energy & Environmental Science, 2021. **14**(3): 1286-1325.

6. Ren, M., X. Qian, Y. Chen, T. Wang, et al., Potential lead toxicity and leakage issues on lead halide perovskite photovoltaics. Journal of Hazardous Materials, 2022. **426**: 127848.

7. Herat, S., Contamination of solid waste from toxic materials in electronic waste (E-waste). The Journal of Solid Waste Technology Management, 2008. **34**(4): 1-18.

8. Byranvand, M.M., W. Zuo, R. Imani, M. Pazoki, et al., Tin-based halide perovskite materials: properties and applications. Chemical Science, 2022. **13**(23): 6766-6781.

9. Shockley, W. and H.J. Queisser, Detailed balance limit of efficiency of p-n junction solar cells. Int. J. Appl. Phys, 1961. **32**(3): 510-519.

10. Mahmoudi, T., W.-Y. Rho, M. Kohan, Y.H. Im, et al., Suppression of Sn2+/Sn4+ oxidation in tin-based perovskite solar cells with graphene-tin quantum dots composites in active layer. Nano Energy, 2021. **90**: 106495.

11. Lanzetta, L., T. Webb, N. Zibouche, X. Liang, et al., Degradation mechanism of hybrid tin-based perovskite solar cells and the critical role of tin (IV) iodide. Nat. Commun, 2021. **12**(1): 2853.

12. Dixit, H., B. Boro, S. Ghosh, M. Paul, et al., Assessment of lead-free tin halide perovskite solar cells using J–V hysteresis. Physica Status Solidi, 2022. **219**(11): 2100823.

13. Cao, J., Q. Tai, P. You, G. Tang, et al., Enhanced performance of tin-based perovskite solar cells induced by an ammonium hypophosphite additive. J. Mater. Chem. A, 2019. **7**(46): 26580-26585.

14. Li, W., J. Li, J. Li, J. Fan, et al., Addictive-assisted construction of all-inorganic CsSnIBr 2 mesoscopic perovskite solar cells with superior thermal stability up to 473 K. J. Mater. Chem. A, 2016. **4**(43): 17104-17110.

15. Mohammadian-Sarcheshmeh, H., M. Mazloum-Ardakani, M. Rameez, S. Shahbazi, et al., Application of a natural antioxidant as an efficient strategy to decrease the oxidation in Sn-based perovskites. Journal of Alloys Compounds, 2020. **846**: 156351.

16. Wang, T., Q. Tai, X. Guo, J. Cao, et al., Highly air-stable tin-based perovskite solar cells through grain-surface protection by gallic acid. ACS Energy Letters, 2020. **5**(6): 1741-1749.

17. Liu, H., L. Wang, R. Li, B. Shi, et al., Modulated Crystallization and Reduced V OC Deficit of Mixed Lead–Tin Perovskite Solar Cells with Antioxidant Caffeic Acid. ACS Energy Letters, 2021. **6**(8): 2907-2916.

18. Ban, H., Q. Sun, T. Zhang, H. Li, et al., Stabilization of inorganic CsPb0. 5Sn0. 5I2Br perovskite compounds by antioxidant tea polyphenol. Solar RRL, 2020. **4**(3): 1900457.

19. Tai, Q., X. Guo, G. Tang, P. You, et al., Antioxidant grain passivation for air-stable tin-based perovskite solar cells. Angew. Chem. Int. Ed, 2019. **58**(3): 806-810.

20. Christe, K.a.S., Stefan (2021, June 14). Iodine. Encyclopedia Britannica. https://www.britannica.com/science/iodine.

21. Xu, C., Z. Zhang, S. Zhang, H. Si, et al., Manipulation of perovskite crystallization kinetics via Lewis base additives. Adv. Funct. Mater, 2021. **31**(13): 2009425.

22. Balilonda, A., Z. Li, C. Luo, X. Tao, et al., Chlorine-Rich Substitution Enabled 2D3D Hybrid Perovskites for High Efficiency and Stability in Sn-Based Fiber-Shaped Perovskite Solar Cells. Adv. Fiber Mater, 2022: 1-16. Available from: https://doi.org/10.1007/s42765-022-00222-y.

23. Singh, N., T. Henningsen, E. Metz, R. Hamacher, et al., Solution growth of vanillin single crystals. Materials Letters, 1991. **12**(4): 270-275.

24. Yin, Q., Y. Wang, Q. Zhang, K. Hu, et al., Structure and properties of K 0. 5 Na 0. 5 Nb 0. 9 6 Sb 0. 0 4 O3 piezoelectric ceramics doped by CuO. Functional Materials Letters, 2021. **14**(06): 2151042.

25. Salau, V.F., O.L. Erukainure, C.U. Ibeji, T.A. Olasehinde, et al., Vanillin and vanillic acid modulate antioxidant defense system via amelioration of metabolic complications linked to Fe2+-induced brain tissues damage. Metabolic Brain Disease, 2020. **35**(5): 727-738.

26. Song, H. and K. Cai, Preparation and properties of PEDOT: PSS/Te nanorod composite films for flexible thermoelectric power generator. Energy, 2017. **125**: 519-525.

27. Liu, H., Z. Wu, H. Gao, J. Shao, et al., One-step preparation of cesium lead halide CsPbX3 (X= Cl, Br, and I) perovskite nanocrystals by microwave irradiation. ACS applied materials & interfaces, 2017. **9**(49): 42919-42927.

28. Balilonda, A., Q. Li, M. Tebyetekerwa, R. Tusiime, et al., Perovskite solar fibers: current status, issues and challenges. Adv. Fiber Mater, 2019. **1**: 101-125.

Chapter 5: Perovskite Solar Fabrics

5.1 Introduction

Textile electronics have attracted scientific and commercial interest due to their versatile capabilities, including stretchability, foldability, and potential applications in smart clothing that could revolutionize human life. The rapid progress in textile electronics has created a demand for wearable and reliable energy sources.[1] One such energy source that is abundant on sunny days is solar irradiance, which is both clean and renewable. Consequently, researchers have focused on developing solar textiles for efficient solar energy harvesting. A basic approach to creating a solar textile is to attach a solar cell to a piece of fabric. However, this combination cannot be considered a true solar textile. An alternative and more promising strategy for integrating solar cells into textiles is to either print the active elements onto the fabric or convert the fabric into a solar cell.

Fabric solar cells, also known as solar fabrics, offer several advantages over traditional flat planar solar cells[2]:

1. Flexibility: Fabric solar cells are lightweight and flexible, allowing them to be integrated into a variety of applications such as clothing, tents, backpacks, and even curtains. This flexibility makes them more versatile than rigid planar solar cells.
2. Aesthetics: Solar fabrics can be designed to be visually appealing, blending seamlessly into the surrounding environment. This makes them ideal for applications where aesthetics are important, such as in wearable technology or architectural design.
3. Portability: Fabric solar cells are easy to transport and can be rolled up or folded for storage. This portability makes them convenient for on-the-go charging of portable devices or for use in off-grid locations.
4. Durability: Fabric solar cells are more durable than traditional solar cells, as they are less prone to cracking or breaking under stress. This durability makes them suitable for use in outdoor environments or in areas with high levels of wear and tear.

5. Customization: Solar fabrics can be customized in terms of size, shape, and color, allowing for greater design flexibility and integration into different products and applications.

Overall, fabric solar cells offer a unique combination of flexibility, aesthetics, portability, durability, and customization that make them a promising technology for the future of solar energy.

In particular, solar textiles can be produced by weaving fiber-type solar cells into fabrics. However, this remains a significant challenge. Moreover, there are technological obstacles, such as the incompatibility of components with current textile industry procedures and machinery, that hinder the large-scale production of fiber-based solar textiles. The ideal wearable solar textile electronics would have properties similar to apparel, such as elasticity, foldability, and washability. This sets them apart from commercial wearable electronics. In order to function as an electrode for the solar cell, fabrics for solar cells need to exhibit excellent conductivity.[3]

5.2 Recent Progress in Perovskite Solar Fabrics

Over the past two decades, there has been significant growth in the development of methods to incorporate solar energy harvesting capabilities into textiles. Initially, attempts involved attaching rigid or flexible solar panels onto textiles, but these were only used in utilitarian apparel and futuristic fashion prototypes. They did not resemble everyday clothes in terms of their appearance, texture, and durability.[4]

In 2017, Lam et al. reported on a flexible textile-based perovskite PV laminate with a 15% power conversion efficiency (PCE). This laminate used elastomeric encapsulation to protect the fabric and active layers, and it was constructed on a SnO_2/PCBM platform. The study suggested that the encapsulating elastomer's flexibility could provide good maneuverability and the potential for washability, but experimental evidence to support these claims was not provided. The researchers also evaluated the stability of the device, finding that it maintained 70% of its initial PCE after 425 hours. Additionally, they demonstrated that the device remained functional even after being submerged in water for 35 minutes.[5]

In 2018, Jung et al. conducted research on flexible perovskite solar cells with a PCE of 5.7%. They achieved low-temperature solution processing by applying a polyurethane coating to the textile fabric. The cells were able to maintain a PCE of approximately 83% after 300 hours.[6]

Peng et al.[2] developed a fiber-shaped perovskite solar cell with an energy conversion efficiency of 3.3%. These fiber-shaped solar cells are flexible and can be woven into various structures, including self-powering textiles. In 2015, Peng et al. also created an elastic perovskite solar cell with a champion efficiency of 5.22%. These elastic PSC fibers were used in textile weaving, and the output voltage or current could be adjusted by connecting the PSC fibers in series or parallel, respectively. For example, connecting three PSC fibers in series increased the output voltage from 0.63 to 1.88 V, while connecting them in parallel increased the output current from 156 to 412 μA (Fig. 6a). The flexibility and elastic properties of the resulting PSC textile (Fig. 6b) facilitated its application in flexible electronic devices.

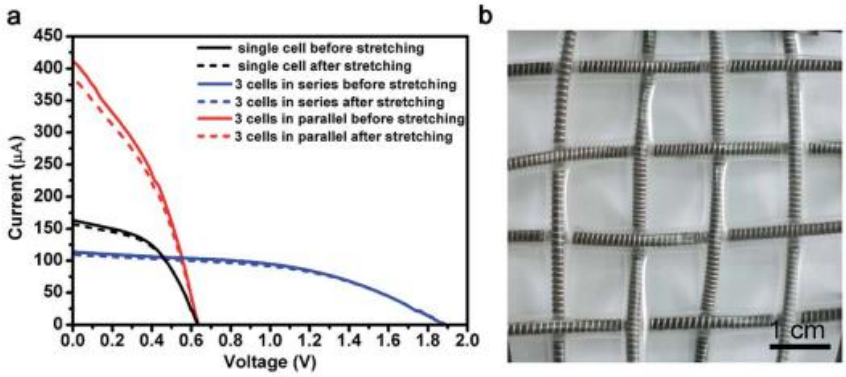

Figure 5.1 (a) J–V curves of the resulting powering textile where three PSC fibers were connected in series or parallel before and after stretching. (b) Photograph of an elastic powering PSC textile.[2]

5.3 Assembling of perovskite solar fabrics

Weaving is a simple method for creating fabric by interlacing warp and weft yarns in a specific pattern. Woven fabrics have properties such as tensile strength, flexibility, permeability, and drape-ability, which are important for achieving protection, style, and comfort when used in clothing. To assemble the solar fabric, we start by sealing the perovskite solar cell (doped with vanillin for an efficiency of approximately 13.18%) in a nylon 66 tubing. The nylon tubing has an estimated transmittance of 85% in the wavelength range of 450 - 850nm. Then, we manually interlace the sealed fiber-shaped solar cells with cotton yarns. The solar cells are positioned in a way that the photoactive side faces the technical side of the solar fabric.

The combination of acrylics with interlacing is used to give the solar fabric a cloth-like texture, absorbency, breathability, and other textile properties. The cooling properties and lightweight nature of acrylics make this fabric ideal for all-day wear.

For our proof of concept, we used 4 solar yarns as the weft and 4 cotton yarns as the warp to create complete weave repeats for 3 different weave patterns: plain weave, twill weave, and satin weave. We chose these weaves because they provide different degrees of light exposure to the solar yarn due to the varying floats created by the weft solar yarns.

The average size of the weave repeats we assembled and tested was approximately 50x45 mm^2. For each weave pattern, we conducted photovoltaic measurements on both parallel and series connections of the solar cells in the solar fabric. We created six mini-modules, with parallel and series connections, for each weave type (see figure 5.2). Each mini-module consisted of 4 solar cells connected together. The photoactive area of the fabric had a footprint of approximately 50 mm × 45 mm.

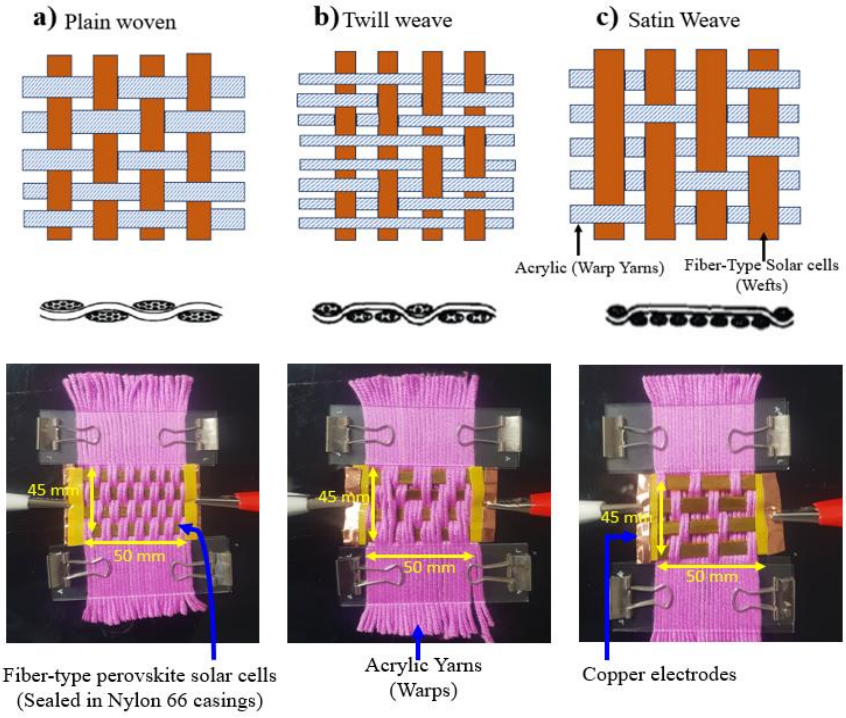

Figure 5.2. Schematic illustration of the solar fabric surface, fabric cross-section and fabric images. a) plain weave. b) Twill weave. c) Satin weave.

5.4 Characterization of the plain-woven solar fabrics

The plain-woven fabric contained solar cells that were connected in both parallel and series arrangements. The fabrics were then characterized and the results are presented in Table 5.1 and Figure 5.3.

To seamlessly integrate the perovskite solar cells made of fiber-type material into the plain-woven fabrics, a simple hand weaving technique was used. By connecting the fiber-type solar cells in either series or parallel, the output voltage and current could be adjusted accordingly. For example, when four solar cells were connected in series, the output voltage increased from 1.01 to 4.04 V. On the other hand, connecting them in parallel enhanced the current density from 3.877 to 3.877 mA/cm^2. Electrical measurements were taken using a high precision solar simulator from the Enli Technology Company. Unless stated otherwise, the measurements were

performed under one sun intensity (1000 W/m2) with an AM1.5 G spectrum. All fixed angle measurements were conducted at a temperature maintained at 25 ± 1 °C.

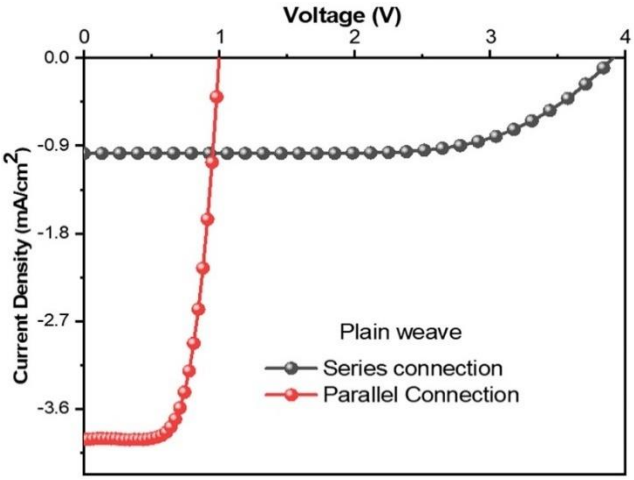

Figure 5.3. I-V curve for the plain-woven fabrics with solar cells connected in series and parallel connections.

Table 5.1. Photovoltaic performance of the plain-woven solar fabric.

Assembly Type	**Open Circuit Voltage (Voc) V**	**Short Circuit Current (Jsc) mA/cm^2**	**Power density (mW/cm^2)**
Single Cell	1.01	22.08	
Series connection (4 Solar Cells)	3.84	0.969	3.72
Parallel connection (4 Solar Cells)	0.98	3.877	3.79

5.5 Characterization of twill and satin-woven solar fabrics

The characteristics of satin and twill-woven solar fabric weaves, created by interlacing solar yarns and cotton yarns, were analyzed. The tests were conducted at room temperature and

humidity levels between 55-60%, with an irradiance of 1 sun (1000 W/m^2) and a gravitational force of 1.5G. The tested area of the weave measured (50 x 45) mm^2.

The results of the photovoltaic measurements showed that the current and voltage output generally increased as the weave pattern changed from plain to twill to satin. For example, when four cells in a woven fabric were connected in series, the voltage increased from 3.84V for plain fabric to 4.01V for twill fabric and 4.03V for satin fabric. These findings are summarized in Table 5.2 and Figure 5.4. It should be noted that the variations in the expected results are due to mismatches in current and voltage caused by differences between cells and variations in the angular position of the embedded solar cells relative to the fabric's surface.

On the other hand, when the cells were connected in parallel, there was a gradual increase in the open circuit current density. The plain fabric sample had an open circuit current density of 3.877 mA/cm^2, while the twill fabric sample had a density of 3.902 mA/cm^2, and the satin fabric sample had a density of 3.916 mA/cm^2.

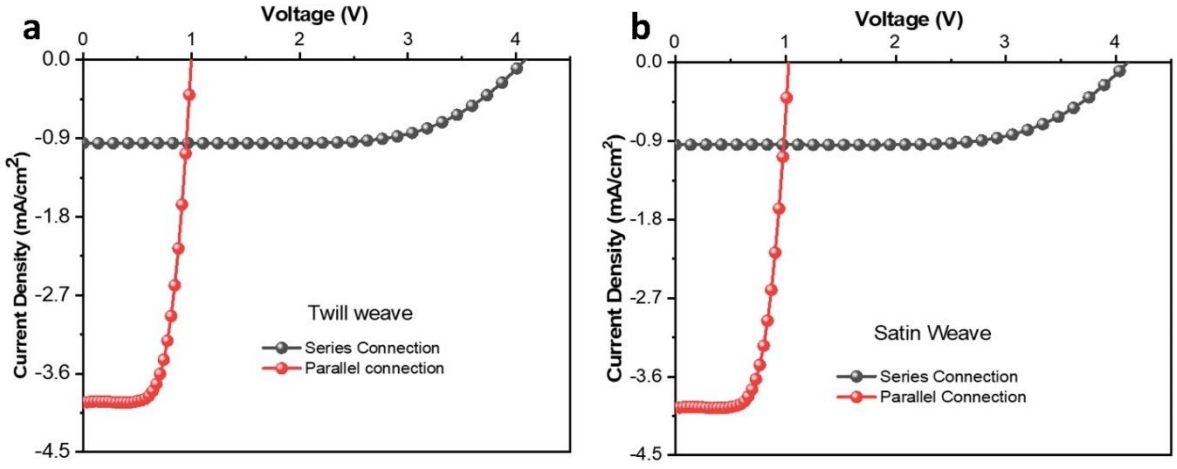

Figure 5.4. I-V curve for the satin and twill-woven fabrics with solar cells connected in series and parallel connections.

Table 5.2. Photovoltaic performance of the twill and satin-woven solar fabric.

Assembly Type	Open Circuit Voltage (Voc) V	Short Circuit Current (Jsc) mA/cm^2	Power density (mW/cm^2)
Single solar cell	1.01	22.08	

Twill woven solar fabric			
Series connection (4 Solar Cells)	4.01	0.940	3.76
Parallel connection (4 Solar Cells)	0.98	3.902	3.82
Satin woven solar fabric			
Series connection (4 Solar Cells)	4.03	0.944	3.80
Parallel connection (4 Solar Cells)	1.01	3.916	3.95

Figure 5.5a, shows that when the satin solar fabric (area 22.5 cm^2 and parallel inherent solar cell connection) was exposed to increasing light intensities, ranging from 20% to 100% sun illumination, both voltage and current showed a gradual increase. At 20% sun, the fabric exhibited a voltage of 0.913V and a current density of 3.715 mA/cm^2, which then increased to 1.01V and 3.916 mA/cm^2 at 100% sun.

This increase in voltage and current is a result of the direct proportionality between light intensity, incident number of photons on the solar fabric, and the generation of charge carriers. As the light intensity increases, more photons interact with the fabric, leading to the generation of additional charge carriers and subsequently boosting the energy output of the solar fabric.

Overall, the results demonstrate the fabric's ability to efficiently harness solar energy and convert it into usable electrical power, making it a promising technology for sustainable energy applications.

As shown in Figure 5.5b, in the study conducted on satin solar fabric, it was observed that there is a correlation between the angle of light incidence and the normalized power density (NPD). When the angle of incidence of light is increased, there is a slight increase in the NPD. Specifically, the NPD of the fabric increases from 98.9% at 10 degrees to 99.9% at 70 degrees.

Interestingly, between 80 and 110 degrees, the NPD remains almost constant at its maximum value of around 100. This indicates that within this range of angles, the fabric is able to maintain a high level of power density efficiency.

However, beyond 110 degrees, there is a slight reduction in NPD, with the value dropping to 98.7% at 180 degrees. This reduction in NPD at higher incident angles can be attributed to the

acrylic yarns present in the fabric. At low and high incident angles, these acrylic yarns may obstruct light from reaching certain parts of the solar yarns, leading to a decrease in overall power density. Overall, this study highlights the importance of considering the angle of light incidence when assessing the performance of satin solar fabric, as it can have a significant impact on the normalized power density and efficiency of the fabric.

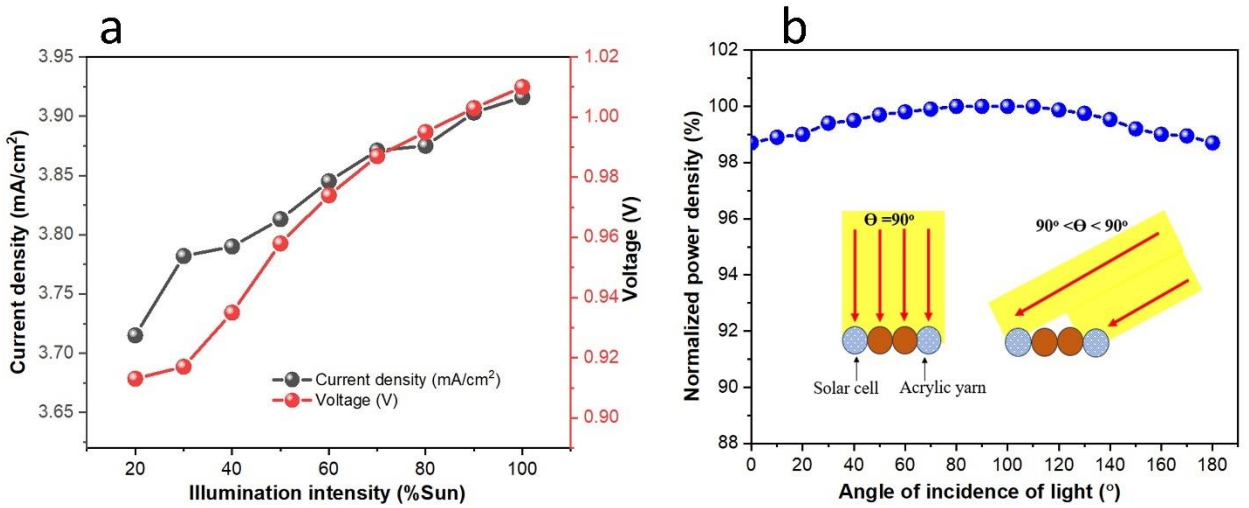

Figure 5.5. a) Variation of light intensity with current and voltage output of satin fabric sample. b) Variation of illumination angle with normalized power density of a satin solar fabric.

5.7 Significant findings and milestones in chapter five

In work package three, we successfully assembled large perovskite solar fabrics (50x45) mm^2 in three different weaves, and we studied and compared the power output of the three weaves.
The following are the key findings and milestones;

1. This study yielded large area (~22.5cm^2), non-toxic and textile-like perovskite solar fabrics, formed by weaving fiber-type perovskite solar cells with acrylic yarns
2. Our study revealed that the maximum power density (3.95 mW/cm^2) from woven solar fabrics could be achieved with a satin weave, using a parallel connection of the solar cells within the fabric.
3. This study also showed that, regardless of weave, connecting solar cells in parallel results in greater power density than connecting them in series.

4. Our research further demonstrated that the power output from a solar fabric made from a certain weave increases with the amount of exposed floating threads (fiber-type solar cells) on the fabric surface.

5.8 Conclusion

This chapter explores the process of creating solar fabrics by interweaving fiber-type perovskite solar cells with acrylic yarns into plain, twill, and satin fabrics. The woven solar cells were then connected in both series and parallel configurations to analyze how these connections affect the energy output of the solar fabrics. The results generally indicate that the energy output of the solar fabrics increases as the weave pattern transitions from plain to twill to satin. This is because, as the weave pattern changes and parallel connections are made, the voltage output of the fabric gradually increases. In the case of series connections, the current output from the fabrics also follows the same order of weave pattern mentioned above. The reason for the observed increase in energy output from plain to twill, with satin producing the highest energy output, is that satin weaves have the most floating yarns on the fabric, exposing them to more illumination and thus resulting in increased energy output.

5.9 References

1. Stoppa, M. and A. Chiolerio, Wearable electronics and smart textiles: A critical review. sensors, 2014. **14**(7): 11957-11992.

2. Deng, J., L. Qiu, X. Lu, Z. Yang, et al., Elastic perovskite solar cells. J. Mater. Chem. A, 2015. **3**(42): 21070-21076.

3. Fan, X., B. Liu, J. Ding, Y. Deng, et al., Flexible and wearable power sources for next-generation wearable electronics. Batteries Supercaps, 2020. **3**(12): 1262-1274.

4. Hashemi, S.A., S. Ramakrishna, and A.G. Aberle, Recent progress in flexible–wearable solar cells for self-powered electronic devices. Energy & Environmental Science, 2020. **13**(3): 685-743.

5. Lam, J.-Y., J.-Y. Chen, P.-C. Tsai, Y.-T. Hsieh, et al., A stable, efficient textile-based flexible perovskite solar cell with improved washable and deployable capabilities for wearable device applications. RSC Adv, 2017. **7**(86): 54361-54368.

6. Jung, J.W., J.H. Bae, J.H. Ko, and W. Lee, Fully solution-processed indium tin oxide-free textile-based flexible solar cells made of an organic–inorganic perovskite absorber: Toward a wearable power source. Journal of Power Sources, 2018. **402**: 327-332.

Chapter 6: Challenges, Future research and Conclusions

6.1 Summary of the major challenges

This thesis conducted experimental investigations and detailed analysis on perovskite materials, fiber-type perovskite solar cell assembling, and the assembling and characterization solar devices and solar fabrics. In brief, our study encountered the following challenges;

1. Challenges in accurately estimating the photoactive area of fiber-shaped solar cells. Cylindrical fiber-shaped solar cells twisted with top electrodes make it very complex to accurately determine the photoactive area. Since area factors in determining the power conversion efficiency of a solar cell, errors involved in estimating the photoactive area will be reflected in the estimated PCE.
2. Toxicity of solvents and other materials that make make-up solar cells. One of the primary challenges in perovskite material synthesis is the potential toxicity of certain components used in the process. Perovskite materials often contain lead, which raises concerns about environmental impact and human health hazards. Even though this study focused on replacing Pb with Sn to overcome the toxicity challenge, research has demonstrated that excessive intoxication of Sn beyond the lethal dose case can bring about toxicity. Additionally, some solvents used in the synthesis process such as DMF and DMSO can also be toxic, posing challenges in handling and disposal.
3. Another challenge encountered is that generally, the PCE in fiber-type perovskite solar cells is still low compared with planar devices and Pb-based fiber-type solar cells. For example, the highest PCE achieved in our investigation with Sn-based fiber-shaped perovskite solar cells is 13.18%, which is lower than 15.7% reported with Pb-based fiber-type solar cell and 26% reported with planar Pb-based perovskite solar cell. Both Sn-based fiber-type solar cells and fabrics face challenges in achieving high power conversion efficiency comparable to traditional planar Pb-based counterparts (25.7%). The constraints of flexible and lightweight materials used in these devices can limit the efficiency of light absorption and energy conversion, making it a key area for improvement.

4. In our study, we also encountered limited shelf-time for the fiber-type solar cells. Our investigation indicated that the best performing device could last for an average lifetime of 3 month. This hinders the commercialization, and increases the recycling frequency of the fiber-type solar cells. This observation is due to the fact that perovskite materials are known to degrade over time when exposed to moisture, oxygen, and light. This degradation can occur during storage, transportation, or even in the final device assembly process, leading to a limited shelf life and affecting the overall performance and reliability of solar yarn and fabric devices. Additionally, Sn-based perovskite material oxidation is one of the major setbacks encountered in this work: Exposure to oxygen and other reactive species can lead to oxidation of Sn^{2+} to Sn^{4+} leading to loss of photovoltaic performance of the material and perovskite-based devices, impacting their stability and long-term performance. Proper encapsulation and protection measures such as the use of antioxidants are essential to prevent oxidation and ensure the durability of solar yarn and fabric devices. Addressing these challenges through advanced materials research, innovative manufacturing techniques, and rigorous quality control measures will be crucial in realizing the full potential of perovskite-based solar yarn and fabric technologies.
5. Finally, frictional damage during weaving is also a major challenge. During the weaving process of solar fabric, frictional forces can cause damages to the delicate perovskite materials, affecting their optical and electrical properties. Careful handling and specialized weaving techniques are required to minimize such damages and ensure the integrity of the solar fabric structure.

6.2 Future research

In the realm of fiber-shaped perovskite solar cell technology, the pursuit of more efficient and durable perovskite devices has been an ongoing endeavor. To further advance the field, several key future research directions have been identified. Therefore, to realize the long-term objectives of this area of research, we herein propose the following research directions in order to overcome the challenges pointed out in the previous section of this chapter.

1) Developing fully inorganic 2D3D cesium-based perovskite materials to mitigate for long-term outdoor device service. The investigation in our work revealed that the best bets devices could serve for approximately 2000 hours due to perovskite material degradation. Exploring the potential of fully inorganic perovskite materials based on cesium presents a promising avenue for mitigating material degradation issues commonly associated with traditional organic-inorganic hybrid perovskites. By focusing on cesium-based compositions, the research aims to enhance the stability and longevity of perovskite solar cells.

2) The use of more robust antioxidants should be considered to further mitigate Tin-based perovskite Material Degradation. Investigating the application of robust antioxidants to combat material degradation in tin-based perovskite materials is another critical direction for future research. By incorporating antioxidants into the material composition, researchers seek to enhance the long-term stability and performance of tin-based solar cells.

3) Perovskite Layer Deposition and Optimization challenges on curved surfaces: Further refining the deposition techniques for perovskite layers on non-flat surfaces (fiber-shaped structures) is essential for achieving uniformity, consistency, and high efficiency in solar cell fabrication. By optimizing the deposition process, researchers aim to improve the structural integrity and electrical properties of perovskite layers, ultimately enhancing overall device performance.

4) Perovskite solar cell encapsulation challenges: Optimizing the encapsulation methods for solar cells is crucial for protecting the delicate components from environmental factors such as moisture, oxygen, and light exposure. By optimizing the encapsulation materials and techniques, researchers seek to increase the durability and reliability of solar cell devices under varying operating conditions.

5) Large area solar fabric assembling and comprehensive characterization challenges: weaving large surface-area solar fabrics is associated with challenges such as friction between the warp and weft yarns that causes severe damages and loss of fabric efficiency. Additionally, conducting thorough characterization of solar fabrics on a large scale is vital for understanding their performance across different applications and environments. By employing comprehensive

characterization techniques, researchers aim to gain valuable insights into the structural, optical, and electrical properties of solar fabrics, leading to improved design and efficiency.

6) Enhance solar cell lifetime to greater than 20 years: Extending the operational lifetime of solar cells beyond one year is a fundamental goal in advancing the sustainability and economic viability of solar energy technologies. By implementing robust materials, optimized fabrication processes, and effective encapsulation strategies, researchers aim to achieve long-term stability and reliability in solar cell devices.

In summary, the challenges and proposed future research directions outlined above represent crucial areas of investigation that hold the potential to drive significant advancements in the development of high-performance, durable, and efficient solar cell technologies. By addressing material degradation challenges, optimizing fabrication processes, and enhancing device characterization, researchers can pave the way for the widespread adoption of solar energy as a clean and renewable power source.

6.3 Conclusions

Fiber-shaped perovskite solar cells for wearable, renewable and sustainable energy sources, have attracted great interest in the field of solar energy harvesting. This thesis has conducted experimental investigations on this technology, and the detailed procedures and results have been addressed in chapters 3-5.

The following is a summary of noteworthy findings:

1) In the study of synthesizing Sn-based 2D3D hybrid perovskite materials, we introduced a method for synthesizing and controlling the reaction between 2D and 3D molecules for high-quality 2D3D hybrid perovskite materials via chlorine doping. Our approach is based on the ability of chlorine to displace iodine from its ionic compounds in solution, creating a reaction that speeds up the formation of high-quality 2D3D perovskite materials. We increased the doping proportion of chlorine in the iodine-based mixture of 2D and 3D perovskites in solution and reduced the effective reaction time to 20 minutes at 100ºC. The approach also enables the use of

DMF as a single solvent to achieve perpendicular orientation of perovskite slabs at 50% chlorine doping and beyond. Additionally, we proposed a chemical reaction mechanism through which chloride ions catalyze the formation of 2D3D hybrid perovskites from iodine-based 2D and 3D perovskite molecules in solution. The synthesized 2D3D perovskite material was integrated into a fiber-shaped perovskite solar cell, giving the highest recorded PCE of 11.96% in Sn-based fiber-shaped perovskite solar cells. The solar yarn was vacuum sealed in a nylon casing and maintained more than 95.5% of its original efficiency after a service lifetime of 3 months in ambient conditions. This research presents the first endeavor to synthesize lead-free 2D3D hybrid perovskite material at low synthesis temperatures and reduced reaction time, under the influence of chloride ion reaction catalyzation. The approach yielded high-performance perovskite materials for high-performance fiber-shaped perovskite solar cells.

2) In the second study, we introduced vanillin, a natural antioxidant that undergoes a double-stage redox reaction. This reaction helps to prevent the oxidation of Sn^{2+} or convert Sn^{4+} back to Sn^{2+}, thereby enhancing the efficiency of Sn-based perovskite solar cells and extending their stability in open-air conditions. By incorporating 7.5% vanillin doping in perovskite, we achieved an impressive efficiency of 13.18% using a flexible one-dimensional solar cell architecture. This represents the highest efficiency currently observed in Sn-based fiber-type perovskite solar cells. Additionally, subjecting the solar cell to 160W microwave irradiation for 3 minutes resulted in a recovery of solar cell efficiency from 88% to 96.5% (normalized efficiency) after 812 hours, and from 35.7% to 65.4% after approximately 2200 hours of aging. These findings highlight the potential of natural antioxidation and short microwave irradiation as effective strategies to enhance the efficiency and prolong the lifespan of tin perovskite solar cells.

3) In our third investigation, we went ahead and created woven configurations of the fiber-type perovskite solar cells demonstrated in the second study, by weaving the solar cells with acrylic yarns to produce weave repeats for characterization purposes to prove the concept. Three weave designs i.e., plain, twill and satin weaves were investigated. The results indicate that by connecting the 4 solar cells used in the weave repeats in a parallel connection increases the current from 3.79, to 3.82 to 3.95 mW/cm^2 for plain, twill and satin woven solar fabric, with an estimated area of 22.5 cm^2. Similarly, by connecting the solar cells in series, the voltage

increased from 3.84 to 4.01 to 4.03 V, for plain, twill and satin respectively. These findings reveal the effect of weave designs and solar cell circuit connection pattern on the output current and voltage of the woven solar fabric.

Based on the results obtained and their significant impact, it is evident that this study has successfully achieved its objectives. The findings not only contribute to the existing body of knowledge but also have practical implications for future research and applications in the field.

Appendix

Table S1. Reagents mixing proportions in 5 MLs of DMF solvent

Ratio of SnI_2: $SnCl_2$	1:0	3:1	2:1	1:1	1:3
Halogen % of Chlorine	0%	25%	33%	50%	75%
CH_3NH_3I	0.100g	0.100g	0.100g	0.100g	0.100g
$HOOC(CH_2)_4NH_3I$ (3% of the total mixture)	0.006g	0.007g	0.008g	0.009g	0.015g
SnI_2	0.100g	0.100g	0.100g	0.100g	0.100g
$SnCl_2$	0.00g	0.033g	0.050g	0.100g	0.300g

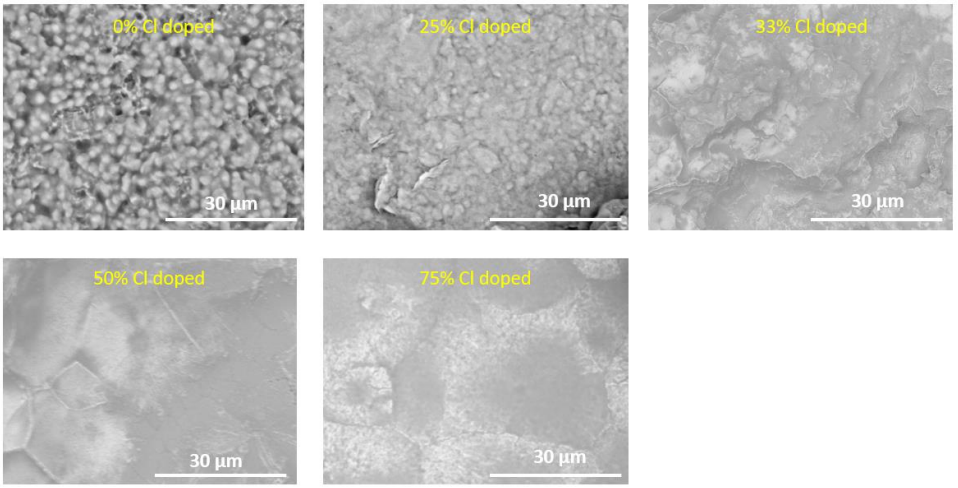

Figure S1. Scanning Electron Microscope (SEM) images of 2D3D perovskites with different chlorine doping proportions deposited on glass substrates.

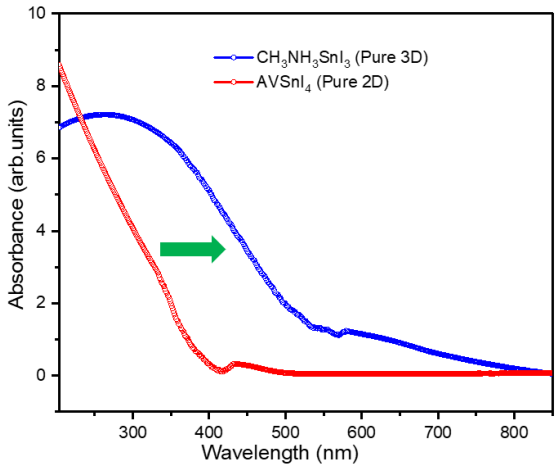

Figure S2. UV absorption spectra of 2D ($HOOC(CH_2)_4NH_3)_2SnI_4$) and pure 3D ($CH_3NH_3SnI_3$) perovskites.

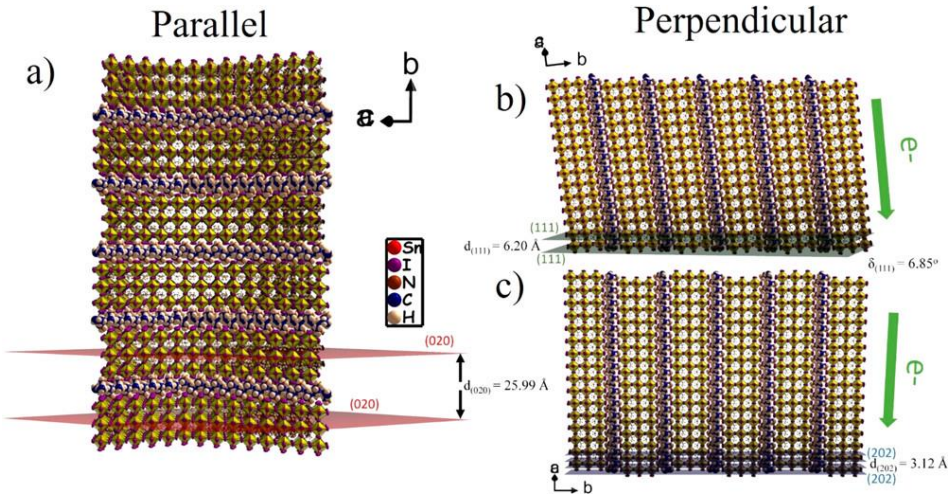

Figure S3. Different thin-film growth orientations of perovskite materials: (a) (0*k*0) parallel oriented, (b) almost perpendicular oriented, and (c) perfectly perpendicular oriented. Reprinted with permission reference (43), Copyright © 2017, American Chemical Society copyright.

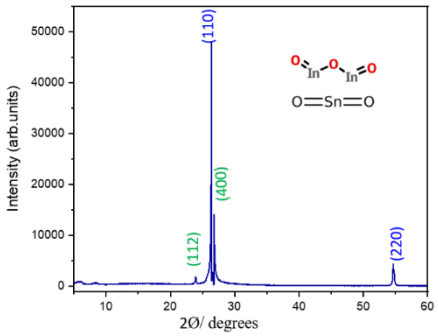

Figure S4. XRD spectra of ITO paste. The blue labeled peaks are a characteristic of Tin oxide nanoparticles. The green-labeled peaks are brought about by Indium oxide nanoparticles.

Table S2. Variation of resistance with increasing electrospinning during for PEDOT: PSS Nanofibers in comparison with dip coated and spin coated samples.

Sample	Electrospinning duration (minutes)	Resistance (kOhm)
S_7	7	12
S_{10}	10	9.5
S_{15}	15	7.56
S_{20}	20	7.23
S_{35}	35	8.38
S_{sc}	Spin coated sample	190.5
S_{dc}	Dip coated sample	160.3

PEDOT: PSS nanofiber Mats electrospun for few minutes (S_7&S_{10}) have the best transmittance but with high resistance probably due to low surface coverage. Nanofiber Mat resistance reduces with increasing electrospinning time to a maximum of 20 min beyond which it increases again. when the nanofiber Mat becomes too thick, resistance in the sample increases because resistance is thickness dependent. Assessment of the %T and Resistance results indicates that the optimum sample is obtained with 15 minutes electrospinning time.

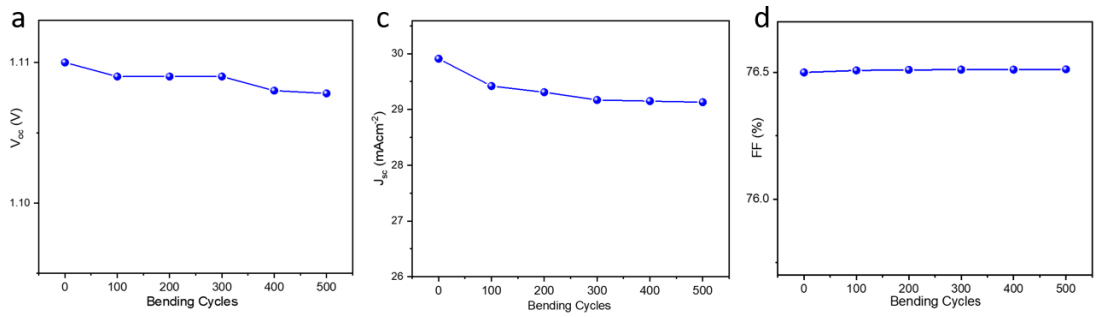

Figure S5. Dependence of photovoltaic parameters on twisting cycle number.

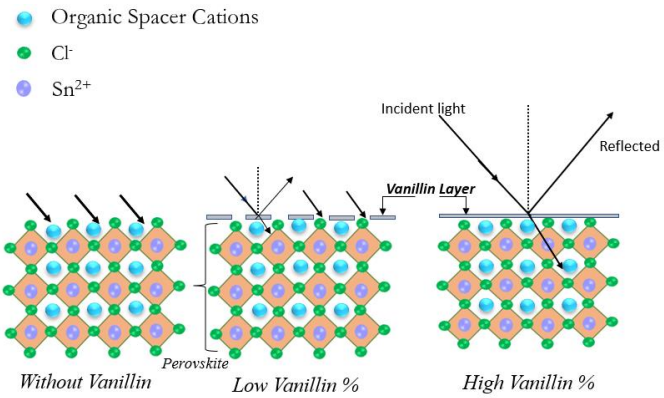

Figure S6. Schematic illustration of the formation of vanillin thin films on the surface of perovskite, and the interaction of the films with light, with increasing vanillin doping in the material.

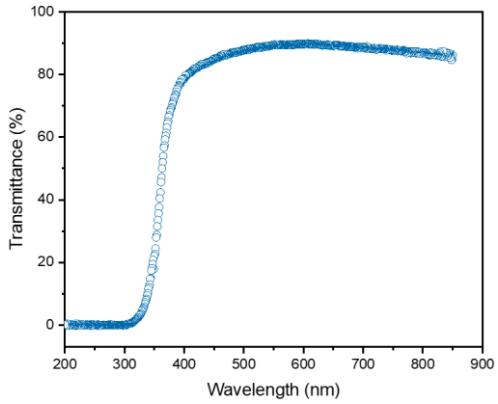

Figure S7. Transmittance spectrum of a pure vanillin film on a glass slide in the 200-850 nm wavelength range.

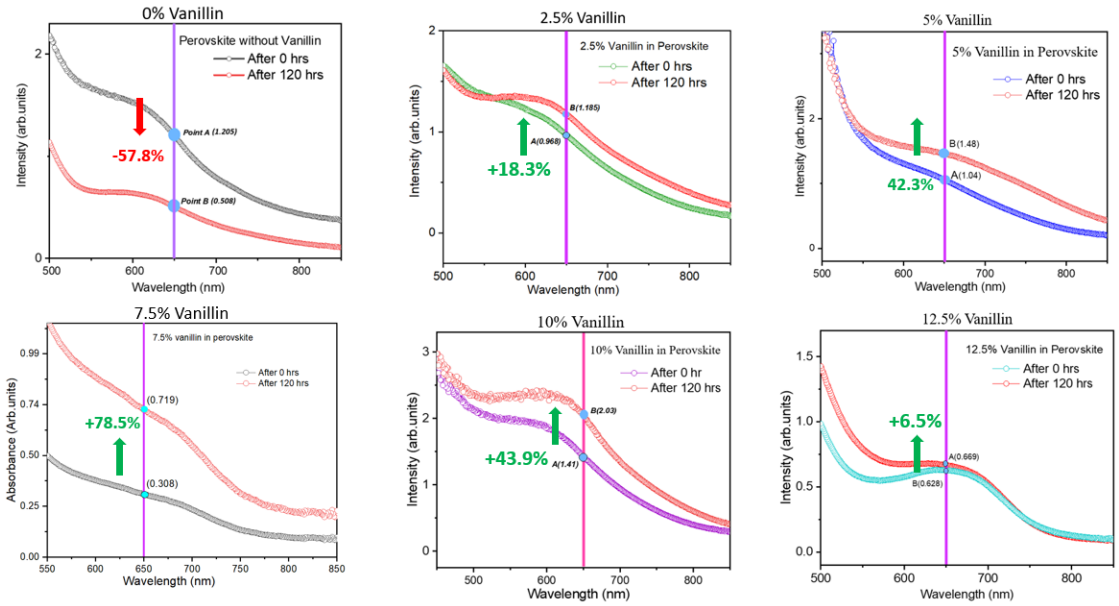

Figure S8: Variation of UV-vis absorbance at 650 nm after 120 hours of exposure, for perovskite films doped with different vanillin quantities.

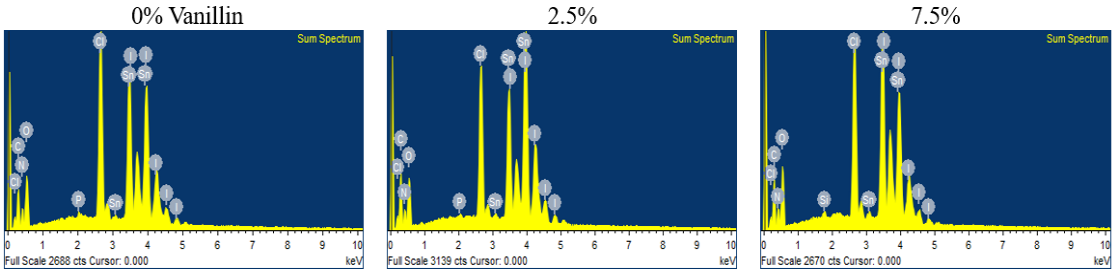

Element	Weight%	Atomic%
C K	13.98	35.45
N K	11.26	16.43
O K	10.37	20.19
Si K	0.32	0.35
Cl K	9.13	7.85
Sn L	32.08	14.24
I L	22.86	5.49

Element	Weight%	Atomic%
C K	12.98	34.31
N K	6.57	14.90
O K	13.48	26.74
P K	0.28	0.29
Cl K	10.22	9.15
Sn L	28.26	7.56
I L	28.20	7.05

Element	Weight%	Atomic%
C K	15.27	38.75
N K	5.53	8.96
O K	10.50	28.54
P K	0.24	0.25
Cl K	8.09	7.49
Sn L	22.34	6.18
I L	38.04	9.84

Figure S9: EDS surface atomic percentage analysis with increasing vanillin doping in perovskite.

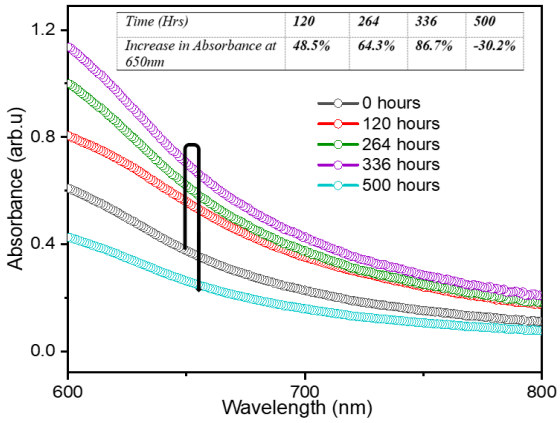

Figure S10: Variation of UV-vis absorption with time (>500 hours of exposure) for 7.5% vanillic acid-doped perovskite.

Table S3: Variation of charge carrier lifetime with increasing vanillin doping in the perovskite material.

Vanillin doping %	0%	2.5%	7.5%	12.5%
Estimated charge carrier lifetime (ns)	19 ns	28 ns	46 ns	25 ns

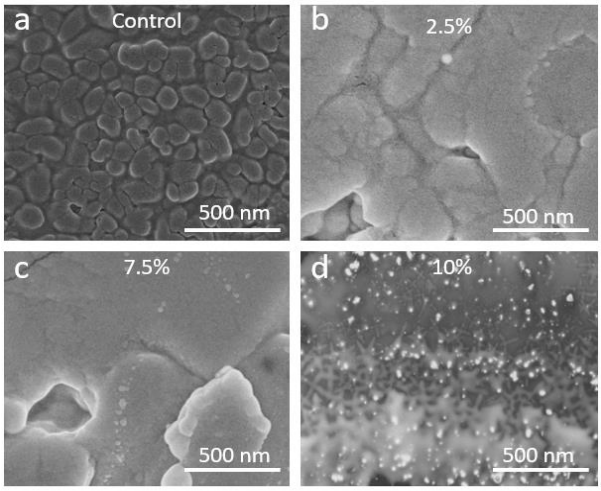

Figure S11: High magnification surface SEM images of vanillin-doped perovskite, showing variations in crystal size.

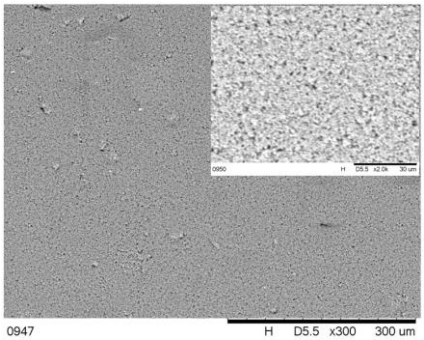

Figure S12: SEM image of the TiO_2 mesoporous layer

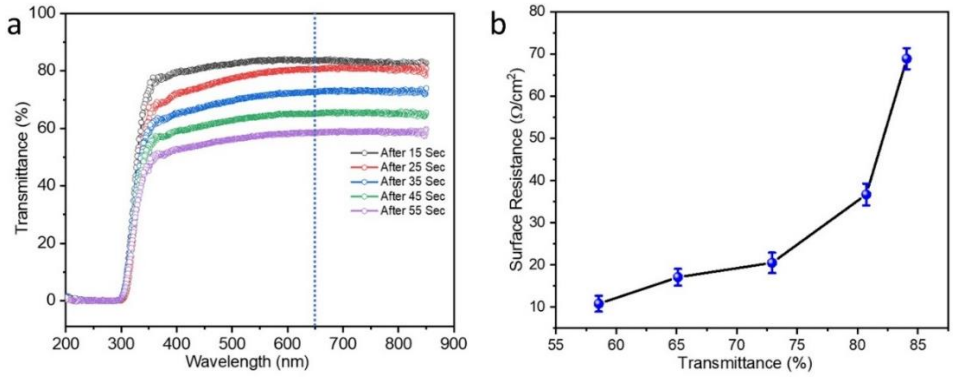

Figure S13. a) Variation of transmittance with platinum layer spattering time at 650 nm wavelength. b) The graph shows the relationship between the thin platinum electrode's transmittance and surface resistance at 650 nm.

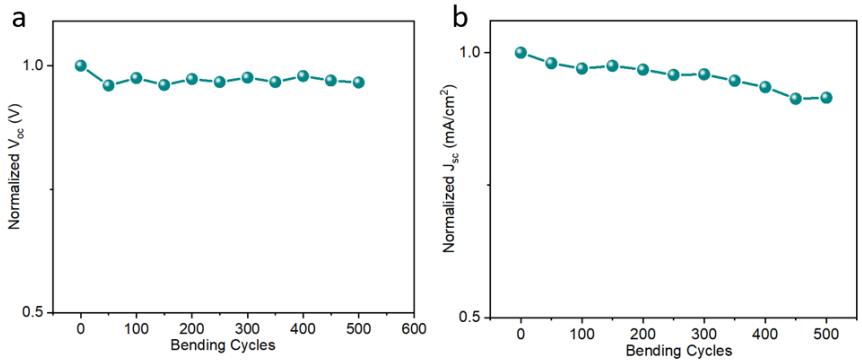

Figure S14(a-b): Variations of open circuit voltage and short-circuit current density during 500 consecutive bending cycles.

Table S4: The fitted recombination resistance (R_{rec}) and series resistance (R_s) of the EIS measurement.

	Recombination resistance (Ω)	Series resistance (Ω)
Control	3027.12	8.73
With vanillin	5254.25	8.51

Table S5: Time dependence of normalized efficiency recovery under 160 W microwave irradiation.

Microwave irradiation time/min	Efficiency at 812 hrs (without microwave treatment)	1	2	3	4	5	6
Normalized Efficiency Recovered (%)	88	89.4	93.5	96.4	92.3	88.4	Cell fails

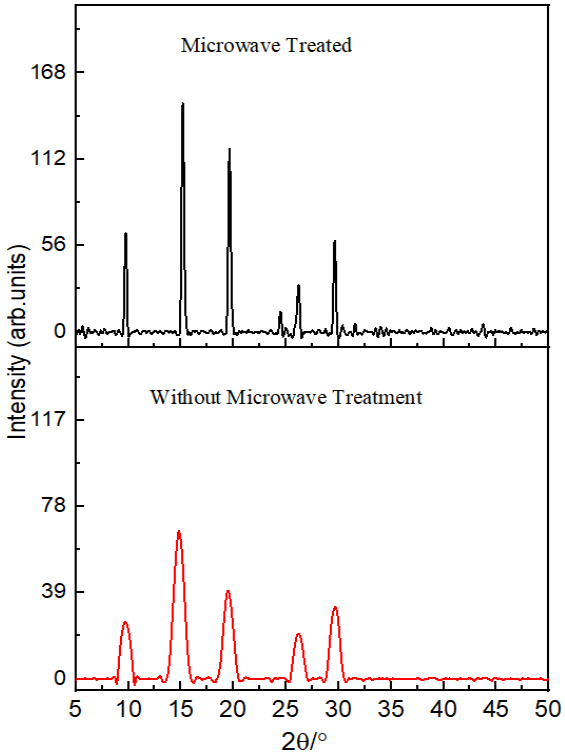

Figure S15: XRD spectra with and without 160W microwave treatment for 3 minutes, taken after 812 hours of sample aging.

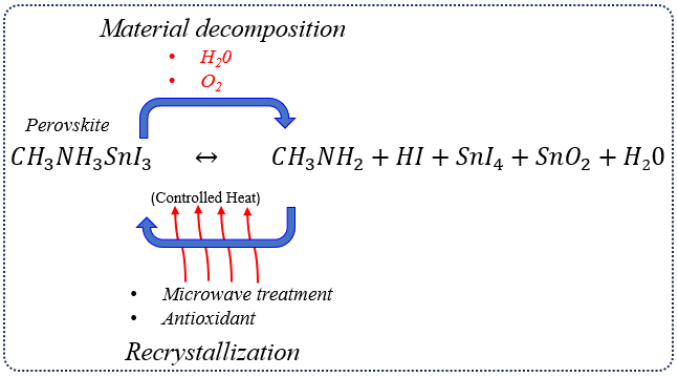

Figure S16: Proposed perovskite material decomposition and recrystallization cycle for the vanillin-doped and microwave treated solar cells.